POLITECNICO DI MILANO
DEPARTMENT OF PHYSICS
DOCTORAL PROGRAMME IN PHYSICS

ELECTRICAL ACCESS TO ANTIFERROMAGNETISM IN METALLIC AND INSULATING THIN FILMS

Doctoral Dissertation of:
Marco Asa

Supervisor:
Prof. Matteo Cantoni

Tutor:
Prof. Riccardo Bertacco

The Chair of the Doctoral Program:
Prof. Paola Taroni

2019 – XXXI

Summary

The discovery of the effect presently known as anomalous Hall dates back to 1881 when Edwin H. Hall observed that a current flowing in a perpendicularly magnetized iron slab produces a transverse voltage one order of magnitude larger than in other non-magnetic metals. A proper understanding of this peculiar property of ferromagnets took more than 70 years, and, today, it is well established that the fundamental origin of the anomalous Hall effect comes from the simultaneous presence of spin-orbit coupling in the solid and broken time inversion symmetry arising from the magnetization. Interestingly, recent observations of large anomalous Hall effect have been reported in antiferromagnetic systems, although the magnetization in antiferromagnets is zero by definition. In these systems, like Mn_3Ge or Mn_3Sn, the peculiar non-collinear spin structure introduces a topological term in the transverse conductivity, originating the anomalous Hall effect. These findings were not just important as a fundamental achievement in solid state physics but also opened some possible applications in the emerging field of antiferromagnetic spin-electronics (or spintronics), which hopes to realize memory devices faster, more scalable and more robust than their ferromagnetic counterpart. In fact, anomalous Hall effect is one of the possible routes that can be used to read the state of antiferromagnetic memory cells.

Metallic non-collinear antiferromagnets, however, represent a rather specific case, where this anomalous component depends on the precise crystal structure and composition. The work presented here proposes instead a more general case, consisting of interfaces between antiferromagnetic and non-magnetic thin films which display a sizable anomalous Hall effect. We demonstrate in fact the possibility to detect electrically the proximity induced magnetization in the non-magnetic layer in contact with the antiferromagnet. The advantage of this method is that it can be exploited independently on the type of ordering (i.e. it works also on collinear antiferromagnets) and is even applicable to insulating antiferromagnets. Several examples are provided demonstrating the generality of this approach, identifying anomalous Hall measurements as a quick and cost-effective way of characterization both in fundamental studies as well as in actual devices.

A first instructive example is provided by the platinum/chromium system. The use

of simple elemental compounds as in this case allows for precise *ab initio* calculations of the electronic and magnetic properties of the materials. By doing so, we found indications that antiferromagnetic chromium induces a net magnetization in neighboring platinum layer. With the idea of electrically detecting this induced magnetization, we grew those compounds as thin films by molecular beam epitaxy (MBE). Simple cross structures were patterned by conventional lithographic techniques and ion milling, allowing for a comprehensive electrical characterization of the bilayer as a function of temperature and magnetic field. After having assessed a solid antiferromagnetic behavior up to 290 K, we demonstrated that an anomalous Hall effect can be observed in absence of any external magnetic field. To this scope, we cooled down through the magnetic phase transition in presence of an applied magnetic field to set a preferred magnetic orientation of the Pt/Cr interface. Depending on the writing field direction, different states of transverse resistance can be reproducibly set and read-out at remanence up to the transition temperature of 290 K. We demonstrate that the origin of this anomalous transport comes only from the interface, as shown by repeated experiments with various Cr and Pt thickness, and it is suppressed when a diamagnetic gold interlayer is placed between Cr and Pt. All these results allow to exclude possible competing mechanisms for explaining the observed transport behavior, and definitely point out a specific role of the proximity induced magnetization in Pt.

Even though Cr is an excellent demonstrator, since the relationship between electrical transport effect and antiferromagnetism is backed by *ab initio* calculations, the Hall signal is very small in this case and requires an high-accuracy measurement setup.

Nevertheless, the same principle of operation can be generally extended to other antiferromagnetic systems which provide a larger signal and are thus more suitable for applications.

For instance, one interesting case covered is the one of Ta/IrMn which presents an Hall signal 4 orders of magnitude larger than Pt/Cr. Multiple states of resistance can be set in Ta/IrMn using different values of the magnetic field applied out of the field plane during the cooling process. Moreover, being the state stored in the antiferromagnet, the read-out can be performed at remanence and it cannot be erased below the transition temperature by external fields (at least up to 9 T).

Besides for potential applications, the electrical detection of antiferromagnetic state can be used also for fundamental studies in material science. An example that will be discussed in this context is the one of tetragonal Cr_2O_3, an uncommon phase of Cr (III) oxide for which no previous reports of antiferromagnetism were given. We demonstrate that thin film of t-Cr_2O_3 can be stabilized by epitaxy on perovskite $BaTiO_3$. We then show how interface effects in Pt/t-Cr_2O_3 can be used to verify a magnetic phase transition at about 40 K which can be identified both by measuring the magnetoresistance and the anomalous Hall effect.

Finally, we will discuss the case of Pt/$TmFeO_3$. Bulk $TmFeO_3$ belongs to the class of rare-earth orthoferrites which, although they present interesting magnetic properties, are seldom studied in thin films. We cover the optimization of the growth by pulsed laser deposition of $TmFeO_3$ on $SrTiO_3$, and demonstrate through anomalous Hall effect in Pt its antiferromagnetic nature up to room temperature.

Supported by all these experimental evidences, we can conclude that proximity effects are a widespread phenomenon at interfaces between certain non-magnetic metals

and antiferromagnets, providing at the same time a tool for the electrical detection of the magnetic state in antiferromagnetic systems. We envisage electrical measurements, and anomalous Hall in particular, as powerful methods for the characterization of magnetic properties in unknown or new materials as well as a potential way to read-out information in antiferromagnetic spintronic devices which, free of any ferromagnetic layer, are fully robust against external fields.

Preface

The present thesis reports part of the work carried out by the author, Marco Asa, from the beginning of his Ph.D. studies on November 1st, 2015. The principal supervisor has been Prof. M. Cantoni from Politecnico di Milano. The experimental activity was carried out in two research centers:

- The nanotechnology research facility Polifab part of Politecnico di Mlano, Milano (Italy) and the associated Nanomagnetism laboratory part of the Department of Physics.

- The department of Physics of the Johannes Gutemberg Universität, Mainz (Germany) for a period of six months (April 2018 - September 2018).

This Ph.D. work has resulted in the following publications:

1. Marco Asa, Lorenzo Baldrati, Christian Rinaldi, Stefano Bertoli, Greta Radaelli, Matteo Cantoni, and Riccardo Bertacco. Electric field control of magnetic properties and electron transport in BaTiO 3 -based multiferroic heterostructures. *Journal of Physics: Condensed Matter*, 27(50):504004, dec 2015

2. Marcus Liebmann, Christian Rinaldi, Domenico Di Sante, Jens Kellner, Christian Pauly, Rui Ning Wang, Jos Emiel Boschker, Alessandro Giussani, Stefano Bertoli, Matteo Cantoni, Lorenzo Baldrati, Marco Asa, Ivana Vobornik, Giancarlo Panaccione, Dmitry Marchenko, Jaime Sánchez-Barriga, Oliver Rader, Raffaella Calarco, Silvia Picozzi, Riccardo Bertacco, and Markus Morgenstern. Giant Rashba-Type Spin Splitting in Ferroelectric GeTe(111). *Advanced Materials*, 28(3):560–565, jan 2016

3. Lorenzo Baldrati, Christian Rinaldi, Alberto Manuzzi, Marco Asa, Lucia Aballe, Michael Foerster, Neven Biškup, Maria Varela, Matteo Cantoni, and Riccardo Bertacco. Electrical Switching of Magnetization in the Artificial Multiferroic CoFeB/BaTiO 3. *Advanced Electronic Materials*, 2(7):1600085, jul 2016

4. C. Rinaldi, J. C. Rojas-Sánchez, R. N. Wang, Y. Fu, S. Oyarzun, L. Vila, S. Bertoli, M. Asa, L. Baldrati, M. Cantoni, J.-M. George, R. Calarco, A. Fert, and R. Bertacco.

Evidence for spin to charge conversion in GeTe(111). *APL Materials*, 4(3):032501, mar 2016

5. C. Rinaldi, S. Bertoli, M. Asa, L. Baldrati, C. Manzoni, M. Marangoni, G. Cerullo, M. Bianchi, R. Sordan, R. Bertacco, and M. Cantoni. Determination of the spin diffusion length in germanium by spin optical orientation and electrical spin injection. *Journal of Physics D: Applied Physics*, 49(42):425104, oct 2016

6. Marco Asa and Riccardo Bertacco. Impact of semiconducting electrodes on the electroresistance of ferroelectric tunnel junctions. *Applied Physics Letters*, 112(8):082903, feb 2018

7. M. Asa, G. Vinai, J. L. Hart, C. Autieri, C. Rinaldi, P. Torelli, G. Panaccione, M. L. Taheri, S. Picozzi, and M. Cantoni. Interdiffusion-driven synthesis of tetragonal chromium (III) oxide on BaTiO3. *Physical Review Materials*, 2(3):033401, mar 2018

8. Christian Rinaldi, Lorenzo Baldrati, Matteo Di Loreto, Marco Asa, Riccardo Bertacco, and Matteo Cantoni. Blocking Temperature Engineering in Exchange-Biased CoFeB/IrMn Bilayer. *IEEE Transactions on Magnetics*, 54(4):1–7, apr 2018

9. Christian Rinaldi, Sara Varotto, Marco Asa, Jagoda Sławińska, Jun Fujii, Giovanni Vinai, Stefano Cecchi, Domenico Di Sante, Raffaella Calarco, Ivana Vobornik, Giancarlo Panaccione, Silvia Picozzi, and Riccardo Bertacco. Ferroelectric Control of the Spin Texture in GeTe. *Nano Letters*, 18(5):2751–2758, may 2018

Contents

Contents

CHAPTER *1*

Introduction

When he gave his Nobel lecture in 2000, Herbert Kroemer coined the famous expression "*The interface is the device*". [10]. Altough his speech was focused on semiconductor heterostructures, nothing prevents to extend this concept to other material systems as well. As a matter of fact, the ability to grow thin films has enabled undisclosed possibilities in the combination of materials with different properties to realize new types of devices. Novel and unexpected phenomena may arise at interfaces and have attracted large interest from the scientific community. Take as an example the discovery of a conductive two-dimensional electron gas (2DEG) at the interface between the wide bandgap insulators $LaAlO_3$ and $SrTiO_3$. [11] The observance of radically new properties in this system, compared to both compounds taken singularly, has challenged solid state physicist for more than a decade and largely contributed to the emergence of functional oxide research. At interfaces, in general, different electronic, chemical and magnetic properties can be observed depending on the specific system opening countless possibilities in the development of functional metamaterials. Moreover, the understanding of the complex phenomena arising at boundaries gets more and more important when considering nanoscale devices, where the interface represents a significant fraction of the physical object and is often the key element for its functionality.

The work presented here explores novel magnetic phenomena at interfaces between antiferromagnets (AFMs) and non-magnetic metals. Magnetic multilayers have been exploited for long time to realize memories and sensors, and magnetic based devices are coming back massively in use with the commercialization Magnetic Random-Access Memories (MRAM). [12–15] MRAMs, in fact, offer a nonvolatile information storage, with lifetime endurance, excellent packing density, satisfactory read and write time, zero standby leakage, and are well integrated in standard CMOS process technology. [16] All these technologies are based, one way or another, on ferromagnetic ma-

terials, typically alloys based on one or more of the four elemental ferromagnets: Fe, Co, Ni and Gd. Ferromagnetic elements in the device allows for information writing with methods going from the simple application of magnetic fields to the exploitation of spin-currents through the principles of spin-transfer torque [17–19] and spin-orbit torque [20], recent achievements of research in spin-electronics or *spintronics*. Nevertheless, the advantage for ferromagnets of being easy to manipulate is also, in some sense, their weakness as it leaves the possibility of involuntary data loss. This is one of the reason why, also within the same field of spintronics, radically new solutions are under investigation. One of these emerging fields is the *antiferromagnet spintronics*, [21–23] where this thesis work also falls.

In this first chapter we discuss the potential advantages which antiferromagnetic elements can offer for information storage and processing, the state of the art and the current material candidates for antiferromagnetic based technology.

1.1 Motivation

Antiferromagnets (AFMs), materials where neighboring spins align in opposite directions, have been discovered thanks to the work that Louis Néel started in 1932 by introducing the concept of "local molecular field" able to account for some experimental results on both ferrimagnets and antiferromagnets, which by the time were just called "anomalous ferromagnets". [24] In 1970, when he was awarded the Nobel prize for his work, Néel stated that AFMs "do not appear to have any practical application". [25] This is no longer true today, since a fundamental building block of the *spin-valve* architecture at the core of MRAM technology exploits an antiferromagnetic layer which, thanks to the interfacial mechanism of exchange bias, [26] pins a neighboring ferromagnet with a reference magnetization direction. In spin-valves, AFMs keep always the same state and play a passive role in the information storage, however the idea of exploiting AFMs as active elements replacing ferromagnets is currently pursued by many research groups. The key advantages that the use of AFMs can bring are:

1. Higher packing density due to the absence of stray fields.

2. Robustness of the information agains external magnetic fields.

3. Shorter state commutation time because of the intrinsically faster magnetization dynamics. [27]

All the three points come as a result of the zero total magnetic moment, hallmark of full compensation of alternating spins. Zero magnetization, as a counterpart, also hinder both writing and reading of information in the antiferromagnetic order. All the mechanisms employed for setting a ferromagnetic memory cannot be applied as they are in the case of AFMs. Also the detection is more problematic, and an efficient way to read the state in an antiferromagnetic memory cell, as effectively as it is done with ferromagnets, is still to be found.

Indeed, in view of application the optimal solution would require a fully-electrical writing and reading of information in AFMs, and some results presented in the next section already go in that direction. In this context, the present work explores the electrical detection of the antiferromagnetic state in thin films, both metallic and insulating,
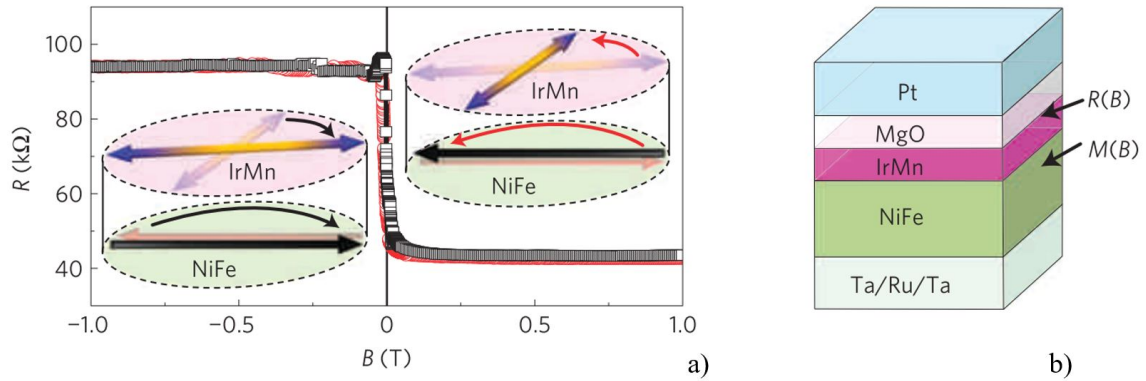
Figure 1.1: *a) Magnetoresistance signal recorded in the range of -1 to +1 T field on a tunneling device fabricated in the NiFe/IrMn(1.5 nm)/MgO/Pt tunnel junction. The insets illustrate the rotation of AFM moments in IrMn through the exchange-spring effect of the adjacent NiFe ferromagnet. The external magnetic field is sensed by the NiFe ferromagnet whereas the tunneling transport is governed by the IrMn antiferromagnet. b) Sketch of the complete heterostructure. Reprinted with permission from [31].*

exploiting the Anomalous Hall Effect (AHE) which can be observed at interfaces between antiferromagnets and some non-magnetic materials. We demonstrate that this phenomenon is rather general extending the class of antiferromagnetic material candidates where the magnetic state can be detected. Moreover, besides the possible applications this approach is cost-effective and readily available in many academic laboratories, enabling a preemptive investigation of AFMs which is complementary to standard characterization with neutron [28] or synchrotron light sources. [29]

1.2 Antiferromagnetic spintronic devices

The first suggestion of a possible scheme to turn AFMs from passive elements in spin-valves to information carriers appeared in 2010 with the theoretical work of Shick *et al.* [30]. The authors proposed bimetallic antiferromagnets IrMn and Mn_2Au as possible candidates for the realization of spin-valve like structures based on the concept of tunneling anisotropic magnetoresistance (TAMR). TAMR junctions consist of an insulating tunnel barrier sandwiched between an AFM electrode and a nonmagnetic metal. Because of the spin-orbit interaction, the tunneling probability is anisotropic and depends on the orientation of AFM magnetization with respect to the crystallographic directions. An experimental demonstration of this effect came one year later using IrMn and Pt as electrodes and MgO as tunnel barrier. [31] In this heterostucture a change in tunneling resistance up to 130% could be observed upon application of an external magnetic field (see Figure 1.1a). The complete structure, also including a ferromagnetic (FM) NiFe element, is shown in Figure 1.1b. The importance of this ferromagnetic layer can be understood looking at the insets of Figure 1.1a: FM and AFM are interfacially coupled and, thanks to the mechanism of exchange spring, turning the FM magnetization drags the AFM as well. This writing method, however, still requires the presence of a FM layer removing any possible advantage that antiferromagnet-only spintronics can bring.

A possible alternative writing scheme in a fully antiferromagnetic TAMR junction
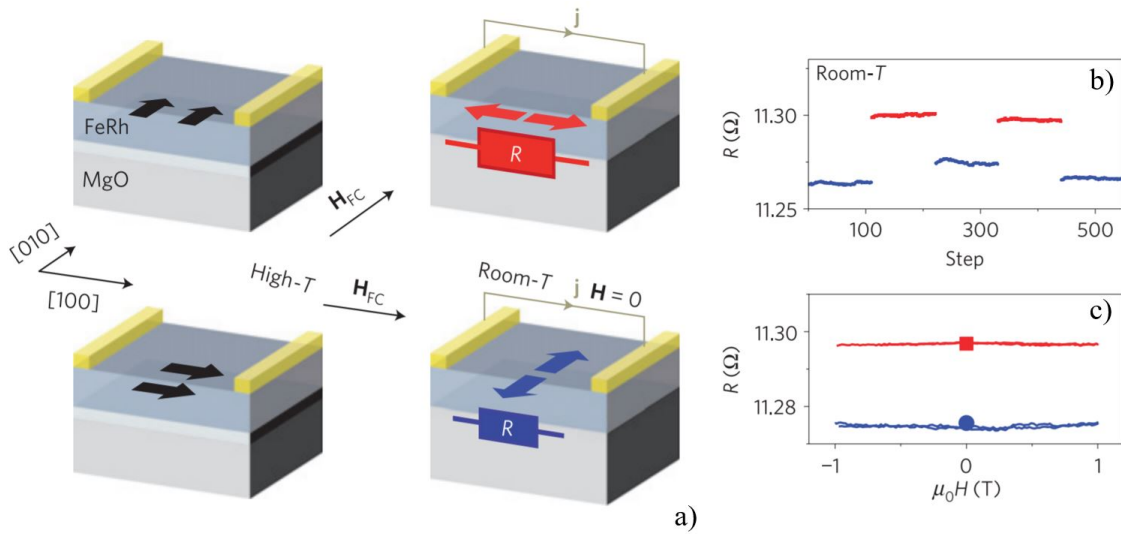
Figure 1.2: *a) Schematic illustration of the FeRh resistor and of the memory writing and reading setup. For writing, the sample is field cooled from a temperature above the AFM-ferromagnetic transition in FeRh. b) Resistance measured at room temperature and zero magnetic field after field-cooling the sample with field parallel (blue) and perpendicular (red) to the current direction. c) Stability of the two memory states at room temperature tested by measuring the resistance while sweeping a magnetic field H between ± 1 T. Reprinted with permission from [33].*

involves the so called field-cooling process and has been demonstrated in Ta/MgO/IrMn heterostructure by Petti *et al.* [32]. In the field-cooling process, a magnetic field is applied while the AFM is heated above its transition temperature to paramagnet. The field is maintained while cooling back the material in the AFM phase so to freeze a well determined direction for the staggered magnetization which can be controlled by the orientation of the external field.

Another early report of AFM memory cell which can be written by field-cooling and read electrically is based on FeRh resistors. [33] FeRh has the peculiarity of being ferromagnetic above 350 K while presenting a gradual transition to an AFM ground state at lower temperatures. This can be exploited as shown in Figure 1.2a, using the field to align the moment in the FM phase in order to determine the spin configuration (parallel or orthogonal to the current) in the AFM phase. The two states can be distinguished from the different longitudinal resistance measured (see Figure 1.2b) because of the mechanism of anisotropic magnetoresistance (AMR). This effect, largely known in ferromagnets but observed also in some antiferromagnetic metals, [34] determines a different resistivity of the magnetic metal depending on the relative orientation between the spins and the current flow and it will be covered with more detail in section 2.4.1.

Figure 1.2c shows one of the advantages of storing information in an AFM. The memory state, represented by the resistance, is unaffected upon the application of ± 1 T when the device is operated below the transition temperature.

Of course the writing via field-cooling is excellent for demonstrators and academic research, but a fully electric read/write process, as available in conventional MRAMs, is highly desirable for applications. Two materials have been proposed in this context: CuMnAs [35] and Mn_2Au. [36] In these materials, the broken spatial-inversion symmetry of the crystalline lattice determines a spin-orbit torque acting independently as
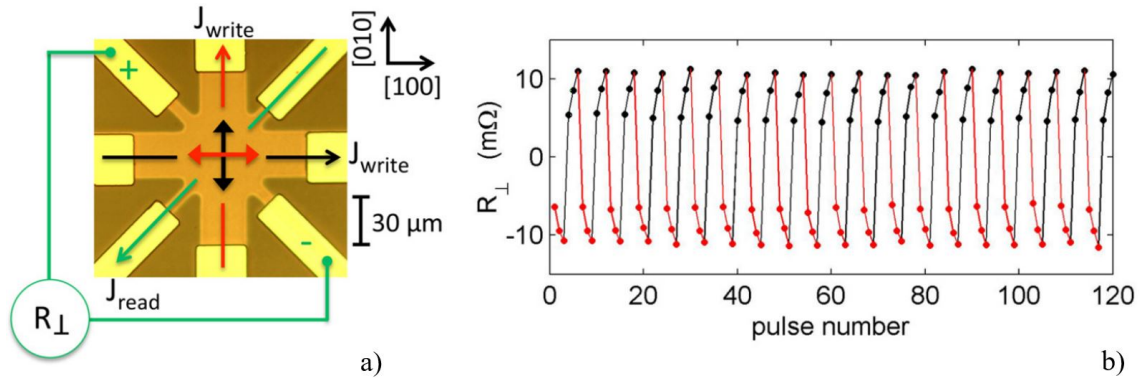
Figure 1.3: *a) Optical microscopy image of the eight-terminal CuMnAs device and schematic of the measurement geometry. b) Change in the transverse resistance after applying three successive 50 ms writing pulses of amplitude J_{write} = 4·10^6 Acm^{-2} alternatively along the [100] crystal direction of CuMnAs (black arrow in panel a and black points in panel b) and along the [010] axis (red arrow in panel a and red points in panel b). The reading current read J is applied along the [110] axis and transverse resistance signals $R_\perp$ are recorded 10 s after each writing pulse. A constant offset is subtracted from $R_\perp$. From [35] Reprinted with permission from AAAS.*

described in [37] on the two spin-sublattices which constitutes collinear AFMs (see Section 2.1. This means that a sufficiently large current can control the staggered magnetization, in particular forcing it to lie perpendicular to the current direction. In CuMnAs first, this has been employed in an eight-contacts geometry as depicted in Figure 1.3a

Write pulses are sent either along the [100] or [010] direction of the crystal (red and black arrows in 1.3a) ideally rotating the magnetization by 90°. The state is then read measuring the transverse voltage by using the four contacts rotated by 45°. As will be detailed in section 3.3.1, this measurement geometry, often called planar Hall sensor, acts as a fully balanced Wheatstone bridge used to maximize the signal coming from the anisotropic resistance change due to AMR (and has nothing to do with the Hall effect despite the name).

The result of multiple writing pulses is reported in Figure 1.3b. Actually, more than two states can be set as the AFM rotation is not coherent but proceeds by domain wall motion. This can be exploited for the realization of multilevel devices. [38] It is also worth nothing that recent reports show that the magnetic state on CuMnAs can also be manipulated by Terahertz pulses, [39] and detected electrically afterwards.

CuMnAs has demonstrated the potentialities of AFM spintronics but suffers the need of a perfectly ordered epitaxial structure, which has proven very difficult to realize, and is not directly compatible with silicon technology. In the last year, however, spin-orbit torque switching of antiferromagnets has been demonstrated also in Pt/NiO. [40–42] In this case, instead of being an intrinsic mechanism related to the crystalline lattice as in CuMnAs or Mn_2As, it involves the interface with an heavy metal with strong spin-orbit coupling like Pt. This opens multiple opportunities for antiferromagnet spintronics, as simpler and cheaper antiferromagnets can became successful candidates fostering the research of new materials and methods.

Before concluding this review, we cover a last type of AFM memory which has been proposed out of Cr_2O_3 in 2017. [43] Cr_2O_3 is a layered insulating antiferromagnet with
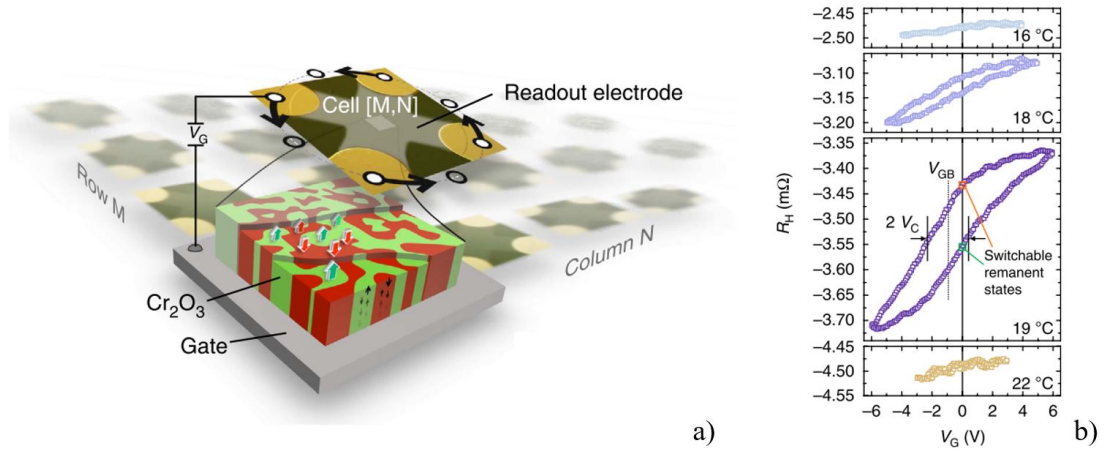
5

Figure 1.4: *a) Pictorial sketch of the Pt/Cr_2O_3 memory cell. The structure consist of a Pt(2.5)/Cr_2O_3(200)/Pt(20)//Al_2O_3 (thicknesses in nm). Exploiting the magnetoelctic coupling of Cr_2O_3, the antiferromagnetic state can be set using an electric field applied across Cr_2O_3 between the two Pt layers. Magnetic proximity effect in Pt allows the electrical detection by measuring the anomalous Hall effect in the Pt layer. b) Anomalous Hall signal and memory window at different temperatures. Reprinted from [43]*

a transition temperature of 307 K. It is also a magnetoelectric system, in which dielectic polarization and magnetization are coupled. [44]

This can be exploited in a geometry such as the one sketched in Figure 1.4a. A Cr_2O_3 thin film is sandwiched between two Pt electrodes in a parallel plate capacitor configuration which allows the application of an electric field. At the same time, the top Pt layer acts as a detector of the AFM state. Due to the magnetic proximity effect (covered in section 2.2)) the Pt interface couples magnetically to the AFM making possible to detect electrically the state of underlying Cr_2O_3. As can be seen in Figure 1.4b, in a small temperature window the application of the electric field across the capacitor with a voltage V_G allows to affect the magnetic configuration of Cr_2O_3 (moving from red to green domain or vice versa in Figure 1.4a). Since Cr_2O_3 has an out-of-plane easy axis, this change affects the Pt out-of-plane magnetization which allows a detection via the anomalous Hall effect (covered in Section 2.3).

Despite the small temperature window in which Cr_2O_3-based devices can operate, the global approach is very promising. On one side, other magnetoelectric materials can be tested as a replacement of Cr_2O_3 but, on the other, interfacial magnetic effects can provide a universal tool to access antiferromagnetism through electrical methods. This, even before being exploitable in AFM memory technology, could be a powerful instrument for the investigation of materials. Showing the universality of these effects and the informations which can be taken from antiferromagnets is the core of this thesis work.

1.3 Thesis Outlook

This first chapter reviewed some important results in the field of antiferromagnet spintronics. The potential advantages of a purely antiferromagnetic memory support over ferromagnetic system have been underlined, namely the higher packing capability, the

robustness against magnetic perturbation, and the faster switching dynamics. In this context, the purpose of the present work is to develop a universally applicable method to access electrically the antiferromagnetic state of a thin film, either metallic or insulating, through interface effects with non-magnetic metals (Pt,Ta) and the measurement of anomalous Hall effect. An ultralow-noise electrical setup, which can be easily and economically reproduced in most of the experimental laboratories, has been employed to detect the antiferromagnetic state of metallic (Cr,IrMn) and insulating (tetragonal-Cr_2O_3,$TmFeO_3$) thin films. Obtaining positive results in all the cases investigated.

The thesis will develop in the following chapters:

- Chapter 2 reviews the basic theory of antiferromagnetic systems and of the concepts that will be employed in the rest of the work: magnetic proximity effect, anomalous Hall effect, anisotropic and Spin-Hall magnetoresistance.

- Chapter 3 presents the experimental techniques employed for the growth of samples, the fabrication of devices and the characterization, with a specific focus on the experimental setup for longitudinal and transverse resistance measurement on antiferromagnetic samples, showing its application on a Ta/IrMn system.

- Chapter 4 covers the results on Pt/Cr, proving the strict correlation between the presence of anomalous Hall effect and the antiferromagnetic state of the system and demonstrating a proximity induced magnetic moment in Pt backed also by *ab initio* calculations.

- Chapter 5 describes both the synthesis and the demonstration of antiferromagnetism in a tetragonal phase of Cr_2O_3 that we stabilized by epitaxy [7]. Interface effects again with a Pt layer allowed to verify the antiferromagnetic ground state predicted by *ab initio* calculations and to determine its transition temperature to paramagnet at about 40 K.

- Chapter 6 presents the investigation done on $TmFeO_3$, starting from the optimization of the epitaxial growth of thin films of this material to the verification of its antiferromagnetic nature in Pt/$TmFeO_3$ bilayers up to (at least) 300 K.

- Chapter 7 drafts the conclusions that can be taken on these results with an eye on future perspectives.

Theoretical background

This chapter reviews the fundamental physics of antiferromagnetic systems and interfacial effects with non-magnetic layers. Section 2.1 covers the origin of antiferromagnetic ordering in condensed matter with specific attention to the case of spin density wave antiferromagnetism in Chromium. The origin of proximity effects at magnetic/non-magnetic interfaces is covered in section 2.2. The transport properties which can arise in magnetic systems, i. e. anomalous Hall effect and magnetoresistance, are covered in section 2.3 and 2.4, respectively.

2.1 Antiferromagnetism

In an antiferromagnetic (AFM) material the magnetic moments, or spins, are coupled and their exchange integral, as opposed to ferromagnets, is negative. As such, the alignment of neighboring spins is antiparallel and, even if a long-range magnetic ordering is achieved, localized moments cancel each other out and no net magnetization arises. Simple antiferromagnets can be effectively described as two interpenetrating ferromagnetic (FM) sublattices coupled antiparallely. AFMs present a variegated landscape of possible configurations; already in a simple cubic cell there are several possible spin lattices as shown in Figure 2.1, resulting from all the possible exchange couplings that different systems can present.

The spin configuration justifies the three key properties of antiferromagnetic materials:

1. Zero net magnetic moment

2. Lack of stray field

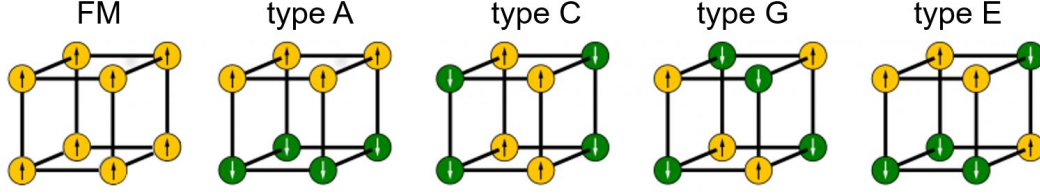3. Robustness against magnetic perturbations

Figure 2.1: *Ordered magnetic configruations in a simple cubic lattice: ferromagnetic (FM) and possible antiferromagnetic types.*

It is clear that the sum of magnetic moments in an ideal and infinite AFM crystal is zero as the two sublattices fully compensate each other. As a result no stray field would be expected outside the material. Finally, the robustness against external fields due to a low magnetic susceptibility can be intuitively understood considering the enormous cost in terms of exchange energy that would come from forcing a parallel alignment of neighboring spins.

A more quantitative, but still elementary, description of AFMs can be obtained from the Weiss model. [45] The two ferromagnetic sublattices can be thought independently aligned by an internal molecular field $B_\uparrow$ ($B_\downarrow$) and the antiparallelism is imposed by assuming each of those fields to be proportional only to the magnetization of the other sublattice:

$$B_{\uparrow(\downarrow)} = -|\lambda| M_{\downarrow(\uparrow)} \tag{2.1}$$

where λ indicates the exchange interaction strength.

In each sublattice the relationship between magnetization M and saturation magnetization M_s is given by the Brillouin function $B_J(y)$

$$\frac{M}{M_s} = B_J(y) = \frac{2J+1}{2J} \coth \frac{2J+1}{2J} y - \frac{1}{2J} \coth \frac{1}{2J} y \tag{2.2}$$

where J is the total angular momentum quantum number and y is a function of field

$$y = \frac{\mu_B g_J J B}{k_B T} = \frac{\mu_B g_J J(|\lambda|M)}{k_B T} \tag{2.3}$$

μ_B is the Bohr magneton, g_J is the Landé factor, k_B is the Boltzmann constant, and T is the temperature. We consider for the moment the molecular field as the only magnetic field present. The simultaneous solution of Equations 2.2 and 2.3 yields a different number of values for M depending on T. Defined T_N

$$T_N = \frac{\mu_B g_J \lambda (J+1) M_s}{3k_B} \tag{2.4}$$

we have two stable solutions with $M \neq 0$ for $T < T_N$, and $M = 0$ as the only solution for $T > T_N$. Hence, a magnetically ordered state can only be observed below the critical temperature T_N which is called, in the context of AFMs, Néel temperature after Louis Néel . Above T_N the system became paramagnetic (PM), except for some notable exceptions like FeRh which undergoes a transition to the FM state. As could be expected intuitively, a stronger exchange coupling λ determines a larger T_N, as thermal excitations cannot perturb the ordered state because of the larger exchange energy.
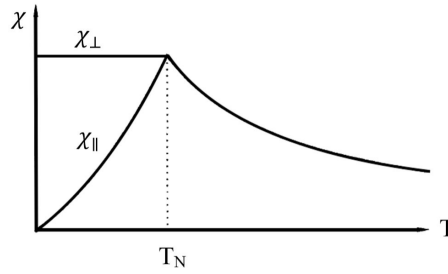
Figure 2.2: *Temperature dependence of susceptibility in an antiferromagnetic system.*

Considering now the impact of an external field $\mathbf{B} = \mu_0 H$ (μ_0 is the vacuum permeability), we introduce the magnetic susceptibility $\chi = \mu_0 M/B$. We treat separately the two temperature regimes for the AFM phase ($T < T_N$) and the PM phase ($T > T_N$), a schematic graph of susceptibility in an AFM system is reported in Figure 2.2. For $T > T_N$ and small magnetic fields we can take the first order expansion of the Brillouin function (Equation 2.2), now including the external field as well, and obtain a susceptibility inversely proportional to the temperature

$$\chi = \lim_{B \to 0} \frac{\mu_0 M}{B} \propto \frac{1}{T + T_N} \tag{2.5}$$

This has the same functional dependence of the Curie law for paramagnetic systems [46] reduced by the additional T_N term at denominator.

For $T < T_N$ the situation is complicated because the magnetic field orientation is crucial and the susceptibility is highly anisotropic. It is thus convenient to distinguish the cases in which the magnetic field is either parallel ($\chi_{\parallel}$) or perpendicular ($\chi_{\perp}$) to the magnetic sublattice. In the low temperature limit $T \approx 0$, an external field parallel to the spins would only add up to one molecular field at the expense of the other. In any case each sublattice is saturated and no change of magnetization is expected, therefore the parallel susceptibility results $\chi_{\parallel} = 0$. When the temperature increases, thermal fluctuations reduce each sublattice magnetization and now the magnetic field can progressively affect more and more the two magnetizations favoring one of the two orientations. Hence, $\chi_{\parallel}$ monotonously grows until T_N is reached.

If, instead, the external field is perpendicular to the spins, both sublattices can tilt in its direction. This canting of magnetic moments produce a magnetization which loosely depends on temperature (since the two sublattices are affected symmetrically by the temperature raise) so $\chi_{\perp}$ is different from zero and almost constant below T_N.

Finally we discuss the effect of large magnetic fields (comparable with the molecular field) in the AFM phase, once more the phenomenology is related to the magnetic field direction as depicted in Figure 2.3. If the field is applied perpendicular to the spins (Figure 2.3a), the canted state (Figure 2.3(I)) increases its tilting with field until complete alignment is achieved. If the field is applied parallel to the sublattice magnetization (Figure 2.3b), at a critical field (dependent on the magnetic anisotropy of the specific material) the configuration suddenly jumps from the antiparallel state (Figure 2.3(II)) to the so called spin-flop state (Figure 2.3(III)).
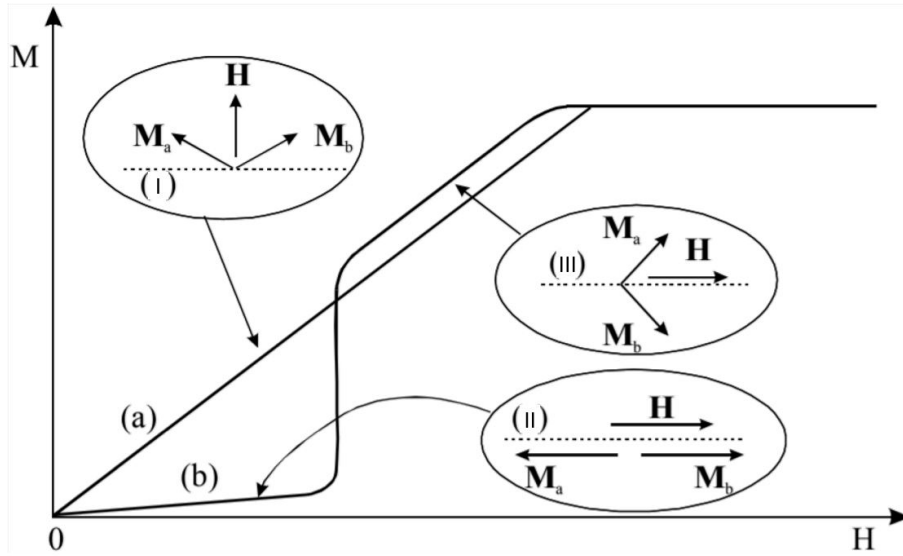
Figure 2.3: *Magnetization curve of an antiferromagnetic system. (a) Field perpendicular to the spin axis, (b) Field parallel to the spin axis. The insets noted as (I-III) indicate the canted state, the antiparallel state and the spin-flop state, respectively.*

2.1.1 Spin Density Wave antiferromagnetism

In this part we spend a few words on chromium, one of the antiferromagnetic systems that we studied and that will be presented in Chapter 4. Chromium is the prototypical Spin Density Wave (SDW) antiferromagnet: because of its peculiar electronic structure, Cr develops spontaneously an oscillatory magnetization as sketched in Figure 2.4. [47] The SDW period is generally a non-integer multiple of the crystal unit cell, hence the SDW is said to be incommensurate. The spin modulation wavelength changes with temperature continuously from about 21 unit cells at 80 K to 28 at T_N=311 K. In the bulk, spin polarization $\mathbf{S}$ can be either parallel or orthogonal to the SDW wavevector $\mathbf{Q}$ depending on temperature. Below the spin-flip transition $T_{sf} \approx 123$ K, a longitudinal SDW wave is observed with $\mathbf{S} \parallel \mathbf{Q}$, otherwise a transverse SDW with $\mathbf{S} \perp \mathbf{Q}$ is found.

The AFM ordering impacts on the electronic structure of Cr as well. In fact, as the SDW is formed, a gap opens in the Fermi surface, resulting in a decrease of free carriers which can be electrically detected. [48] While these properties are known since decades for bulk Cr [47], the study of thin films is more recent and proves some substantial difference from the bulk case. First of all the Néel temperature is found to be dependent on film thickness and residual strain from the substrate [49]. The spin-flip transition is not observed and the only stable configuration is the out of plane longitudinal SDW. [50–52] We note, however, that the presence of a metallic capping layer deposited on Cr films can affect the type of SDW producing in some cases complex magnetic phase diagrams. [53] In any case, since thin films always maintain a SDW ordering, this implies once again a gap opening at Fermi level in the antiferromagnetic phase. The resulting decrease of free carriers allows to assess electrically the Néel temperature [54] in an independent way from the interface effects that we are going to demonstrate in Chapter 4.
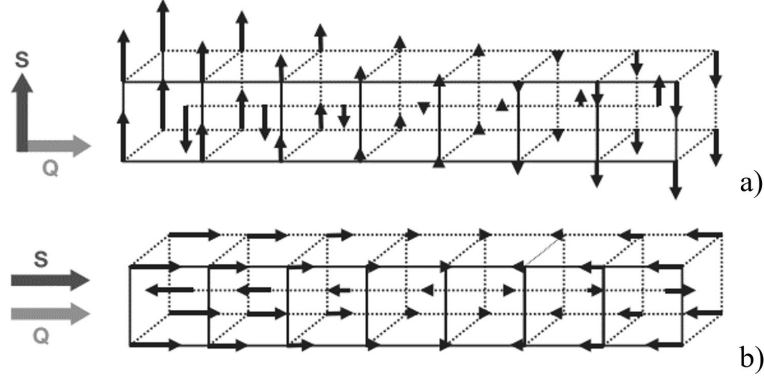
Figure 2.4: *Sketch of the spin density wave antiferromagnetic order in chromium, the incommensurate SDW extends over multiple unit cells. a) Transverse SDW. b)Longitudinal SDW. Reprinted with permissions from [54].*

2.2 Stoner instability and magnetic proximity effect

While the Weiss molecular field is a good phenomenological model for solids with localized magnetic moments, a description for ferromagnetic ordering in metals, where the electronic states are highly delocalized, can be obtained through the Stoner model.

In the free electron model, energy levels are occupied up to the Fermi level E_F and, as no spin-dependent term is present in the Hamiltonian, states with opposite spin orientation are degenerate, thus determining a non-magnetic ground state.

Introducing the exchange interaction spin degeneracy is lifted and, if this results energetically favorable, a ferromagnetic ground state can develop. In this case the effect of exchange interaction on the electronic dispersion consists of a spin-dependent energy shift as shown in Figure 2.5. The different number of electrons in the spin-split bands results in a net magnetization of the electron gas. This configuration has an increased kinetic energy with respect to the unperturbed state, and a ferromagnetic ground state can be energetically stable if the exchange interaction compensates for that.

In first approximation the increase of kinetic ΔE_K energy related to a rigid shift ∂E of the two sub-bands (as picture in Figure 2.5) is

$$\Delta E_K \approx \frac{1}{2} g(E_F) \partial E^2 \tag{2.6}$$

where $\frac{1}{2} g(E_F) \partial E$ is the density of carriers shifting in energy of ∂E. By defining $n_\uparrow$ the majority and $n_\downarrow$ the minority carrier density, and considering a magnetic moment per electron equal to $\pm \mu_B$, the gas magnetization is $M = \mu_B(n_\uparrow - n_\downarrow)$. In a mean field approximation, as previously used in the Weiss model, the molecular field is again linear in the order parameter as $B_{mf} = \lambda M$. In this case the potential energy gain due to the exchange interaction is given by the integral of the Zeeman term $E = -\mu \cdot \mathbf{B}(\mathbf{M})$ between 0 and M:

$$\Delta E_P = - \int_0^M \mu_0(\lambda M') dM' = -\frac{1}{2} \mu_0 \lambda M^2 = -\frac{1}{2} \lambda \mu_0 \mu_B^2 (n_\uparrow - n_\downarrow)^2 \tag{2.7}$$

Introducing the term $U = \mu_0 \mu_B^2 \lambda$, with U that gives a measure of the Coulomb
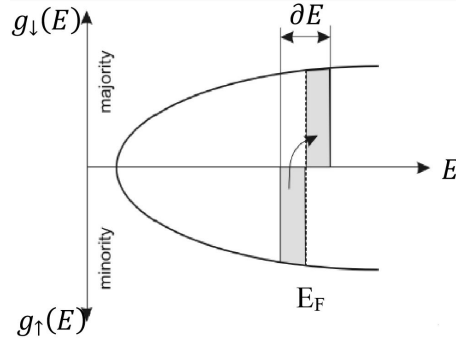
Figure 2.5: *Energy-split bands in metallic ferromagnet. The imbalance between electrons with minority and majority character determines a net magnetization.*

energy, we can simplify the expression into

$$\Delta E_P = -\frac{1}{2}U(g(E_F)\partial E)^2 \tag{2.8}$$

The total energy change of the system, given by the sum of the kinetic and potential parts is thus

$$\Delta E = \frac{1}{2}g(E_F)\partial E^2(1 - Ug(E_F)) \tag{2.9}$$

A ferromagnetic ground state can be thus expected if and only if ΔE is negative i. e. if

$$Ug(E_F) > 1 \tag{2.10}$$

which is the so called Stoner criterion. Therefore, the appearance of ferromagnetic order in metals has to be related with strong Coulomb interaction and large density of states around the Fermi level. Apart from the $3d$ transition metals, Fe, Co, Ni, no other bulk element satisfies the Stoner criterion in standard conditions. Nevertheless, some elements are very close to meet the requirements for a ferromagnetic ground state with the notable cases of Pd and Pt. [55] These materials on the verge of Stoner ferromagnetism can actually develop a magnetic order for slight modification of the electronic structure. This is possible for instance by doping with magnetic impurities, [56, 57] applying an electric field, [58, 59] or, in multilayers, interfaced with magnetic layers. The latter case, which goes by the name of magnetic proximity effect (MPE), has been demonstrated by X-ray magnetic circular dichroism (XMCD) for Pt interfaced with Fe, [60] Co, [61] and Ni [62]. Similar behavior has been observed for other non-magnetic $5d$ metals like Ir or W. [63])

MPE has been also invoked to explain some transport properties of Pt on insulating Yttrium Iron Garnet, [64] although this is still debated. [65] More recently, MPE in Pt has been exploited to detect the state of a neighboring magnetoelectric antiferromagnet Cr_2O_3[12], [13], demonstrating it also as a valuable probe in the context of the emerging antiferromagnetic-based spintronics [21] as we will cover in more detail in the next chapters.

2.3 Anomalous Hall Effect

Anomalous Hall Effect (AHE) was discovered by E. H. Hall in 1881 when he reported a transverse voltage in magnetized iron an order of magnitude larger than the one appearing in other non-magnetic metals. This effect could not be explained in terms of the Lorentz force. The dependence is non linear with the out-of-plane magnetic field H_z and is hysteretic. An empirical relationship has been enstablished with the out-of-plane magnetization M_z of the material.

$$\rho_{xy} = R_0 H_z + R_s M_z \tag{2.11}$$

R_0 and R_S are respectively the ordinary and the anomalous Hall coefficient. The classical measurement scheme for AHE is the same for ordinary Hall experiments and is reported in Figure 2.6a. A current J passes through the material and a transverse voltage is monitored while the out-of-plane magnetic field is changed. An example of anomalous Hall signal, expressed as transverse resistance $R_{xy} = V_{xy}/I$, is shown in Figure 2.6, the large transverse signal coming from the anomalous Hall effect of an out-of-plane magnetized CoFeB ultrathin film makes the linear component due to the ordinary Hall effect not even appreciable.

A theoretical explanation of the physical origin of AHE took more than 70 years from its discovery. After the work of Karplus and Luttinger, [66] it is well established that the fundamental origin of the anomalous Hall effect comes from the simultaneous presence of spin-orbit coupling (SOC) in the solid and broken time inversion symmetry coming from the magnetization. Other than this intrinsic contribution due only to the band structure of ferromagnets with SOC, also extrinsic contributions due to scattering at impurities can induce a transverse voltage. Such contributions, *skew scattering* [67] and *side jump* [68], however, still require the presence of SOC and net magnetization in order to have a non-vanishing transverse velocity.

AHE is thus widely considered an intrinsic property of ferromagnetic materials only, antiferromagnets indeed lack a net magnetization and AHE is generally not arising. Recently, however, antiferromagnets with non-collinear spin structure like Mn_3Sn, [69] Mn_3Ge, [70] and $Cr_{0.68}Se$ [71] have been reported for large AHE. In this case the transverse velocity has a topological origin, being related to the non-collinear spin structure
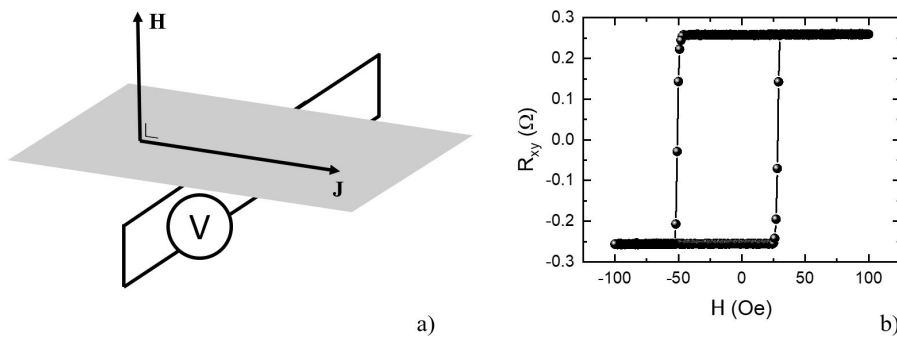

Figure 2.6: *a) Sketch of the experimental configuration for the measurement of AHE in a ferromagnetic metal: the out-of-plane magnetic field* **H** *is varied while monitoring the transverse resistance. b) Anomalous Hall resistance of a sputtered CoFeB ultrathin film (0.8 nm) with out-of-plane easy axis*

whose chirality determines a non-vanishing Berry phase for the traveling electron.

Whereas this topological AHE is a peculiar property of these materials, a much broader class of antiferromagnets can be possibly investigated by exploiting the AHE in a proximal layer, as reported in the case of Pt/Cr_2O_3 [43,72] and in this thesis on Cr (Chapter 4), tetragonal Cr (III) oxide (Chapter 5) and $TmFeO_3$(Chapter 6).

2.4 Magnetoresistance

The change in resistance R of a material or, more generally, of layered systems upon the application of a magnetic field H goes under the name of magnetoresistance. The relative change of resistivity is taken as a figure of merit for this effect as

$$\frac{\Delta\rho}{\rho} = \frac{R(H) - R(0)}{R(0)} \tag{2.12}$$

Different types of magnetoresistance (MR) can be observed and devices can be engineered to exploit technologically MR for memory and sensor applications. For the purposes of this work we will just introduce the phenomenology of two magnetoresistive effects, namely the anisotropic magnetoresistance and the spin-Hall magnetoresistance that will be discussed in the following sections.

2.4.1 Anisotropic Magnetoresistance

The anisotropic magnetoresistance, or AMR, is found in ferromagnetic metals. As first reported by Lord Kelvin in 1857 [73], this effect depends on the relative orientation of magnetization with respect to the current flow.

AMR is generally defined as:

$$AMR = \frac{\rho_\parallel - \rho_\perp}{\rho_{av}}; \qquad \rho_{av} = \frac{1}{3}\rho_\parallel + \frac{2}{3}\rho_\perp \tag{2.13}$$

with $\rho_\parallel$ ($\rho_\perp$) the metal resistivity for current parallel (perpendicular) to the magnetization axis. The dependence of AMR on the angle θ between magnetization $\mathbf{M}$ and current $\mathbf{J}$ follows a $\cos^2$ law:
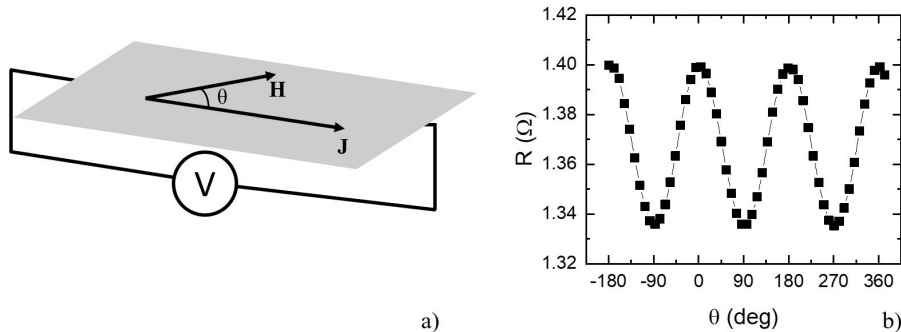

Figure 2.7: *a) Sketch of the experimental configuration for the measurement of AMR in a ferromagnetic metal: the angle θ between magnetic field $\mathbf{H}$ and current $\mathbf{J}$ is varied while monitoring the metal resistance. b) Resistance of a NiFe structure in a magnetic field H = 100 Oe as a function of θ. The π-periodic oscillation follows equation 2.14.*

$$\rho(\theta) = (\rho_\parallel - \rho_\perp)\cos^2(\theta) + \rho_\perp \tag{2.14}$$

The typical amplitude of AMR in $3d$ ferromagnets, in the order of few percents, and its angular dependence are shown in Figure 2.7. Figure 2.7a shows the typical measurement configuration for AMR, where the angle θ between the magnetic field $\mathbf{H}$ and the current flow $\mathbf{J}$ is varied continuously while monitoring the resistance. Figure 2.7b shows the actual AMR of a e-beam evaporated NiFe structure in a field of 100 Oe which is large enough to saturate its magnetization. Consistently with equation 2.14, it is possible to appreciate the π-periodic oscillation of resistance with its maximum at $\mathbf{H} \parallel \mathbf{J}$ and its minimum for $\mathbf{H} \perp \mathbf{J}$.

2.4.2 Spin Hall Magnetoresistance

While AMR is an intrinsic property of ferromagnetic metals, the spin-Hall magnetoresistance, or SMR, described in this section is intimately bound to what happens at the interface between a magnetic material and a metal with strong spin orbit coupling. In the latter, the presence of spin Hall effect and inverse spin Hall effect determine an interconversion between charge and spin current which is affected by the magnetization of the first layer.

Spin Hall effect (SHE) in solids determines a deflection in electron transport depending on their spin orientation. [74] This induces a spin accumulation on the lateral surfaces of samples where a charge current is flowing. The spin current j_S is always orthogonal to the charge current j_C as shown in Figure 2.8. No magnetization of the material is needed for the effect to occur, but in analogy to the Hall effect a fictitious magnetization can be associated to the layer (see Figure 2.8a). Noteworthy, the sign of j_S and its relative amplitude to j_C are properties of the specific material. Seizable spin current generation can be observed in materials with large spin orbit coupling like Pt, Ta and W. Where SHE is present, the inverse mechanism or ISHE can be also observed (see Figure 2.8b). In this case the spin current is converted into a transverse charge current.
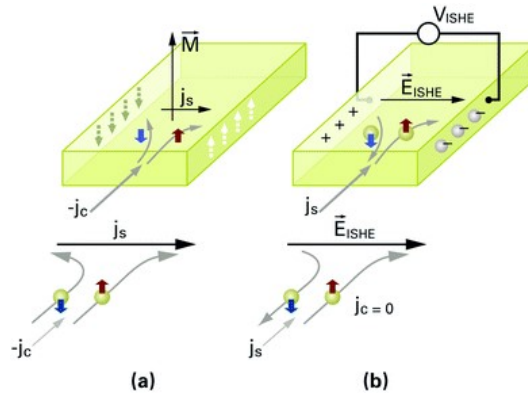

Figure 2.8: *Schematic illustration of the (a) spin Hall effect (SHE) and (b) inverse spin Hall effect (ISHE). The labels indicate the relative orientation of the associated magnetization ($\mathbf{M}$), electric field ($\mathbf{E}$), and charge (j_C) or spin (j_S) currents. The SHE converts an incident charge current into a transverse spin current, while the ISHE converts an incident spin current into a transverse electric field. Reprinted with permission from [75]*
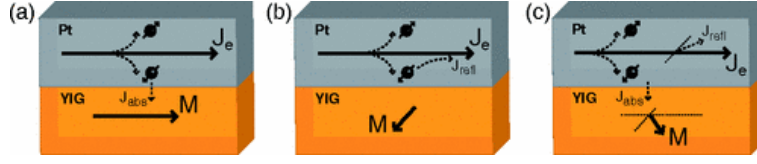
Figure 2.9: *Schematic drawing explaining the SMR in a Pt/YIG system.(a) When the magnetization* $\mathbf{M}$ *of YIG is perpendicular to the spin polarization σ of the spin accumulation created in the Pt by the SHE, the spin accumulation will be absorbed (*$\mathbf{J_{abs}}$*)(b) For* $\mathbf{M}$ *parallel to σ, the spin accumulation cannot be absorbed, which results in a reflected spin current back into the Pt, where an additional charge current* $\mathbf{J_{refl}}$ *will be created by the ISHE. (c) For* $\mathbf{M}$ *in any other direction, the component of σ perpendicular to* $\mathbf{M}$ *will be absorbed and the component parallel to* $\mathbf{M}$ *will be reflected, resulting in a current* $\mathbf{J_{refl}}$ *which is not collinear with the initially applied current* $\mathbf{J_e}$*. Reprinted with permission from [77]*

SMR originates from the interplay between (I)SHE and magnetization-dependent leakage of the spin current through the interface between non-magnetic metal and magnetic layer. As SMR is easier to disentangle from other MR effects if the magnetic material is insulating, the first system in which SMR has been studied is the bilayer made by non-magnetic Pt and the ferrimagnetic insulator Yttrium Iron Garnet (YIG). [76] A pictorial view of the processes leading to SMR is presented in Figure 2.9. Charges passing through Pt are subject to the SHE which deflects the electrons either up or down, in the section, depending on their spin. The resulting spin current can diffuse through the interface with YIG depending on the ferrimagnet magnetization direction. We distinguish three cases:

- *Magnetization orthogonal to the spin polarization* (Figure 2.9a). In this case the spin current diffuses in the insulator transferring angular momentum i. e. exerting a torque to the local moments in YIG. This results in the dissipation of the spin current.

- *Magnetization parallel to the spin polarization* (Figure 2.9b). Here no momentum can be transfered to YIG. Without dissipation the spin current can be reflected back without scattering in the non-magnetic layer where is subject to the inverse spin hall effect. The reconversion into charge current impacts on the resistivity of the non-magnetic layer by reducing its value.

- *Intermediate cases* (Figure 2.9c) In general, the spin component perpendicular to the magnetization will be absorbed, whereas the parallel component will be reflected generating a charge current which is non-collinear with the current excitation.

A full theoretical description of SMR [78] yields an analytical expression for the longitudinal resistivity as a function of the transverse magnetization m_y in the magnetic layer, the resistivity $\rho = \sigma^{-1}$, the spin-Hall angle θ_{SH},the spin-flip diffusion length λ, and the thickness d_N of the non-magnetic layer.

$$\rho_{long} = \rho + \Delta\rho_0 + \Delta\rho_1(1 - m_y^2) \tag{2.15}$$

$$\frac{\Delta\rho_0}{\rho} = -\theta_{SH}^2 \frac{2\lambda}{d_N} \tanh\frac{d_N}{2\lambda} \tag{2.16}$$

$$\frac{\Delta\rho_1}{\rho} = \theta_{SH}^2 \frac{\lambda}{d_N} \operatorname{Re} \frac{2\lambda G_{\uparrow\downarrow} \tanh^2 \frac{d_N}{2\lambda}}{\sigma + 2\lambda G_{\uparrow\downarrow} \coth \frac{d_N}{\lambda}} \qquad (2.17)$$

Here $G_{\uparrow\downarrow}$ is the spin-mixing coefficient for the specific interface.

Using similar arguments a change in transverse resistivity can also be expected. Again from the theory: [78]

$$\rho_{trans} = \Delta\rho_1 m_x m_y + \Delta\rho_2 m_z \qquad (2.18)$$

$$\frac{\Delta\rho_2}{\rho} = -\theta_{SH}^2 \frac{\lambda}{d_N} \operatorname{Im} \frac{2\lambda G_{\uparrow\downarrow} \tanh^2 \frac{d_N}{2\lambda}}{\sigma + 2\lambda G_{\uparrow\downarrow} \coth \frac{d_N}{\lambda}} \qquad (2.19)$$

Here we note that if an out-of-plane component of magnetization is present (i. e. $m_z \neq 0$) a transverse component, linear with m_z, in the resistivity tensor can appear. This effect, phenomenologically equivalent to the anomalous Hall effect described in section 2.3, is called Spin-Hall Anomalous Hall Effect (SHAHE).

2.4.3 Symmetry discrimination between AMR and SMR

In case both AMR and SMR are present simultaneously, for instance because of a proximity magnetization induced in the non-magnetic metal, it is possible to exploit their different symmetry in order to disentangle the two components. In this regard, it is common to perform angle-dependent magnetoresistance measurements along three orthogonal axes. An example again considering YIG as the magnetic material is shown in Figure 2.10.

With the device in the xy plane, with current flowing parallel to x, we distinguish three rotation planes. In the xy plane the scan along the angular coordinate marked as α includes both sinusoidal contributions from AMR and SMR since we would expect a change proportional $\sin^2(\alpha)$ in longitudinal resistance both from equation 2.14 and 2.15. This changes when scanning in the yz along the angle β. In this case, the magnetization is always perpendicular to the current and no modulation would come from the AMR, thus isolating the sole SMR. Finally by repeating the measurement in the xz plane, along the γ angle, the m_y component in the ferrimagnet appearing in equation 2.15 is not affected, making possible to isolate only the AMR.

While this method is fine for disentangling the contribution to longitudinal resistivity change, it cannot be applied to the modulation in transverse resistivity. In fact, both AHE and SHAHE present the same symmetry with respect to the m_z component (see equations 2.11 and 2.18) and other strategies, depending on the specific case, can be used to check the leading term between the two. Finally, being SMR related to the real part of the spin-mixing conductance (equation 2.17) and SHAHE to the imaginary part (equation 2.19), the relative influence of spin-Hall based phenomena could be different for longitudinal and transverse magnetotransport. As an example, in the prototypical system Pt/YIG the leading term in determining the longitudinal magnetoresistance is SMR while in transverse magnetoresistance is the AHE coming from magnetic proximity. [79]

Finally, it is important to note that the mechanism of SMR can apply to antiferromagnetic systems as well. Recent works have shown SMR in heavy-metals interfaced
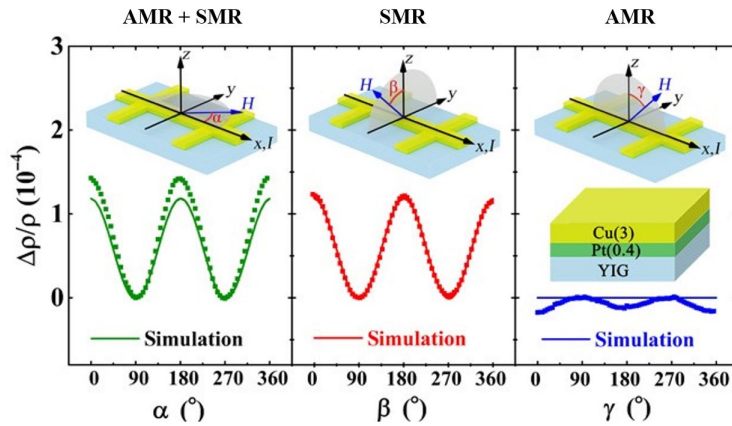
Figure 2.10: *Angular dependent magnetoresistance in Pt/YIG. From [80]. Reprinted with permission from AAAS.*

with AFMs. [81–87] In most of the cases a magnetic field above the spin-flop field (see Section 2.1) has been employed, therefore the magnetization axis of the AFM is perpendicularly-oriented to the applied field instead of parallel like in the case of YIG. As a result, the angular scans interested by SMR are shifted by 90°. In this case the SMR is said to be *negative*, as opposite to the ordinary "positive" SMR measured in YIG.

Experimental methods

This chapter introduces the most relevant methods employed for the growth, fabrication and measurement of antiferromagnetic-based devices. Thin film deposition technologies and equipments are described in section 3.1. The fabrication of devices through optical lithography processes is described in section 3.2. Finally, electrical measurements are covered in section 3.3 together with a description of the setup designed for sensitive offset-free Hall measurements.

3.1 Thin Film Growth

The following chapters will present results on several antiferromagnetic thin films and heterostructures, namely Pt/Cr, Pt/t-Cr_2O_3, and Pt/$TmFeO_3$. The growth of such materials was performed using some of the deposition techniques available either at Polifab or at JGU - Mainz. We will discuss here the main characteristics of each technique and the relevant process parameters involved.

Pt/Cr and Pt/t-Cr_2O_3 heterostructures were entirely fabricated in the cluster tool LASSE (Layered Artificial Structures for Spin Electronics) whose diagram is reported in Figure 3.1. [88]

The system allows for film growth by pulsed laser deposition (PLD) and molecular beam epitaxy (MBE), possibly combined without breaking the vacuum, and offers several characterization tools available *in situ* for electron diffraction and photoelectron spectroscopies. It is composed of five vacuum chambers through which samples up to 10×10 mm^2 can be moved using magnetic or mechanical transfer arms.

Chamber #1 is the introduction chamber which serves as a fast entry loadlock from which samples can be either moved towards the sample preparation chamber (Chamber #2) or the pulsed laser deposition chamber (Chamber #3). The latter features the optical access for the Nd:YAG laser as well as a gas inlet to maintain a controlled oxygen
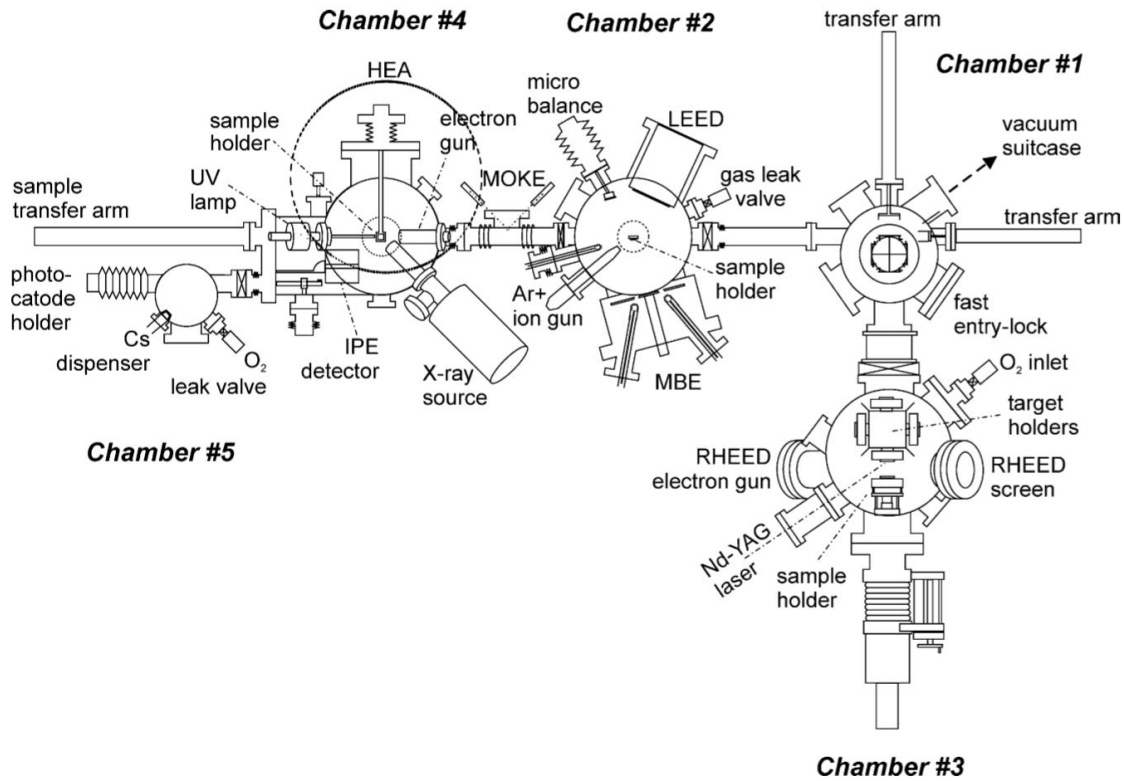
Figure 3.1: *Schematic diagram of the LASSE cluster (top view). High and ultra-high vacuum chambers are interconnected by gate valves and samples can be moved from one chamber to the others by means of magnetic and mechanical transfer arms. Reprinted with permission from [88]*

atmosphere during processes. A reflection high-energy electron diffraction (RHEED) gun designed for high pressure operation can be used to monitor the surface also in real time during the deposition. The sample preparation chamber allows for substrate pre-treatment by thermal annealing and/or argon-ion sputtering, includes seven evaporators for Molecular beam epitaxy of metals and oxides and a low-energy electron diffraction (LEED) system for surface analysis. Chamber #4 is the measurement chamber devoted to electron spectroscopies. Either an X-ray source or an He ultraviolet lamp can be used to excite photoelectrons from the sample surface which are then collected by an hemispherical electron analyzer (HEA). A setup for spin-resolved inverse photoemission (SPIPE) is also present and Chamber #5 is used for the preparation of photocatodes for such experiments.

All the chambers are isolated by gate valves except during sample transfer. Both the sample preparation and the measurement chamber operate in ultrahigh vacuum (UHV) regime, i. e. at a pressure lower than 10^{-9} mbar, in order to preserve samples from contamination as well as granting a sufficiently long mean free path for particles during MBE deposition and spectroscopy experiments.

3.1.1 Molecular Beam Epitaxy

Molecular beam epitaxy (MBE) has been used for the deposition of metals in Pt/Cr and Pt/t-Cr_2O_3 samples. In MBE the target material is heated in ultrahigh vacuum causing

either its evaporation or sublimation. The resulting flux of atoms travels towards the sample which is facing the evaporator and gets deposited on the surface.

Evaporation can be achieved both using resistive heaters (fine for semiconductors and metal with low vapor pressure) or electron-beams (which can be applied also to metals with high vapor pressure and oxides). The fundamental difference between MBE and conventional thermal or e-beam evaporators stands in the ultrahigh vacuum conditions in which the former is carried out. Because of the very low pressure the mean free path for atoms is in the order of meters, meaning that most of the material evaporated arrives on the substrate without any scattering event. This makes MBE highly directional and well suited for the growth of ordered epitaxial thin films. Moreover, the absence of almost any leftover reactive gas in the deposition chamber prevents contamination of the growing film. In order to achieve epitaxial growth, deposition rates are kept rather low (from few Å/min to few nm/min at most) and the substrate surface has to be clean and ordered. Atomic level control of the thickness can be achieved using mechanical shutter to open or obstruct the atom flux, and abrupt interfaces between layers can be obtained.

MBE has unparalleled potential within the physical vapor deposition techniques for the growth of semiconductor heterostructures but it can also be successfully employed for the growth of single-crystalline metals and oxides.

The MBE apparatus in LASSE consists of six confocal e-beam evaporators plus an additional one that can be moved close to the sample to get higher growth rates. In each evaporator, a tungsten filament can be made incandescent by passing a suitable current, freeing some electrons from its surface because of thermionic emission. Free electron are then accelerated towards the material to evaporate. To do so, an high positive voltage (between 500 and 3000 V) is applied to the high-purity metal rod or the metallic crucible containing the material.

Deposition rates are calibrated before each growth process with a quartz microbalance that can be moved in place of the sample.

3.1.2 Pulsed Laser Deposition

Pulsed layer deposition (PLD) has been employed in this work for the growth of $BaTiO_3$ seed layers for the epitaxy of t-Cr_2O_3 and for the deposition of antiferromagnetic $TmFeO_3$. Making possible to grow complex compounds maintaining the correct stoichiometry, PLD has found wide application mainly in the growth on fucntional oxides, like high-temperature superconductors, piezoelectrics, ferroelectrics and magnetic oxides. These compounds are typically based on ternary compound in the form ABO_x where A and B are different metallic species. Moreover, it is very common to include other elements as dopants to tailor specific functionalities. As precise composition is fundamental to achieve good functional properties, PLD has an edge over other techniques like co-evaporation from single constituents or sputtering (covered in the next section). The latter in fact, even if starting from stoichiometric targets, preferentially deposits species with higher atomic cross section with the process gas, losing accuracy in the film composition. At the contrary, the high-energy process of laser-assisted deposition ablates material independently of the elemental nature of constituents, thus making easier to maintain unaltered the stoichiometric ratio.

Figure 3.2 sketches of the PLD chamber in LASSE which also serves to explain
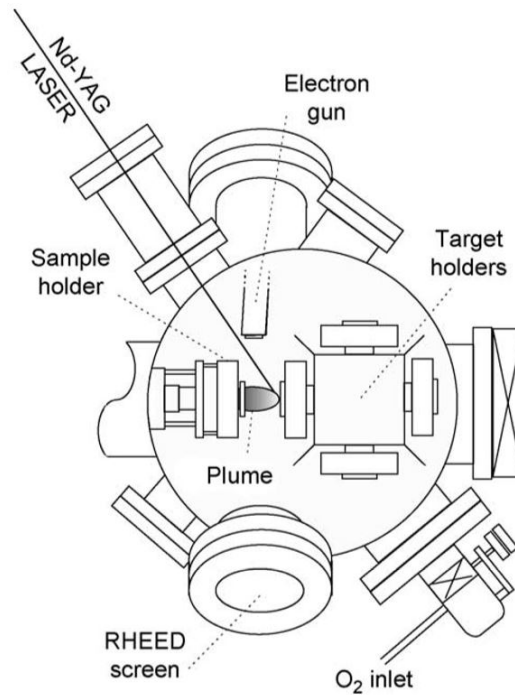
Figure 3.2: *Sketch of the pulsed laser depoition chamber in LASSE. Reprinted with permission from [88]*

the working principle of laser assisted deposition. An high energy pulsed laser beam, provided in LASSE by a Nd:YAG laser operating on the fourth harmonic ($\lambda = 266$ nm) in Q-switching regime, is focused on the surface of a ceramic target with the desired composition of the film to grow. The laser fluence on the target is above the ablation threshold of the material, and the absorption of ultraviolet light in few nanometers below the surface causes instantaneous heating up to 3000 K with consequent vaporization and ionization of the material. The continuous absorption of energy of the laser pulse increases the temperature and pressure inside the plasma that rapidly expands perpendicularly to the target, forming the characteristic *plume*. Chemical species move inside the plasma plume towards the substrate where they impinge and condensate.

The process is typically carried out with a background gas pressure of Argon or Oxygen, the latter is generally used for the growth of oxides to compensate for de-oxigenation and reduce the oxigen vacancies in the film. For this reason, in LASSE a controlled gas inlet provides a continuous oxygen flow, while the pressure is maintained constant using a proportional valve with automatic feedback regulating the downstream towards the pumping group.

During the growth, sample holder rotates while the laser beam can be rastered on the target to provide uniform material consumption and homogeneous thickness on larger area with uniformity of $\pm 10\%$ on 2.5 cm. An infrared lamp allows to maintain substrate temperatures up to 1000 K, required for the epitaxial growth of oxides.

The growth of TmFeO$_3$ has been carried out using the PLD setup in JGU-Mainz which features more or less the same components of the PLD in LASSE, but employs a KrF excimer laser (λ= 248 nm) instead of the quadrupled Nd:YAG source and an infrared diode laser for substrate heating.

24

3.1.3 Magnetron Sputtering

Magnetron sputtering has been used for the growth of Ta/IrMn thin films that will be shown in section 3.3.1 for validating the measurement setup for antiferromagnetic films and for the deposition of Pt in Pt/TmFeO$_3$. The sputtering process is carried out in an inert gas athmosphere (argon is used in most of the cases) inside a vacuum chamber. The material to be deposited is negatively biased with a high voltage. Under appropriate partial vacuum condition the acceleration of charged particles (both Ar$^+$ and e$^-$) by this bias causes the ionization of other neutral atoms leading to an avalanche process and to the plasma ignition. Positively charged argon ions, at this point, are still accelerated towards the target, bombarding the surface and transferring their momentum to atoms in the solid. This causes the ejection of the material in the form of neutral atoms, clusters or molecules. Once these neutrals are ejected, they can proceed with some scattering events toward the sample, finally getting incorporated in the growing film.

In the magnetron configuration, an array of permanent magnets placed behind the target confines electrons directly on top of the target surface. In this way, the free electrons repelled by the negatively charged target, cannot reach the substrate, where they could overheat the sample possibly causing structural damage. At the same time, the circular trajectories followed by electrons along the magnetic field flux line enhance by orders of magnitude the probability of ionizing neutral Ar atoms. As a consequence of the larger number of ions available, a significant increase of the deposition rate can be observed

3.2 Optical lithography

Ultraviolet optical lithography is the standard pattern transfer technique employed for micro and nanofabrication of devices. An ultraviolet radiation source (lasers or mercury gas-discharge lamps) is used to transfer a pattern from a properly designed 2D mask to a radiation sensitive polymer (the *photoresist*) deposited on sample surface. After selective exposition to the light and a proper developing process, only the desired areas of the sample remain covered with photoresist allowing for successive steps of deposition or etching.

The steps of lithographic process are illustrated in Figure 3.3.

0. **Sample cleaning**. Superficial contaminations have a bad influence on resist adhesion and on final resolution of the pattern. Cleaning is performed with an ultrasonic bath in acetone, rinse in isopropanol and a soft bake in order to desorb water.

1. **Photoresist deposition**. The image reversal photoresist AZ5214E from Micro-Chemicals GmbH has been used for device lithography. It consists of a photoactive compound (naphthoquinone diazide) in a Novolak resin matrix.

   The deposition from solution of phototoresist films 1.4 μm thick occurs via spin-coating. The sample is covered with some drops of liquid and put on rapid rotation so that the centrifugal force distributes the material uniformly on the sample surface. Thickness t of the resulting film depends on angular velocity ω and fluid
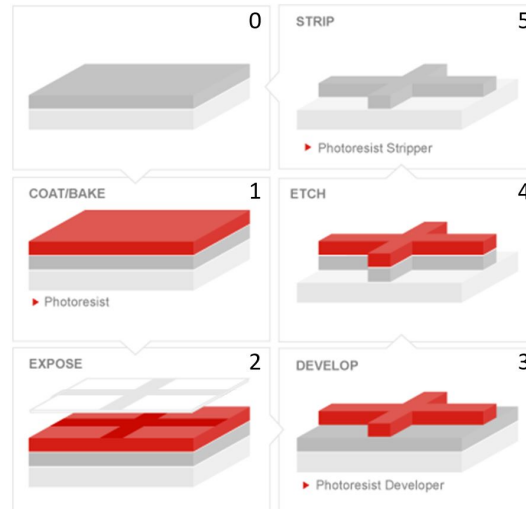
Figure 3.3: *Optical lithography process with positive resist and etching*

viscosity η accordingly to the empirical relation

$$t = K \frac{C^\alpha \eta^\beta}{\omega^\delta}$$

where K, α, β, δ are specific constants of the system.

The spin coating method provides a high processing speed and a high homogeneity of the layer thickness for films up to a few microns.

After the photoresist deposition, the solvent is evaporated by a soft bake at $110\,^\circ\text{C}$ for 50 seconds.

2. **Exposure**. The exposure to light radiation, over a certain dose, modifies the chemical properties of the photoresist, producing a different solubility of the exposed and unexposed part of the film. In the case of positive resist AZ 5214E, the exposed regions become more soluble and can thus be easily removed in the development process. UV radiation has been used and the image transfer is realized through a mask patterned with Cr: where the metals is present on the mask, it adsorbs the radiation protecting the underlying resist from the exposure. In this way it is possible to transfer the Cr pattern into a resist pattern on the sample.

    To align the mask to the sample in the various lithographic steps a Karl Suss MA8 mask aligner has been used; the UV source is the Hg-I line (365 nm) of a mercury lamp.

3. **Development**. During the developing process, an appropriate chemical agent (AZ726 MIF Developer from MicroChemicals GmbH) removes the part of resist not belonging to the image. In case of positive resist, the exposed part is dissolved, while the part protected from the light by the Cr mask remains onto the sample. For a negative resist the mechanism is just the opposite.

4. **Additive or subtractive processes**. As the sample is patterned, selective etching and/or material deposition can be performed. In the case of etching (done with
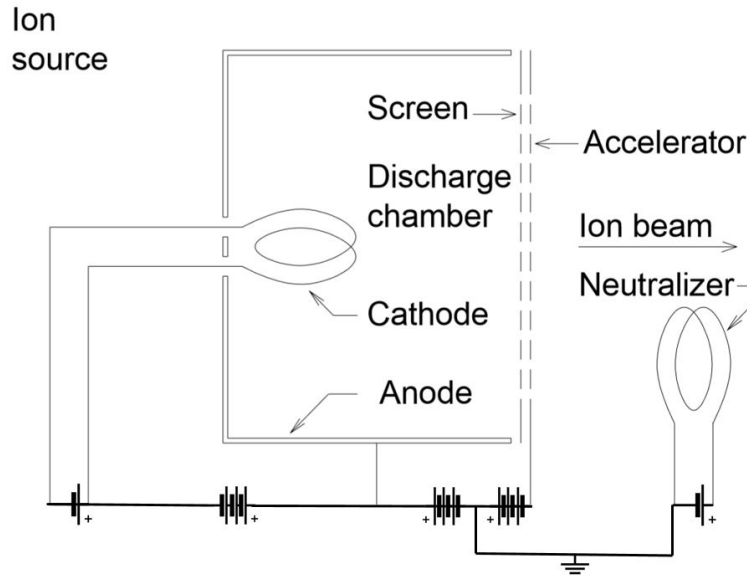
Figure 3.4: *Schematic of the Kaufman and Robinson KDC 160 Ion Source.*

the technique of ion beam etching described in section 3.2.1), resist protects the covered areas from being removed, whereas, in the case of deposition, it prevents the adhesion of material on the underlying layer.

5. **Strip or Lift-off**. Following subtractive processes, strip of the resist leaves only the parts that were covered in relief. Vice versa, in the case of additive processes, the *lift-off* of the resist removes the material deposited on top of the polymer, leaving the material only in correspondence of the exposed part of the sample. In both cases, samples were kept in AZ100 Remover from MicroChemicals GmbH in order to remove the remaining resist. To check the completion of the process, samples were carefully examined with an optical microscope.

3.2.1   Ion Beam Etching

Ion beam etching is a physical dry etching technique where Ar^+ ions are accelerated towards the sample in a vacuum chamber. Similarly to what happens with sputtering targets, the sample material is removed by momentum transfer between the accelerated Ar ions and the sample surface. Figure 3.4 reports a schematic diagram of the Kaufman and Robinson KDC 160 Ion Source that has been employed to fabricate devices in Polifab. A similar system was also available in the cleanroom in JGU-Mainz. In ion beam etching, Ar atoms are ionized by a current discharge and then accelerated towards the sample. In the discharge chamber, a hot cathode filament emits electrons by thermionic effect. These electrons, while moving towards the positively charged metal walls of the chamber which serve as anode, hit and ionize the Ar atoms. At this point, an accelerator grid set to a negative potential forces the Ar^+ ions outside of the discharge chamber towards the sample to be etched.

Being the plasma generation and the acceleration completely decoupled, it is possible to control independently the flux (increasing or decreasing the discharge voltage) and energy (acting on the acceleration voltage). Between the accelerator grid and the
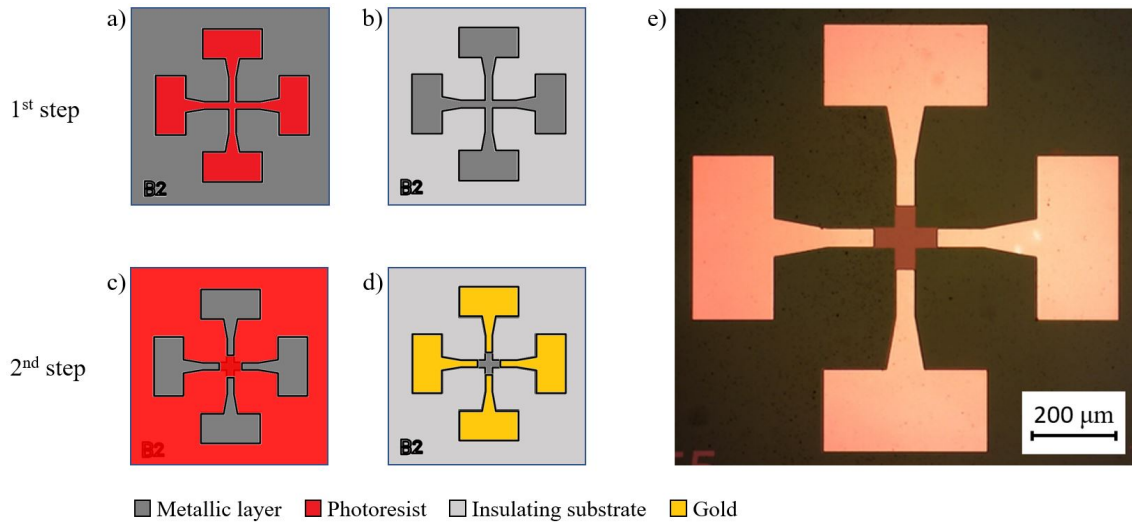
Figure 3.5: *Fabrication process of an Hall cross. a) Lithography of the cross structure. b) Patterned cross in the film by ion beam etching and photoresist strip. c) Lithography of the contact pads area. d) Cross with Gold contact pads. e) Optical image of a finished Pt/Cr//MgO device.*

sample, a second filament produces electrons by thermionic emission. These electrons avoid the positive charge build-up on the sample both neutralizing the Ar^+ ions of the beam before they reach the sample and directly compensating the positive charges on the sample surface. During the etching process, the sample holder is kept in rotation to ensure uniformity on the whole surface. Furthermore, it is possible to tilt the sample holder with respect to the incident beam by a desired angle (tipically $30°$) to avoid redeposition of material being etched.

3.2.2   Device fabrication

Devices that will considered in this work have an Hall cross geometry. This structure allows both longitudinal and transverse resistivity measurements and is optimal for realizing offset compensation schemes like the one that will be introduced in section 3.3.1. Here, we summarize the two step microfabrication process needed to realize the final device ready for characterization.

- 1st step: Hall cross definition (Figure 3.5a,b)

  1. Spin coating of 1.4 μm thick AZ5214E photoresist.
  2. Photoresist baking at 110 °C for 90 s to evaporate leftover solvent.
  3. Exposure to UV light with a dose of 125 mJ/cm^2.
  4. Development in AZ726 MIF developer for 1 minute and water rinse.
  5. Ion beam etching to remove all the unprotected metallic layer.
  6. Photoresist stripping

- 2nd step: Contacts pad deposition (Figure 3.5c,d)

  1. Spin coating of 1.4 μm thick AZ5214E photoresist.
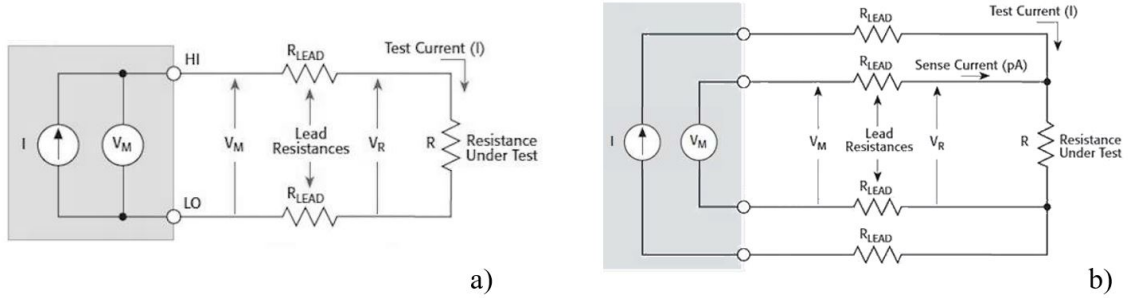 2. Photoresist baking at 110 °C for 90 s to evaporate leftover solvent.

Figure 3.6: *Electrical probing configurations. a) Two points measure. b) Four points measure (Kelvin sensing)*

3. Alignment and exposure to UV light with a dose of 50 mJ/cm^2.

4. Reversal bake at 110 °C for 90 s to crosslink polymer chains in exposed areas.

5. Flood exposure to UV light with a dose > 200 mJ/cm^2.

6. Development in AZ726 MIF developer for 45 s and water rinse.

7. Deposition by magnetron sputtering of Au(250)/Cr(50) contacts

8. Photoresist lift-off

The additional steps in the lithographic process for contact pad definition (number 4 and 5 in the 2nd step) are used to turn the positive AZ5214E to act as a negative photoresist so that the area exposed to UV though the mask remain insoluble during development. This process called *image reversal* is peculiar of the photoresist employed and defines an optimal resist profile for subsequent lift-off processes. [89]

The optical microscope image of one finished device is reported in Figure 3.5, the Hall structure has a Greek cross geometry with 50 μm wide and 150 μm long arms intersecting in the middle. Once patterned, the sample is prepared for electrical transport experiments by gluing it with thermally conductive paste on a suitable chip carrier and wirebonding the desired microstructure to electrically accessible copper pads.

3.3 Electrical characterization

Electrical measurements, although immediate and commonly available, require a careful design in order to remove artifacts, avoid common noise sources and achieve reliable results. A very simple resistance measurement with an Ohm-meter can be done in the two-point configuration like the one in Figure 3.6a. In this case, the two contacts serve both as a voltage probe and as injectors for the test current I. If the intention is to measure the resistance R of the device under test, given by the Ohm's law $R = V_R/I$, this method can give some errors. In fact, if the leads resistance R_{LEAD} in non negligible compared to R, the voltage V_M measured by the instrument can be sensibly different from V_R. In particular, looking at the diagram, the resistance measured is $R_M = V_M/I = 2R_{LEAD} + R$.

To get rid of the undesired term $2R_{LEAD}$ which not only accounts for the wire resistance but also for the intrinsic contact resistance which is typically unknown, a four point configuration like the one shown in Figure 3.6b is preferable. The current path

is the same as before, but the voltage drop across R is measured through other two probes on a parallel circuit. Even though this circuit can also be affected by contact and wire parasitic resistances, those will be dwarfed by the enormous input impedance of the voltmeter (from MΩ in low class instruments up to TΩ in high-end nanovoltmeters). The current flowing in this branch will be negligible with respect to the current loop and so will be the voltage drop across the leads. As a result the measured voltage $V_M = V_R$ and the correct value of R can be retrieved dividing by the known test current.

Another crucial issue in measuring small signals is the unavoidable presence of thermoelectric effects usually leading to spurious signals in the order of μV. Thermal gradients which give rise to the Seebeck effect can spontaneously appear on the sample or can be induced by Joule heating when a current is flowing. Seebeck voltage, however, retains its sign when the current is reversed and also Joule heating, which depends on the current squared, is independent on the sign. Therefore, in linear systems like the ones that we are going to deal with, thermoelectric offsets can be compensated by subtracting measurements repeated with opposite probe polarity.

All the measurements discussed in the following will employ four-wire sensing and the current reversal method for thermal offset compensation.

3.3.1 Magneto-transport measurements

Longitudinal geometry

The first transport property of interest in a conductive system is the longitudinal resistivity, also in relation to some possible magnetoresistive phenomena as discussed in section 2.4. An elegant result from Van der Pauw [90] states that the resistivity of a planar sample with arbitrary shape can be determined from two non-local resistance measurements provided that:

1. Sample is simply connected, i. e. there are no holes.

2. Contacts are placed close to the edge.

3. Contacts are significantly smaller than the distance between them.

4. Sample thickness is uniform.

Considering the Hall cross geometry that we discussed in section 3.2.2 the two Van der Pauw measurement configurations are the ones sketched in Figure 3.7. Two orthogonal non-local measurements or resistance can be performed by injecting a current in the contact pairs 1-4 and 1-2 as noted in the figure and measuring the voltage drop on the corresponding contacts 2-3 and 3-4.

If we define:

$$R_{1423} = \frac{V_{23}}{I_{14}}; R_{1234} = \frac{V_{34}}{I_{12}} \tag{3.1}$$

The sheet resistance R_s of the film can be found by solving the transcendental equation:

$$e^{\frac{R_{1423}}{R_s}} + e^{\frac{R_{1234}}{R_s}} = 1 \tag{3.2}$$

And therefore, from the thickness of the film t, the longitudinal resistivity ρ_{xx}
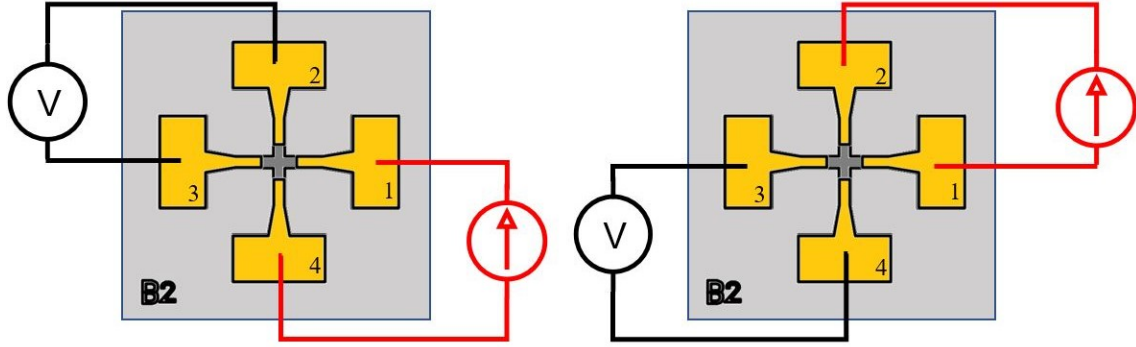
Figure 3.7: *Van der Pauw configuration for the measurement of resistivity in Hall crosses.*
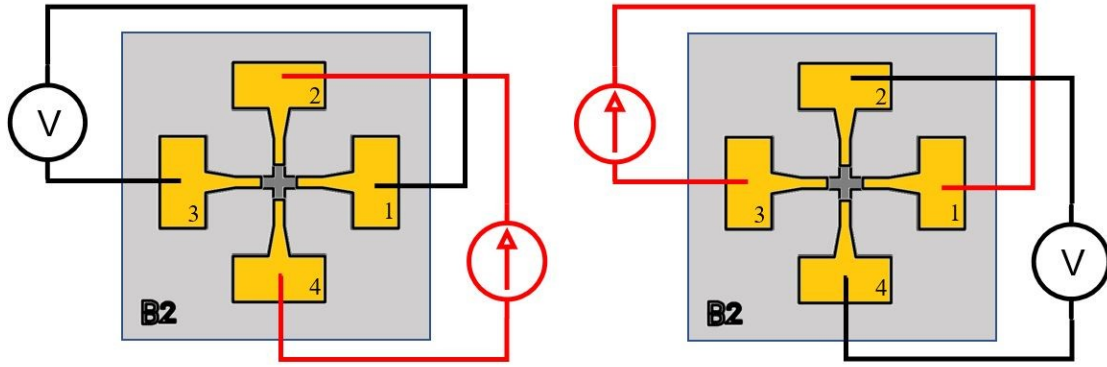

Figure 3.8: *Transverse resistance measurement configuration in Hall crosses.*

$$\rho_{xx} = R_s t \tag{3.3}$$

Transverse geometry

In transverse resistance or Hall measurements, the voltage drop perpendicular to the flowing current is measured. This situation is represented in Figure 3.8. Ideally the two configurations should be equivalent, i. e., using the subscript notation, R_{2413}=R_{1324}. This is however not true in reality. as the measured resistance R is unavoidably a linear superposition of the transverse term R_{xy} and a longitudinal component.

$$R(T, H) = R_{xy}(T, H) + p(H)R_{xx}(T, H) \tag{3.4}$$

where p is the factor that expresses the non-ideality of the cross. This geometrical factor should not depend on temperature, however it can be affected by the application of magnetic fields as we are going to discuss in the next section.

Generally, the leftover longitudinal term is large compared to the true transverse term. If this can be an annoyance when measuring the anomalous Hall effect in ferromagnets (the offset can be easily subtracted once the full hysteresis loop is measured) in the case of antiferromagnets this spurious signal would be destructive.
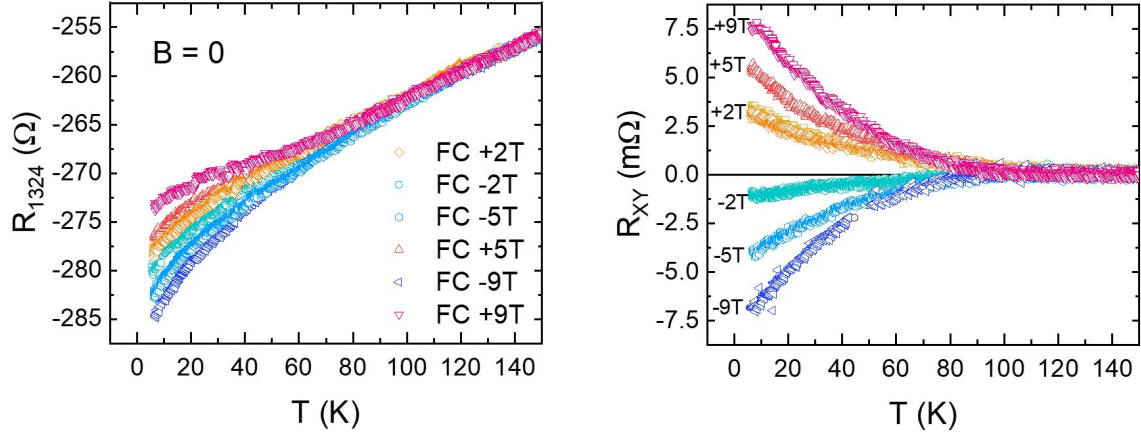
Figure 3.9: *Anomalous Hall effect measurement in Ta(2)/IrMn(4)/Ta(2)//SiO$_2$. a) R_{1324} without offset compensation b) with geometrical offset compensation using equation 3.5.*

It is however possible to remove the geometrical offset by adopting both contact permutations of Figure 3.8. In fact, Daniil and Cohen demonstrated [91] that the magnitude of the longitudinal voltage drop is identical in the two cases and $p_2 = -p_1$. Therefore, by averaging the two measurement, the longitudinal component cancels out leaving only the transverse term.

$$R_{xy} = \frac{R_{1324} + R_{2413}}{2} \tag{3.5}$$

To illustrate this, Figure 3.9 shows a measurement of anomalous Hall effect at remanence, with and without the offset compensation, in field cooled antiferromagnetic IrMn. A Ta(2)/IrMn(4)/Ta(2)//SiO$_2$ heterostructure grown by magnetron sputtering has been used for this purpose. Previous reports mentioned a non-zero anomalous Hall signal in Ta/IrMn, [92] making it an optimal testbed for the method. Indeed, repeated measurements on a device written by field cooling from above the Néel temperature $T_N \approx 100K$ with an out-of-plane field between -9 T and +9 T display a monotonic response to the writing field already in the plain transverse resistance R_{1324} (Figure 3.9a). However, this signal is offset from 0 by a geometrical factor of about 280 mΩ, which is almost 20 times larger than the magnetic signal. Instead, when the measurement is offset compensated point-by-point using equation 3.5, the transverse resistance of magnetic origin became nicely referenced at zero, as can be seen in Figure 3.9b.

Ta/IrMn among all the antiferromagnetic system that we studied is the one which has the larger magnetic signal and the smaller temperature coefficient of resistance, making the measurement sensibly easier. Therefore, in all the other cases that we are going to discuss in the next chapters, offset compensation is even more crucial to isolate a small variation over a large background. Finally, we emphasize that the transverse resistance measured in Ta/IrMn comes just from the uncompensated moments of the antiferromagnet and at the interfaces which can be set by field cooling. Measurement were performed at remanence, with the hysteresis of the superconducting coil used to apply the field compensated to have $H = 0 \pm 1$ Oe. The signal goes to zero exactly in correspondence of the Néel temperature and results unaffected by external fields (up to 9 T) below it, thus excluding a possible origin from a ferromagnetic contamination.
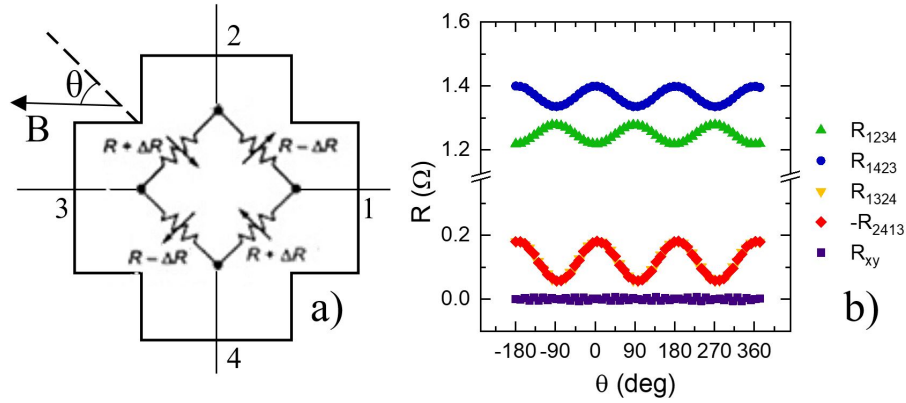
Figure 3.10: *a) Equivalent Whetstone bridge circuit of the Hall cross with a magnetic field applied in the plane of the field. b) Four-point resistance measured as a function of in-plane field angle: longitudinal (green and blue points) and transverse (yellow and red points). By averaging R_{1324} and R_{2413} the geometrical contribution can be compensated to isolate Hall effect R_{xy} (violet points).*

Planar Hall Effect

Even though the single transverse measurement R_{1324} (or R_{2413}) alone is affected by an undesired offset when looking for R_{xy}, conversely, it can be very effective in detecting variations of longitudinal R_{xx}. If we consider the equivalent circuit of the Hall cross represented by four resistors joining the cross arms (see Figure 3.10a) we can recognize the structure of a Wheatstone bridge. This resistor arrangement is typically employed in analog electronic circuit design to measure the value of a resistive sensor.

Here, each branch of the circuit can be seen as a magnetization sensor because of the previously discussed magnetoresistive phenomena (section 2.4. Using a ferromagnetic Permalloy thin film as a demonstrator we take the longitudinal resistances R_{1423} and R_{1234} orthogonal to each other (green triangles and blue points in Figure 3.10) as a function of the magnetic field direction (H=100 Oe)). The modulation ΔR due to anisotropic magnetoresistance is about 4.9% relative to R. Very importantly, when the resistance change is positive on one arm it is negative on the orthogonal one. This is exactly the situation of a fully balanced Whetstone bridge as schematized in Figure 3.10a. The full bridge is the most sensitive configuration possible in this scheme to detect just ΔR granting at the same time also an advantage in terms of temperature drift rejection. The red and yellow points which are superimposed in Figure 3.10 represent the value of R_{1324} and -R_{2413}, which allow the measurement of magnetoresistance exploiting the intrinsic Wheatstone bridge capability of the Hall cross. With respect to longitudinal measurements, the transverse configuration (R_{1324} or R_{2413} independently) presents larger modulation over a smaller offset, increasing the relative sensitivity by order of magnitudes. For this reason, similar configurations are massively used in magnetic sensor devices typically under the name of Planar Hall Effect sensors. Despite the name, this has nothing to do with the Hall effect. As a matter of fact we can once again average R_{1324} and R_{2413} to recover the true transverse voltage R_{xy}. Being the magnitude of the two identical and the sign opposite, the average leads to a constant zero value for R_{xy} consistently with the absence of any Hall effect as the field is applied in the plane.

3.3.2   Integrated setup for transport measurements

As we have just seen multiple informations can be readily accessed from a simple geometry like the Hall cross just by changing the contact configuration. The acquisition of both transverse and longitudinal resistance, compensating simultaneously geometrical and thermal offset, requires (at least) 8 independent measurements with related permutations of contacts and of current polarity. This is of course an operation that cannot be done manually in order to obtain a complete characterization of the transport properties in a reasonable time. Other than to speed up the whole process, a fast automated commutation between different contact configurations offers a more robust compensation of geometrical offsets in Hall measurements. In fact, if between the acquisition of R_{1324} and R_{2413} passes too much time and the temperature of the sample changes even by few mK, the geometrical offset will be no longer canceled as the sample resistivity will change as well because of temperature.

To meet these requirements, a simple relay switching matrix was specifically designed and realized for this purpose. The switching matrix redirects the four terminals of the instruments (two for the current source and two for the voltmeter) to the four contact pads of the device under test, making possible to collect all the transverse and longitudinal measurements consecutively within one second. Details on the implementation of the circuitry are reported in Appendix A.

Another key point is the choice of the measurement instrumentation. As we mentioned at the beginning of the chapter, an important feature for our setup is the use of current reversal to get rid of thermoelectric effects. There are two options in this regard: either using a sinusoidal excitation or applying an alternating positive and negative DC bias (like in a square wave). The first method would is typically apply together with lock-in demodulation amplifiers, however, even high-end commercial lock-ins are not particularly efficient for precise Hall measurements. In fact, two figures of merit of the amplifier used to read the voltage are fundamental here: input impedance and common mode rejection ratio (CMRR). The first is important to detect small signals while the second determines how good is the instrument in measuring a voltage difference between the inputs when both inputs are evenly lifted from the ground potential (by geometry in Hall crosses the common mode is always present and is approximately half of the voltage applied to the current line). Commonly available lock-in amplifiers present an input impedance of 1 MΩ and typically declare a CMRR of 100 dB (a factor of 10^5 rejection). By using instead nanovoltmeter (Keithley 2182A) the input impedance is 10 GΩ and, in combination with a DC current source (Keithely 6221), a CMRR of more than 200 dB ((a factor of 10^{10} rejection) is claimed. [93]

A schematic of the instrumental setup is reported in Figure 3.11a. A custom designed LabVIEW software communicates with the current source which, in tandem with the nanovoltmeter, performs measurements with the current reversal method. The acquisitions are coordinated with the switching of circuit permutations. In this case the software controls over serial line an Arduino board which drives the relays (see Appendix A). The software will also control the cryostat temperature and magnetic field where applicable.

The sample is wire-bonded to a non-magnetic holder serviced by copper wires for bringing the signals in and out the cryogenic environment. Silver paste or low-temperature varnish is used to fix the sample and ensure a proper thermal contact. The
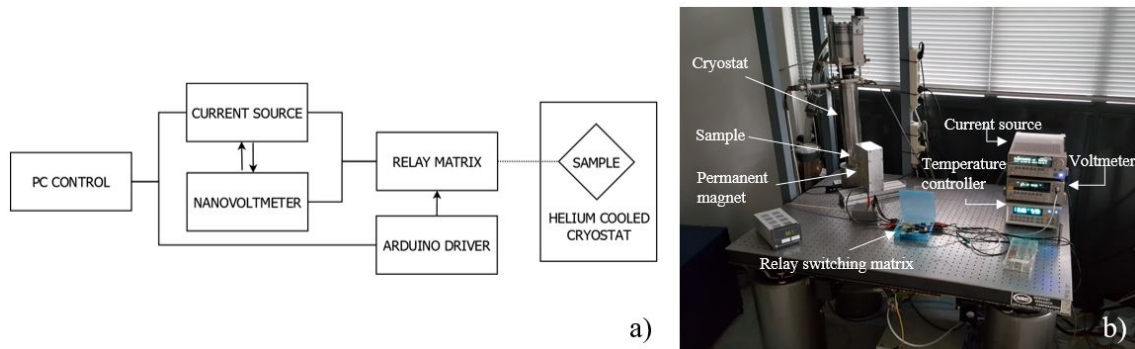
Figure 3.11: *a) Schematic diagram of the electrical measurement setup. b) Picture of the setup used for measurements on Pt/Cr (Chapter 4)*

setup used for measurements in Pt/Cr (Chapter 4) is pictured in Figure 3.11b. In this case, field cooling writing of the antiferromagnetic state is made possible by a permanent magnet in Halbach configuration providing a uniform field of 0.4 T. In other cases (Chapter 5 and 6), a superconducting coil has been used to provide larger fields. The components of the measurement setup are otherwise unchanged.

CHAPTER *4*

Magnetic Proximity and Anomalous Hall Effect in Pt/Cr bilayers

This chapter will cover the results on the electrical detection of the antiferromagnetic state in metallic chromium. In agreement with *ab initio* calculations, electrical measurements provide evidence of a proximity induced magnetization in Pt by neighboring antiferromagnetic Cr. The transverse resistivity at remanence, in fact, can be controlled in Pt/Cr/MgO heterostructures by field cooling the antiferromagnet across its Néel temperature.

In section 4.1, the theoretical predictions of a magnetized interface between Pt and Cr are reported. The experimental work supporting these predictions is presented in section 4.2 and 4.3 for the device fabrication and characterization, respectively. Finally, section 4.4 draws the conclusion of this work.

4.1 Results of *ab initio* study of Pt/Cr

We first summarize in this part the main results obtained using Density Functional Theory (DFT) on an ideal Pt/Cr interface. This part of the work has been carried out by Carmine Autieri and Silvia Picozzi in CNR-SPIN L'Aquila as collaborators of the project. Two important aspects for the following discussion will be covered here: i) the effect of the spin-orbit coupling (SOC) in Pt on the magnetocrystalline anisotropy of Cr and ii) the penetration of magnetization in Pt interfaced with antiferromagnetic Cr.

For the first point, the magnetocrystalline anisotropy (MCA) has been calculated as a function of Cr lattice parameter. When SOC is taken into account, a clear dependence is found as shown in Figure 4.1. The MCA shows a strong sensitivity to strain effects, highlighted by the non-monotonic behavior and in agreement with what previously found for 3d ferromagnets interfaced with 5d materials. [94] For the lattice constant of
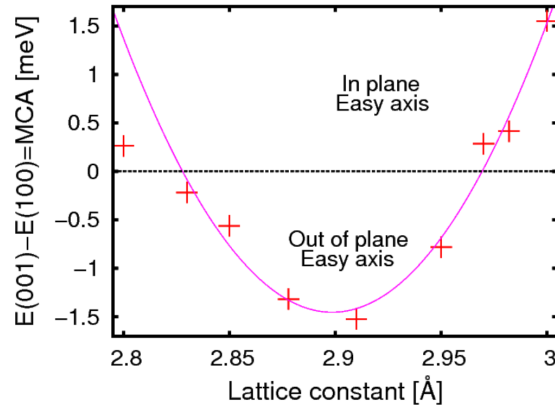
Figure 4.1: *Magnetocrystalline anisotropy (MCA) of the Pt/Cr heterostructure as function of lattice constant (red points) as predicted by density functional theory. Positive (negative) values of the MCA represent in plane (out of plane) easy axis. The purple line is a guide for the eyes.*
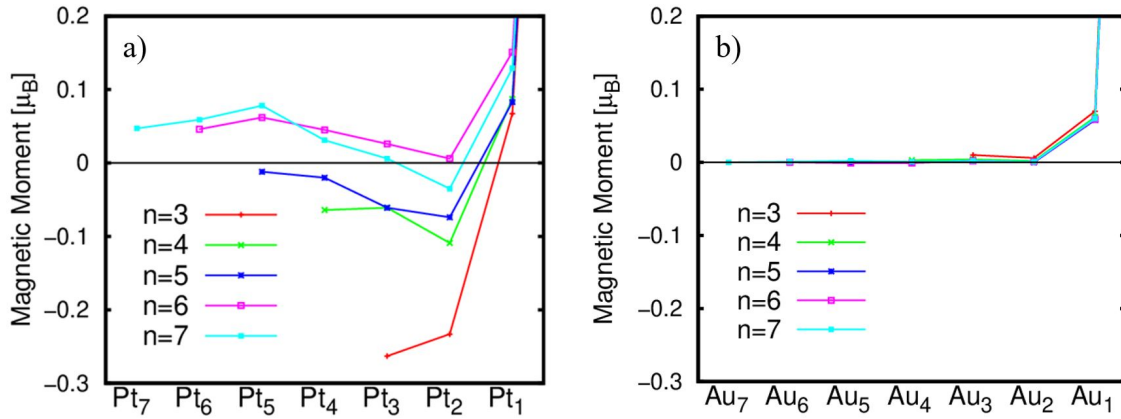

Figure 4.2: *a) Magnetic profile of the Pt(n)/Cr interface. The Pt1 is the Pt interface layer. The Pti is the i-th layer from the interface. b) the same for the Au(n)/Cr interface.*

bulk Cr (a=2.89 Å), also close to the one of our relaxed films grown on MgO, a large magnetocrystalline anisotropy with an out-of-plane easy-axis is expected. This implies that the natural tendency of Cr thin films to display an out-of-plane longitudinal spin-density wave (see section 2.1.1) should be even more energetically favorable in this case.

Regarding instead the proximity effect, the profile magnetization of the Pt(n)/Cr heterostructure has been calculated as function of the number (n) of Pt layers. and is shown in Figure 4.2a. The interface Pt always couples ferromagnetically with Cr, as for other ferromagnetic materials [95,96], and the magnetic moment remains different from zero even farther from the interface. From a theoretical point of view, the magnetic proximity demonstrates that the spin polarization, arising into the antiferromagnet, penetrates the Pt layers and, although the spatial profile is non-monotonous, the sum over the Pt layers leads to a non-vanishing total magnetization.

The specific role of Platinum in the observation of magnetic proximity effect (MPE) was introduced in section 2.2. Shortly, bulk Pt presents a van Hove peak close to the Fermi level and the interface hybridization can favor a Stoner ferromagnetic instability,

so that Pt undergoes a magnetic phase transition at interfaces. [97] This is made clear by comparing the results obtained for the Au(n)/Cr interface shown in Figure 4.2b. In this case, except for the tail of Cr magnetization on the first Au layer, the magnetic moment is always zero as gold is far to reach the Stoner instability.

The simultaneous presence of out-of-plane magnetocrystalline anisotropy at the interface and net magnetization in Pt sets Pt/Cr as a prototypical system for the test of anomalous Hall effect coupled with the antiferromagnetic order as will be assessed in the next sections.

4.2 Sample growth and device fabrication

For this work, Pt/Cr bilayers were grown on MgO (001) single crystals by Molecular Beam Epitaxy (MBE) (see section 3.1.1). Optimization of the Cr growth was already performed in the LASSE cluster described in section 3.1. [98] In LASSE we verified the single crystal growth, the chemical stability of the interfaces, and the impact of thickness and post-annealing on the residual strain in the chromium films. The sample growth consists of the following steps, all carried in ultrahigh vacuum (UHV) conditions.

1. Annealing of the MgO substrate at 873 K for 1 hour to clean and order the surface.

2. Deposition of Cr from an e-beam heated high-purity rod with a rate of 3 Å/min, as calibrated with a quartz microbalance, while keeping the substrate at 373 K.

3. Annealing at 873 K for 30 minutes to relax the chromium film and favor surface ordering.

4. Room temperature deposition of Pt from an e-beam heated high-purity rod with a rate of 0.8 Å/min.

5. Annealing at 673 K for 20 minutes.

Heterostructure were grown with Cr thickness ranging from 25 to 75 nm and with Pt capping from 0.4 to 3 nm. The structural characterization of Cr and Pt/Cr films was performed both *in-situ* exploiting the potential of X ray Photoelectrons Diffraction (XPD) and *ex-situ* by X-Ray Diffraction (XRD).

The XRD spectrum of a Pt(3)/Cr(75)//MgO is reported in Figure 4.3a. Apart from the diffraction signal coming from the substrate, the only visible peak corresponds to (002) planes of Cr, indicating a single crystal phase of the layer. The Pt film is too thin to produce signal in the XRD, but for utrathin films it is possible to exploit XPD which has chemical selectivity enabling the investigation of the surrounding of a given atomic species. The analysis of elastically scattered photoelectrons from Cr $2p_{3/2}$ and Pt 4f permits the crystallographic structure and order of Cr and Pt films, respectively, to be investigated. The results are shown in Figure 4.3b, where we report the XPD polar scans, collected along the [110] azimuth of MgO, of the Cr $2p_{3/2}$ peak on uncapped (black curve) and Pt-capped (blue curve) films, and of the Pt 4f peak of the capping layer on Cr (red curve). The well-defined diffraction peaks of all the scans demonstrates the good crystal quality of both Cr and Pt. Moreover, the quality of XRD on Cr top interface is maintained upon Pt deposition (the smaller signal-to-noise ratio in the blue
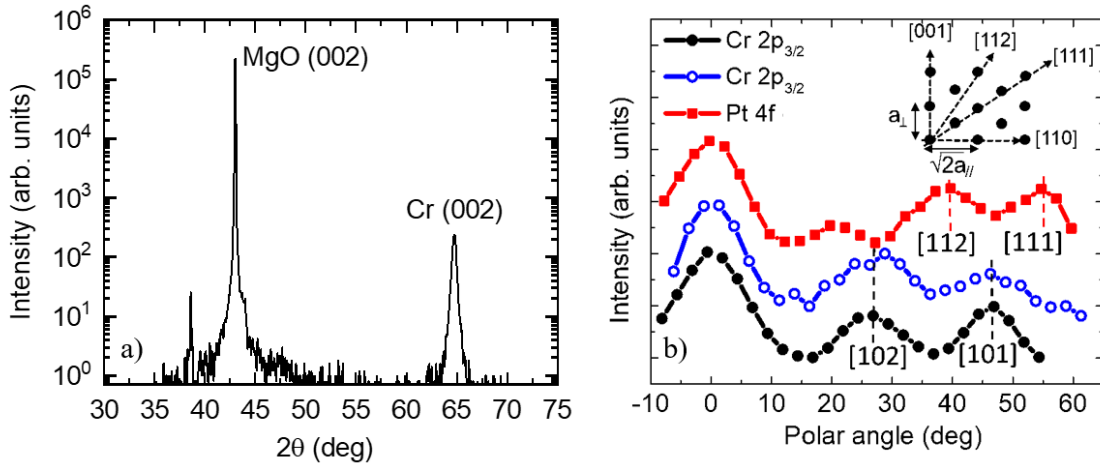
Figure 4.3: *a) X-Ray Diffraction spectrum obtained with Cu-Kα monochromatic source evidencing a single crystal phase of Cr. b) X-Ray photoelectron diffraction pattern of the Cr 2p3/2 (black curve: uncapped film, blue curve: Pt capped film) and Pt 4f (top, red line) along the MgO [110] azimuth on samples. Dashed lines indicate the main diffraction peaks, [102] and [101] for Cr (black line), [112] and [111] for Pt (red lines), respectively. In the inset is reported the atomic arrangement of a tetragonal lattice in the (110) plane, with the main diffraction directions indicated.*

curve with respect to the black curve comes from the attenuation of the Cr signal due to the Pt overlayer).

The two main peaks for Cr at 28° and 45° (the error bar is ±1°) can be ascribed to the diffraction, in the forward scattering regime, along the [102] and [101] crystallographic directions of a bcc Cr with [100] azimuth The diffraction pattern from Pt 4f photo-emitted electrons along the MgO [110] azimuth shows instead two peaks at about 39.0° and 54.8° polar angles, which correspond to diffractions along the Pt [112] and [111] directions, respectively (see the atomic arrangement of a tetragonal lattice in the (110) plane, shown in the inset, with the main diffraction directions indicated).

From these informations, it is possible to verify that a 45° rotation exists between the MgO and Cr unit cells, as expected for minimizing the lattice mismatch. In the same way Pt and Cr lattices are rotated by 45° so that MgO[110]∥Cr[100]∥Pt[110].

Devices were fabricated as Hall crosses out of the planar films following the process described in Section 3.2.2. In the next section we will discuss the main results obtained from electrical measurements.

4.3 Experimental results

For the electrical characterization, both longitudinal and transverse resistance measurements were performed as a function of temperature using the setup described in section 3.3.2, exploiting the compensation of geometrical and thermoelectric offsets.

The measurement protocol goes as follows: by cooling the sample below its Néel temperature in a magnetic field B = ±0.4 T perpendicular to the surface plane, produced by a permanent magnet in Halbach configuration, we set the magnetic state of Cr (field cooling). Subsequently, the state is read by measuring the anomalous Hall resistance while the temperature is raised with a constant rate of 2 K/min. A close-circuit He cryostat was used to this scope.
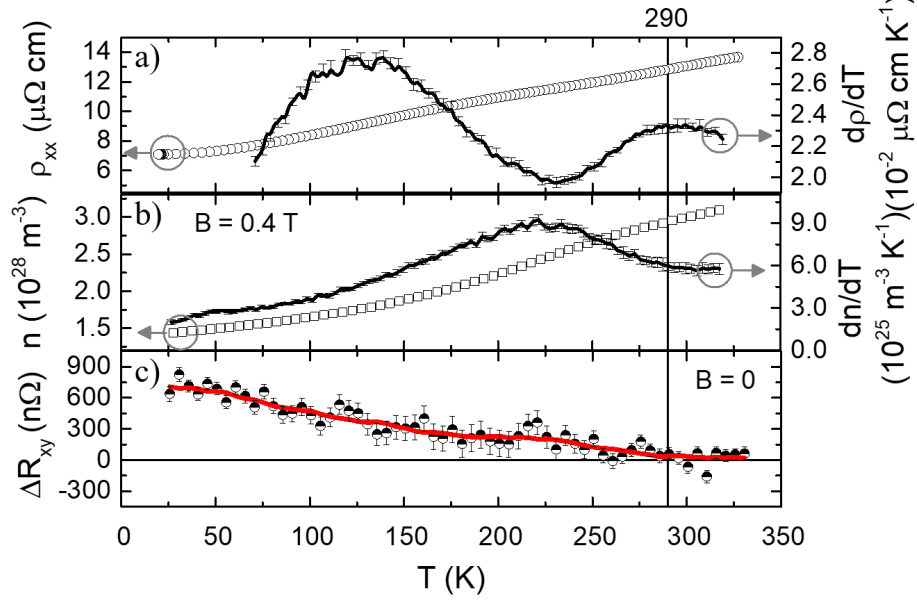
Figure 4.4: *Transport properties of a Pt(2)/Cr(50) Hall cross as a function of temperature. a) resistivity (empty dots) and first derivative (black line). b) number of carriers from ordinary Hall measurements (empty squares) and first derivative (black line). c) anomalous Hall resistance difference upon opposite field coolings. The red line is a guide for the eye.*

Figure 4.4 reports the transport properties of a Pt(2 nm)/Cr(50 nm) bilayer. The probing current used in this case is a $\pm$ 20 mA square wave. Figure 4.4a shows the longitudinal resistivity ρ_{xx} of the sample (empty dots) and its first derivative with respect to the temperature (black line) in the 20-330K temperature (T) range. Here, it is crucial to remind that the formation of the SDW in Cr determines the opening of a gap in the Fermi surface along the direction of the wave vector as discussed in section 2.1.1. This results in a reduction of the carrier density, that determines an upturn in the resistivity curve which may not be easily detected in the ρ_{xx} plot but it can be highlighted by calculating the derivative with respect to temperature. In fact, following reference [49], the Néel temperature T_N can be associated to the local maximum in $d\rho/dT$. From Figure 4.4a we find T_N = 290 $\pm$5 K which is to some extent inferior to bulk Cr T_N = 311 K but in line with other epitaxial thin films. [54] The same information can be extracted from the ordinary Hall resistivity ρ_{xy} since it is related to the carrier density n by the simple relation coming from the Drude model $\rho_{xy} = -B/ne$ (e is the electron charge). The temperature dependence of n (empty squares) and its first derivative (black line) with respect to T are shown in Figure 4.4b. For the reasons given above, the increase of dn/dT below 290 K is again consistent with the AFM phase transition of Cr, [54] in agreement with the value established from longitudinal resistivity measurements. Finally, 4.4c shows the difference between the anomalous Hall resistances (ΔR_{xy}) measured in states prepared by cooling the sample in opposite out-of-plane magnetic fields (B = $\pm$4 T). The small signal, in the order of hundreds of nano-ohms, can be reproducibly detected over multiple writings and is found to be dependent only on the field-cooling direction. ΔR_{xy} decreases with temperature, approaching zero in correspondence of the temperature T^* = 290 K, that happens to be

coincident with the previously determined T_N, considering the experimental error bar. Note that below T^*, the application of magnetic fields does no longer affects the transverse resistance at remanence, thus excluding the possible influence of ferromagnetic contaminations on the signal. On the contrary, the robustness against external fields can be explained by the negligible magnetic susceptibility of Cr in the AFM phase. This strict correspondence between Cr magnetic order, established from ordinary transport measurements, and presence of AHE clearly relates the origin of the latter to the antiferromagnet state. We emphasize that conventional magnetometry does not allow to observe this phase transition. No change in the magnetic signal is observed with Vibrating Sample Magnetometry (VSM) across the phase transition on an unpatterned Pt(3)/Cr(75) 5x5mm^2 sample. Considering the experimental error of 3 μemu this sets the upper limit to the average magnetic moment in Cr and Pt to 0.003 μ_B/atom and 0.07 μ_B/atom, respectively. The latter is still compatible with the predicted induced moment by DFT (see section 4.1) with a mediated value smaller than 0.05 μ_B/atom.

4.3.1 Origin of the Anomalous Hall Effect in Pt/Cr

Once the presence of AHE is assessed, it is important to verify whether this comes from bulk Cr or from the Pt interface, possibly related to the mechanisms described in Chapter 2. A first hint of the interfacial origin of AHE comes from the comparison of samples with different Cr and Pt thicknesses presented in Figure 4.5. ΔR_{xy} at 20 K is almost identical for samples with 25, 50 and 75 nm thick Cr films, and Pt thickness fixed to 3 nm, with an average value of 680 $\pm$120 nΩ. In the good-metal regime, the anomalous Hall resistance is proportional to the magnetization of the sample and independent of sample resistivity. [72] Being ΔR_{xy} not related to Cr thickness, a bulk contribution should be therefore excluded. Instead, when a thinner Pt layer (0.6 nm, corresponding to 4 monolayer) is considered, a smaller transverse resistance difference $\Delta R_{xy} = 275 \pm 30$ nΩ is found between states written with opposite field. We incidentally note that ΔR_{xy} in the thinnest Cr sample (25 nm) approaches zero already below 200 K. This is consistent with the reported increase of Cr transition temperature with thickness in epitaxial thin films. [49] A second confirmation of the interfacial origin comes from the insertion of a gold spacer between Pt and Cr. In this case, DFT calculations predict no proximity induced moment in Au/Cr (see Figure 4.2b), at variance with Pt/Cr systems. This is in excellent agreement with experimental results: as can be seen in Figure 4.5, the Pt(3)/Au(3)/Cr(50) sample does not show any detectable signal compared to any of the Pt/Cr samples. We emphasize that the same Cr(50) film was used for the comparison. Au was deposited on only half of the sample with the help of a mechanical shutter while Pt was grown on the whole sample. Hence, the different signal cannot be ascribed to Cr quality which is confirmed to be the same by resistivity and ordinary Hall measurements (not shown). Moreover, the AHE suppression with the interposition of the diamagnetic interlayer allows to exclude any significant contribution to the signal given by spin-Hall magnetoresistance (section 2.4.2), since any phenomena related to spin-current generation in Pt would result unaffected as the spacer thickness is much thinner than the spin diffusion length in gold ($\lambda > 30$ nm [99]).
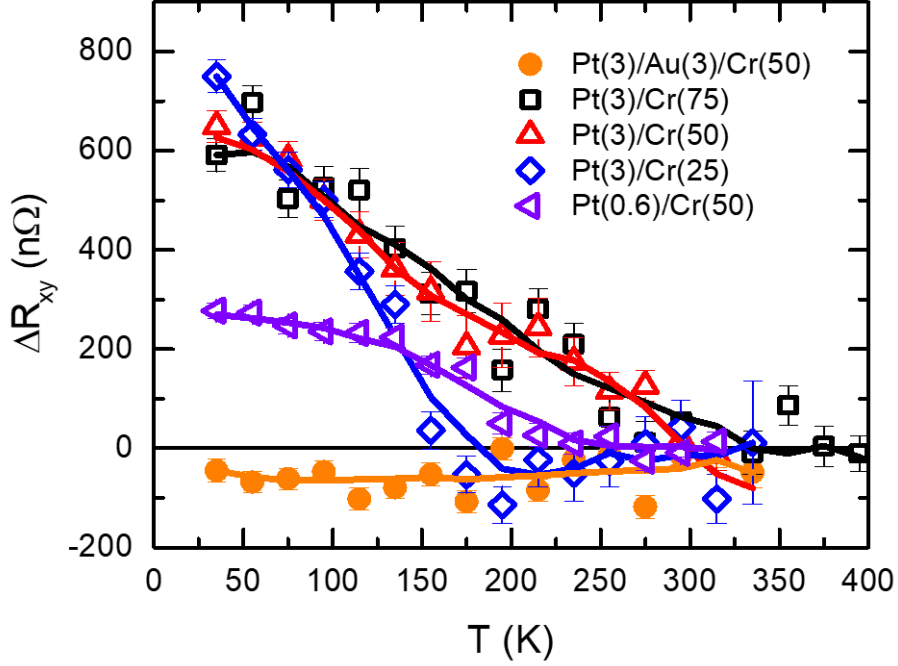
Figure 4.5: *Difference of the anomalous Hall resistance as a function of temperature in Pt/Cr and Au/Cr bilayers. Nominal thicknesses are expressed in nm. Error bars indicate the standard error on multiple samples. The lines are just a guide for the eye.*

4.3.2 Impact of field-cooling amplitude on AHE

In this last part, we address the impact of magnetic field amplitude in the field-cooling process of Pt/Cr. The previous results were obtained using a fixed magnetic field of 0.4 T provided by a permanent magnet, which was readily available in the cryogenic setup in Milan and could be easily removed for a field-free measurement of AHE. Indeed, larger magnetic fields can be achieved using superconducting coils, however, in this case the hysteresis of the superconducting magnet requires a careful compensation in order to obtain a true zero-field measurement. A second device on the same sample Pt(3)/Cr(50) of Figure 4.4 was measured using a cryogenic system available in JGU-Mainz with magnetic field up to 12 T. The raw measurements of AHE at remanence (a calibrated bias field of ± 70.0 Oe was used to compensate for the magnet hysteresis) for different field-cooling conditions are shown in Figure 4.6. A temperature-dependent offset from zero is clearly superimposed and we relate it to a non-perfect compensation of thermal voltages. These offsets, however, are fully reproducible across repeated measurements and subtraction can be used to isolate the true magnetic signal. When large fields are applied while cooling from room temperature ($B \geq 5$ T in this case) the signal difference at remanence is almost an order of magnitude larger, with ΔR_{xy}=5.6$\pm$0.5 $\mu\Omega$ (compared to ΔR_{xy}=672$\pm$100 nΩ with $\pm$0.4 T field cooling). The measurement after cooling at +7 T (black solid triangles in Figure 4.6) overlaps the one for state written at +5 T indicating that saturation can be reached even at magnetic fields lower than 5 T. Finally, when the system is cooled without any magnetic field (zero field-cooling, green dots in Figure 4.6), the resulting AHE sits in between the opposite states, consistently with a randomly-oriented multidomain state.
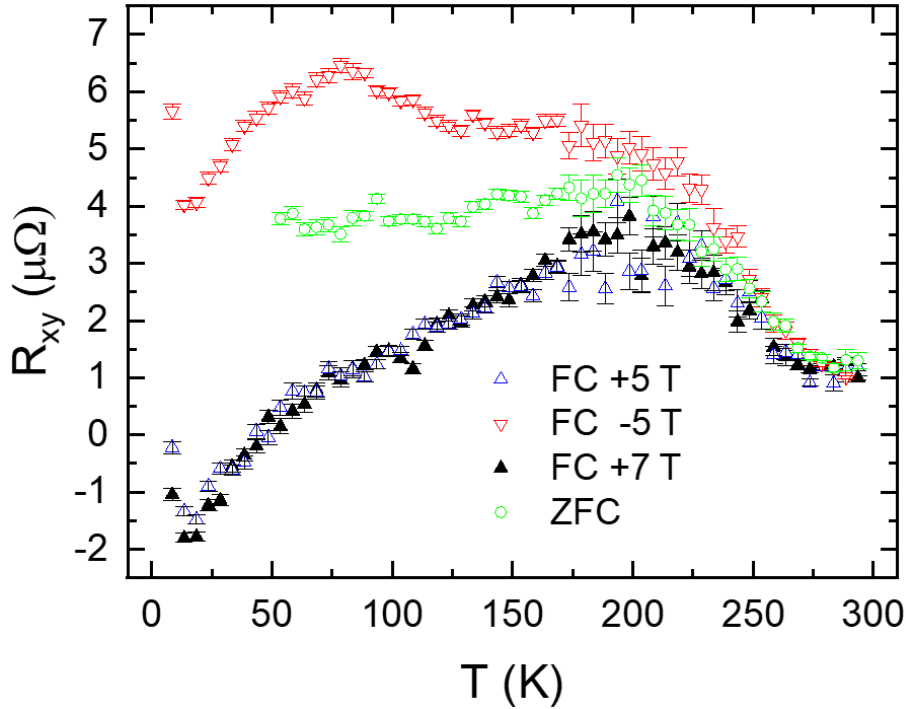
Figure 4.6: *Anomalous Hall resistance in Pt/Cr for different field cooling (FC) conditions. Field cooling with +5 (blue empty triangles) and +7 T (black solid triangles)results in the same remanent state, indicating that already at 5 T the interface magnetization is saturated. The signal for zero field-cooling (ZFC, green dots), consistently with a multidomain magnetic state, sits in between the ones for positive and negative field-cooling.*

4.4 Discussion

Anomalous Hall Effect (AHE) is typically associated to ferromagnetic metals as a consequence of broken time reversal symmetry and spin-orbit coupling and it is generally considered that ordinary antiferromagnets with collinear spin configuration should not exhibit AHE due to vanishing of the Berry phase. Chromium belongs to the family of collinear antiferromagnets, even though it displays a periodically modulated spin structure (the spin-density wave, section 2.1.1). Therefore, the appearance of AHE has to be related to the interface with Pt as we demonstrated measuring samples with different Cr and Pt thickness.

Just by measuring electrical transport properties some relevant informations on the antiferromagnet can be assessed. The Néel temperature is observed independently in three complementary measurements (ordinary Hall, resistivity and anomalous Hall after field cooing) and is found to decrease in thinner Cr films. The dependence of the anomalous Hall effect on field-cooling amplitude reveals that non-saturated multi-domain configurations can be present at the interface which do not respond anymore to magnetic field when Cr is in the antiferromagnetic phase. Finally, the comparison between Pt/Cr and Au/Cr devices highlights the crucial role of the interface in agreement with density functional theory predictions.

Therefore, Despite the fact that the signal is too small for any practical application (in the hundreds of nano-ohms), Pt/Cr represents a valuable tool for fundamental

study of emerging magnetic phenomena at interfaces. First of all, the elemental nature of the constituents allows to tackle the problem independently with an *ab initio* approach. As a second point, the peculiar features that Cr displays in the transport curves at the Néel temperature give another way to independently measure the antiferromagnetic transition, setting a clear correspondence between AHE and antiferromagnetism in chromium. In the end, while the results reported highlight the specific role of the interface with Pt, we could expect similar mechanisms with other NM metals like Pd, [100] Ir, W, [63] or V [101] reported to have proximity magnetization in contact with ferromagnets, thus making Cr a simple testbed to study these interface effects also in antiferromagnets. At the same time, we can anticipate AHE coming from interfaces to be generally exploitable in a large variety of antiferromagnetic systems, either metallic or insulating, making Hall measurements a powerful probe of antiferromagnetism both for fundamental studies and in view of applications.

Synthesis and antiferromagnetism of tetragonal Cr(III) oxide

This chapter will cover the synthesis of tetragonal-Cr_2O_3 (t-Cr_2O_3) and the demonstration of its antiferromagnetic character. In section 5.1, we show that a tetragonal phase of chromium (III) oxide can be stabilized on $BaTiO_3$. The resulting structure consists of a defective rocksalt cell where one out of three Cr atoms is missing. This compound has a different structure with respect to the stable phase of Cr_2O_3 in the bulk, which, in the form of α-Cr_2O_3, has a corundum (rhomboedral) structure and is a layered antiferromagnet.

Subsequently, in section 5.2.1, the antiferromagnetic ordering, expected by *ab initio* calculations, is demonstrated by both magnetoresistance and anomalous Hall measurements in Pt/t-Cr_2O_3 with a critical temperature T_N = 40 K.

5.1 Interdiffusion-driven synthesis of tetragonal Cr(III) oxide on $BaTiO_3$

While the growth of epitaxial t-Cr_2O_3has been reported by Cr deposition in a ozone atmosphere on MgO, [102] we exploited instead a solid state reaction between metallic Cr and the perovskite oxide $BaTiO_3$ (BTO). We demonstrated, in fact, that a thermally activated oxygen migration from the underlying layer causes the complete oxidation of ultrathin Cr layers on BTO leading to this uncommon tetragonal cell. [7] In this section we first discuss the stability of Cr/BTO interface and the synthesis of epitaxial t-Cr_2O_3 driven by interdiffusion of atomic species across the interface. We then present the expected electronic and magnetic properties of this compound from *ab initio* calculations. To grow Cr/BTO//STO(001) multilayers, a combined deposition has been performed in the same vacuum cycle in the cluster tool LASSE, using Pulsed Laser Deposition (section 3.1.2) for BTO and Molecular Beam Epitaxy (section 3.1.1) for Cr.
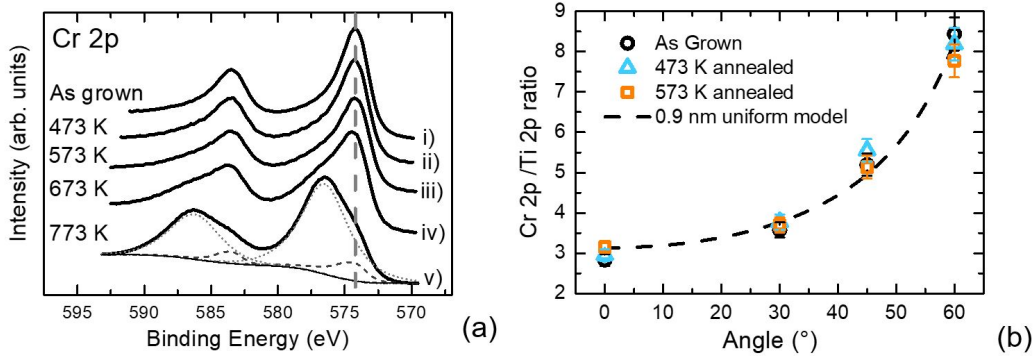
Figure 5.1: *a) Cr 2p photoemission spectra following annealing at increasing temperatures. b) Cr/Ti photoemission intensity ratio as a function of angle and annealing temperature. The accordance to a uniform layer model (dashed line) and the temperature independence rules out any significant interdiffusion. Reprinted with permission from [7]*
.

Post-annealing treatments, photoemission experiments and electron diffractions were conducted *in situ* as well. The growth parameters for BTO are summarized in Table 5.1.

Laser wavelength	266 nm
Substrate temperature	873 K
Oxygen pressure	0.053 mbar
Oxygen flux	0.2 sccm
Pulse energy	9 mJ
Repetition rate	2 Hz
Deposition rate	1.2 nm/min

Table 5.1: *Growth conditions for $BaTiO_3$ on $SrTiO_3$.*

Metallic Cr was deposited at room temperature with a calibrated rate of 2Å/min. For electrical transport experiments, 2 nm of Pt were deposited on top of t-$Cr_2O_3$by MBE with a rate of 0.8Å/min.

5.1.1 Chemical stability of the Cr/BaTiO$_3$ interface

Interdiffusion of chemical species across interfaces is typically overlooked but is an important issue especially in metal/oxide heterojunctions. Here we consider the specific case of the Cr/BaTiO$_3$ interface. Chromium has an high reactivity and forms different thermodynamically stable oxides such as Cr_2O_3, CrO_2 and CrO_3. When in contact with perovskite $SrTiO_3$, oxygen diffusion from the substrate to MBE grown Cr thin film has been reported following in-vacuum annealing over 900 K. [103] It was also shown that this solid-state reaction strongly depends on the electronic structure of the oxide itself [104] and the migration from BTO may be activated at a different temperature. To test this, we performed X-ray Photoemission Spectroscopy (XPS) on a Cr(1 nm)/BTO(30 nm)//STO sample following incremental post-annealing processes. The spectra acquired for the Cr 2p peak are reported in Figure 5.1a. We can observe that in the as grown Cr film (i) the asymmetric line shape and the Cr 2p$_{3/2}$ peak posi-
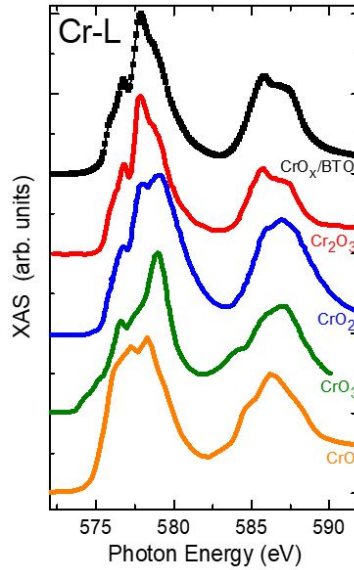
Figure 5.2: *Comparison of the X-ray Absorption spectrum at the Cr L edge of Chromium oxide on BTO (black curve) with reference data for α-Cr$_2$O$_3$, [106] CrO$_2$, [107] CrO$_3$ [108] and CrO. [109] Reprinted with permission from [7].*

tion at 574.35 ± 0.15 eV are consistent with a fully metallic Cr layer [105]. The same spectrum is preserved after 20 minutes long annealing at 473 and 573 K (ii-iii). However, upon the annealing at 673 K (iv), a shoulder at higher binding energies appears, finally dominating the spectrum when the sample is annealed at 773 K (v) with a peak shifted to 576.7 ± 0.15 eV. This chemical shift is a typical signature of 3^+ oxidation state of Cr. [105]. Concerning the possible interdiffusion of metallic species across the boundary, Figure 5.1b reports the effect of annealing on the angular dependence of the Cr 2p/Ti 2p intensity ratio. No significant effect is seen for annealing up to 573 K and the experimental data are well fitted by the expected curve for a uniform coverage of 0.9 nm thick Cr on BTO (dashed line). This, on one side, demonstrates a good planar growth of metallic Cr on BTO and, on the other side, exclude any sensible interdiffusion. For annealing temperatures larger than 573 K the Cr/Ti ratio is dominated by photoelectron diffraction as will be discussed in Section 5.1.2 and is not reported.

To unambiguously verify the oxidation state in the film annealed at 773 K X-ray Absorption Spectroscopy (XAS) at the Cr L edge has been performed on oxidized Cr/BTO sample at the APE beamline of the Elettra synchrotron in Trieste. In this case a 2 nm thick film of Cr has been used and complete oxidation was achieved performing a single annealing at 773 K. The results are shown in Figure 5.2 together with reference spectra of bulk Cr$_2$O$_3$and other possible chromium oxides. The striking match between oxidized Cr on BTO and α-Cr$_2$O$_3$ XAS spectra gives further confirmation of the expected Cr 3^+ oxidation state. This also indicates a very similar electronic structure despite the structural difference that will be discussed in the next section.

5.1.2 Structural phase of Chromium oxide on BTO

Because of the interfacial reaction that we use to synthesize Cr$_2$O$_3$, the thickness of this material is limited to few nanometers. This makes impossible to use ordinary structural
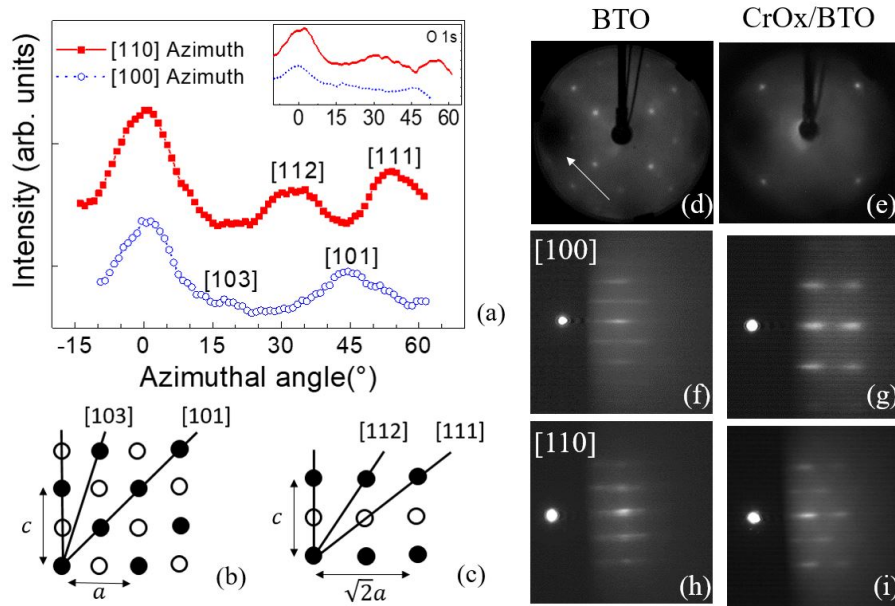
Figure 5.3: *Electron and Photoelectron diffraction of epitaxial chromium oxide on BTO. a) XPD angular scan of Cr 2p peak along [100] and [110] azimuth. In the inset: the same for O 1s. b),c) interpretation schemes for the peaks observed in XPD for the [100] and [110] azimuth respectively. d),e) LEED pattern of BTO and t-Cr_2O_3. The white line is parallel to the [100] direction of BTO. f),g) RHEED pattern taken on the [100] azimuth for BTO and t-Cr_2O_3. h),i) RHEED pattern taken on [110] azimuth for BTO and t-Cr_2O_3. Reprinted with permission from [7].*

characterization techniques such as X-Ray Diffraction which would have a signal too small from such an ultrathin layer. Nevertheless, it is possible to use surface sensitive techniques such as Photoelectron Diffraction (XPD) and electron diffractions (LEED, RHEED) available in-situ in the cluster LASSE.

Figure 5.3a reports the Cr 2p peak intensity as a function of photoelectron take-off angle. Three clear XPD peaks are visible either when the sample is rotated along the [100] or [110] directions. Those peak can be easily interpreted as the ones of a slightly distorted face-centered cubic (FCC) lattice (see for instance black points in Figure 5.3b,c). XPD of the O 1s peak is reported in the inset of 5.3a. The same diffraction angles are found also in this case pointing out an analogous coordination of the atoms. This is consistent with a rocksalt structure in which, necessarily, one out of three atoms in the Cr site is missing because of the stoichiometry constraint. This phase is different from the bulk Cr_2O_3 , which has a corundum structure with a rhomboedral unit cell, and it is possible to stabilize in thin films only through the epitaxial strain from the substrate. We note that a similar phase has been previously obtained on MgO substrates through evaporation of Chromium in an ozone atmosphere, [102] as a confirmation of the possibility to grow this structure epitaxially on different substrates. Finally, electron diffractions corroborate the hypothesis of a tetragonally distorted rocksalt structure. The Low Energy Electron Diffraction (LEED) pattern of t-Cr_2O_3 (Figure 5.3e) shares the same fourfold symmetry of BTO (Figure 5.3d). Reflection High Energy Electron Diffraction (RHEED) of t-Cr_2O_3 (Figure 5.3g,i) is again pointing to a FCC lattice. A morphological information can be finally obtained as the modulation of the streaks in t-Cr_2O_3 RHEED pattern indicates some three-dimensional growth of the

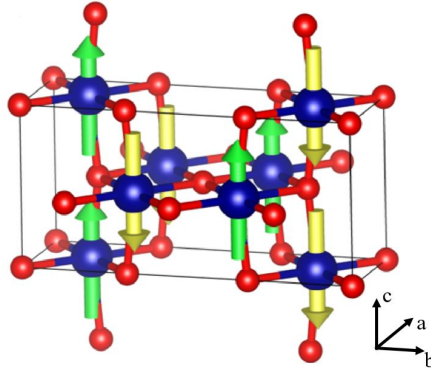**Figure 5.4:** *Structure and magnetic configuration of t-Cr$_2$O$_3$ as predicted by density functional theory.*

layer probably related to roughening during the oxidation process.

5.1.3 Prediction of the electronic properties of t-Cr$_2$O$_3$ from Density Functional Theory

Ab-initio calculations have been performed by our collaborators C. Autieri and S. Picozzi of CNR-SPIN L'Aquila on the t-Cr$_2$O$_3$ structure inferred from diffraction measurement. The main results obtained from Density Functional Theory (DFT) on the electronic structure are reported in reference [7], indicating a substantial analogy to the case of bulk α-Cr$_2$O$_3$. This similarity holds true despite the structural difference because of the same octahedral coordination of oxygens in the two cells, leading to absolutely comparable density of states and bandgap of 3.2 eV. Here we focus instead on the magnetic properties of t-Cr$_2$O$_3$ that will be experimentally assessed in the following of the chapter.

First of all, from a purely geometrical argument, a G-type antiferromagnetic ground state as in Figure 5.4 would be expected in t-Cr$_2$O$_3$ according to Goodenough-Kanamuri rules for superexchange [110]. DFT indicates a magnetic moment of 2.9 μ_B per Cr atom and axis dependent exchange couplings (according to the reference frame in Figure 5.4) J$_c$=6.9 meV, J$_b$=49.5 meV (antiferromagnetic) and J$_a$=-3.0 meV (ferromagnetic). Using these values in mean field theory the expected Néel temperature is 643 K. However, mean field theory fails in presence of defects and low dimensionality, meaning that the transition temperature could be much lower than this value. In the next section we demonstrate experimentally the antiferromagnetism of t-Cr$_2$O$_3$ through electrical measurement and we verify the transition temperature to be $\approx$ 40 K.

5.2 Antiferromagnetism of t-Cr$_2$O$_3$/BaTiO$_3$

In this part of the chapter we present experimental results supporting the expected antiferromagnetic character of epitaxial Cr$_2$O$_3$ on BaTiO$_3$ covered in section 5.1.3. Following the methodical approach discussed in section 3.3.1, we discuss the magneto-transport properties of Pt on t-Cr$_2$O$_3$ as a function of temperature. We observe clear indications from interface driven effects such as Spin Hall Magnetoresistance (section 2.4.2) and Magnetic Proximity Effect (section 2.2) pointing out an antiferromagnetic Phase transition around 40 K.
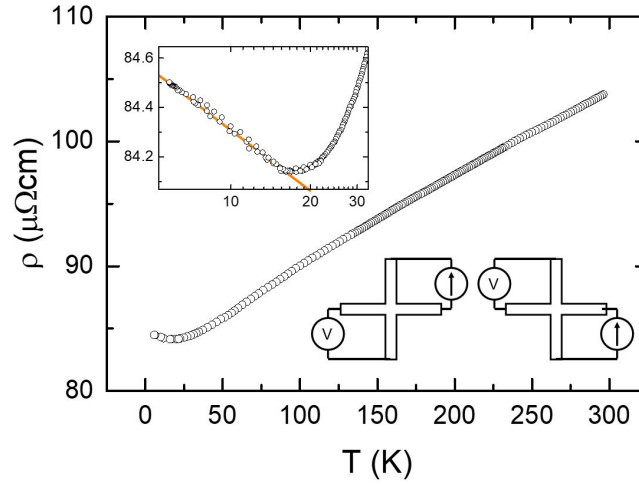
Figure 5.5: *Resistivity of Pt on t-Cr₂O₃ as a function of temperature. Bottom inset: sketch of the device and Van der Pauw measurement configuration. Top inset: zoom in the low temperature region highlighting the logarithmic dependence of the resistance anomaly.*

5.2.1 Electrical properties

We recall that the first system in which interface effects with Pt were used to detect the state of an insulating antiferromagnet was actually a corundum α-Cr_2O_3 thin films by Kosub *et al.* [43, 72]. While we could expect similar interface effects to be present, we still need to verify that they are significant also in the tetragonal phase of Cr_2O_3. In fact, while α-Cr_2O_3 presents a layered antiferromagnet structure, t-Cr_2O_3 is expected to exhibit a G-type antiferromagnetism (see section 5.1.3). As such, the effect of magnetic order on the transport properties of Pt could be different in this case.

For the electrical characterization, 50 μm wide Hall crosses were defined through optical lithography and ion beam etching on a Pt (2)/t-Cr_2O_3(2)/BaTiO₃ (30)//SrTiO₃ heterostructure (thicknesses in nm), as described in section 3.2.2. The integrated magneto-transport setup (section 3.3.2) was employed with a Cryogenics™ closed cycle liquid helium superconducting cryomagnetic system, able to reach a minimum temperature of 1.4 K and a maximum magnetic field of 7.5 T, located at L-NESS laboratories in Como (Italy). A current square wave with amplitude ±100 μA was used for all the measurements.

Figure 5.5 presents the resistivity ρ of Pt (the only conductive layer in the heterostructure) as a function of temperature acquired during a field cooling from 300 to 6 K at B = +7.5 T. As discussed in section 3.3.1, the Van der Pauw geometry sketched in the bottom inset of the figure can be used to obtain a reliable value of resistivity provided that the material is uniform and the thickness well known. As typically observed in ultrathin Pt films the resistivity is sensibly larger than the bulk value ρ = 11.1 $\mu\Omega cm$. The typical temperature dependence for good metals is observed with a positive coefficient of resistance $d\rho/dT$ on most of the range inspected. Nevertheless, a low-temperature anomaly is found (see top inset in Figure 5.5) and the resistivity starts to increase again with a logarithmic trend below 20 K. Several mechanisms can account for this behavior: electron-electron interactions, quantum interference of the electron waves (Weak localization) [111] and scattering with magnetic impurities (Kondo ef-
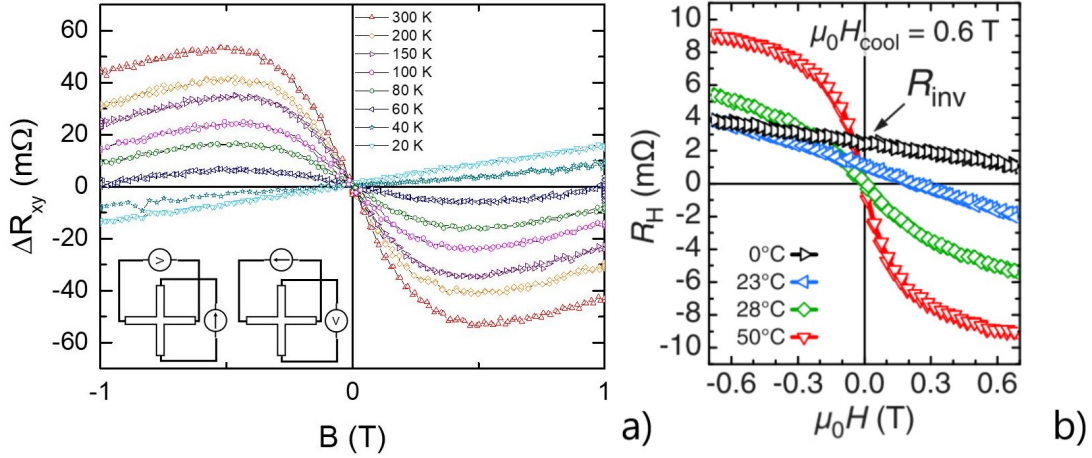
Figure 5.6: *a) Hall effect in Pt on t-Cr$_2$O$_3$ at different temperatures. An anomalous component is evident above 40 K. Inset: Measurement configuration for geometrical offset subtraction. b) Hall effect in Pt on α-Cr$_2$O$_3$, reprinted with permission from [72]*

fect) [112]

The latter could be already a signature of Magnetic Proximity Effect (MPE), as Kondo has been recently shown to arise together with ferromagnetism when a large electric field is applied in Pt thin films by means of ionic gating [59]. However, as all three effects determine the same functional dependence of resistance, it is difficult to disentangle the various contributions in the present case.

Results of Hall measurements at several temperatures are reported in Figure 5.6a. Two separate Hall measurements with the electrode configurations sketched in the inset of 5.6a were subtracted to compensate for geometrical offsets as described in section 3.3.1. While at low temperature only the linear ordinary hall effect (OHE) is observed, above 40 K an anomalous component arises as well. This same dependence has been demonstrated in reference [72] on Cr$_2$O$_3$ above the Néel temperature $T_N = 301$ K and ascribed to magnetic proximity in Pt. Their result are reported for comparison in Figure 5.6b. Remarkably, the sign of OHE is reversed in our measurements with respect to those of ref. [72]. However, an inversion of the Hall coefficient has already been reported depending on Pt thickness t [59, 113] and, consistently with our results, a positive slope is observed for $t < 3$ nm. Even though the coverage is nominally identical, a small deviation from the expected value can easily justify this difference. Nevertheless, the comparable behavior of the anomalous part, despite the different critical temperature which is found at about 40 K for t-Cr$_2$O$_3$, gives a first indication of the expected antiferromagnetic phase transition.

Following the same approach used for Pt/Cr (see chapter 4), we verified the possibility to write a state in the AFM phase via field cooling and reading it at remanence through Hall measurements. To achieve true remanence conditions (B = 0) while using a superconducting coil, a particular care is needed to counteract the hysteresis of the magnet itself. In fact, the trapped current loops may still produce a stray field of several tens of Oersted in the sample space. We compensated this by applying a small bias to keep the magnetic field within ±1 Oe.

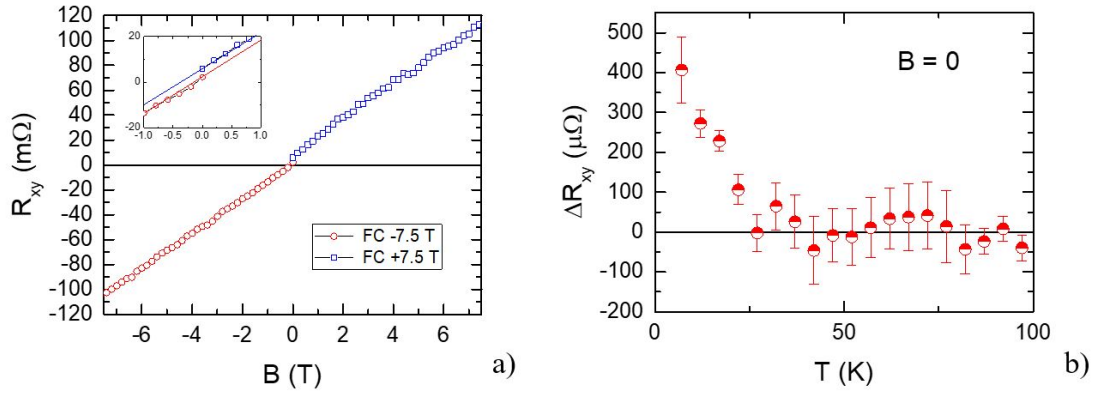Figure 5.7a shows the Hall signal measured at 6 K while sweeping the field to zero

Figure 5.7: *a) Hall Resistance at 6 K following two opposite field cooling processes B = +7.5 T (blue squares) and B = -7.5 T (red dots). Inset: zoom highlighting the gap between the two curves coming from the remanent magnetization set via field cooling. b) Anomalous resistance difference at B = 0 between states set with an upward and a downward field cooling.*

after a field cooling at +7.5 T (blue dots) and -7.5 T (red squares). As discussed before, no anomalous component is highlighted at low temperature and the field dependence is linear. An offset from zero, originating from uncompensated out-of-plane magnetization, is present and can be consistently determined with a field cooling process in two different states. The gap between the two curves is highlighted in the inset of Figure 5.7 which shows a zoom at low field. The temperature evolution of this difference is shown in Figure 5.7b. Despite the rather noisy signal it is evident that this residual Hall signal can be distinguished only below 35 K consistently with our previously determined transition temperature. While this is the same mechanism that has been reported for corundum Cr_2O_3, [72] it is worth to notice that in that case the interface was with a layered antiferromagnet i. e. with a ferromagnetically ordered surface. In our case we expect a G-type ordering (with reference to section 5.1.3) and the signal should be related only to uncompensated moments. Finally, we observe that this signal can not be ascribed to some ferromagnetic contamination because it has been found completely insensitive to magnetic field up to 2 T applied at 6 K, corroborating its relationship to antiferromagnetic t-Cr_2O_3.

5.2.2 Magnetoresistance

In this section we present in the magnetoresistive properties of the Pt/t-Cr_2O_3 system. We start discussing the temperature dependence of low-field magnetoresistance (MR) reported in Figure 5.8a-c for different relative directions of magnetic field **B** and current **j**. We first notice that, in all the cases, the MR ratio decreases monotonously with temperature, eventually displaying a flat response for T ≤ 40 K. Once again this is consistent with recent reports on α-Cr_2O_3 [84] where the low-field MR vanishes at the Néel temperature. We then highlight that while a positive MR is observed for **B**∥**j** (Figure 5.8a) and **B**⊥**j** with **B** normal to the sample surface (Figure 5.8c), a negative MR is found when **B**⊥**j** with **B** in plane (Figure 5.8b). This behavior can be understood within the framework of Spin Hall Magnetoresistance (SMR, see section 2.4.2): above T_N, the magnetic field orients the spins of paramagnetic t-Cr_2O_3, causing a decrease
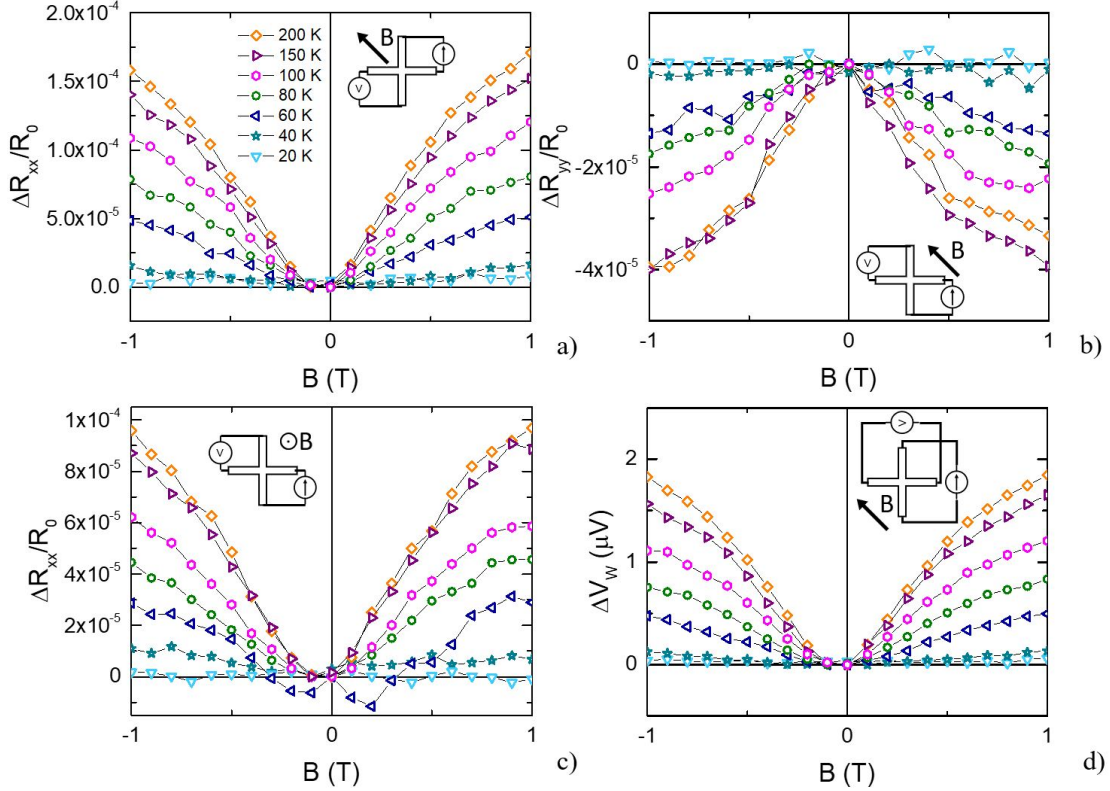
Figure 5.8: *Low-field magnetoresistance in Pt/t-Cr$_2$O$_3$. a) Field parallel to current b) field perpendicular to current in plane c) field out of plane d) Wheatstone bridge output voltage. In the insets: sketch of measurement configuration and field direction*

of resistance proportional to m_y^2, where y indicates the direction in plane perpendicular to the current. Below T$_N$, spins of the antiferromagnet are insensitive to the external field and the resistance remains constant. Finally, Figure 5.8d shows how the SMR signal can be greatly improved in term of signal-to-noise ratio by exploiting the intrinsic Wheatstone-bridge capability of Hall crosses in the planar Hall geometry (section 3.3.1) providing at the same time robustness to the measurement against thermal drifts.

With the idea of revealing the Néel vector orientation and the system anisotropy, magnetoresistance and its angular dependence have been characterized with the high field setup in JGU (Mainz). Two sets of data obtained above (T = 200 K) and below (T = 20 K) T$_N$ are shown in figure 5.9. The MR for B oriented along the three principal axes x, y, z, with x parallel to the current flow, y perpendicular to it in the plane, and z out of the plane, are shown in 5.9a,e. As introduced in the previous paragraph, the MR at 200 K can be largely explained by SMR in a paramagnetic system. The angular scans show the expected $\sin^2$ dependence of MR. We recall from section 2.4.2 that the scan in the xy plane (angle α, Figure 5.9f) includes both contributions of anisotropic magnetoresistance (AMR) and SMR, the scan in the yz plane (angle β, Figure 5.9g) the contribution of SMR only, and the scan in the xz plane (angle γ, Figure 5.9h) isolates the sole AMR. Observation of AMR in Pt should not be surprising as a magnetized state can be easily induced by proximity effects [72,114]. It is noticeable that the field dependence is rather different in the two cases, SMR (Figure 5.9g) increases monotonously
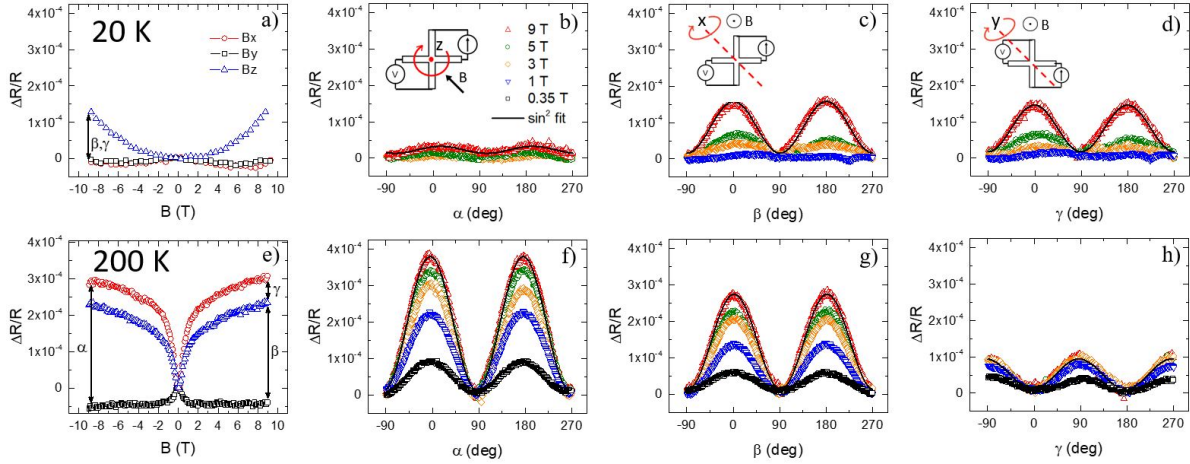
55

Figure 5.9: *Large-field magnetoresistance and angular dependence in Pt/t-Cr$_2$O$_3$. a) MR at 20 K. b-d) angular scans for different field strengths along α, β, γ directions as defined in section ?? at 20 K. e-h) same as a-d) for T = 200 K*

at least up to 9 T whereas the AMR (Figure 5.9h) saturates already at B $\approx$ 1 T. Below T$_N$ we still observe signals along both β (Figure 5.9c) and γ (Figure 5.9d). Notably the sign of MR in the scan along γ is reversed with respect to the same measurement at 200 K and the field dependence now matches perfectly in amplitude the one of the scan along β. As a result of that, the signal along α (Figure 5.9b) is negligible. At the present point we cannot tell if this striking similarity between the two out-of-plane scans is just accidental or has a physical meaning related to the antiferromagnetic transition as also discussed below. Here we just note that the MR on β keeps the symmetry of a positive SMR (as in the paramagnetic state above T$_N$). In a spin-flop antiferromagnet the spins would be perpendicular to the applied field, therefore SMR along β whould be either zero or negative (90° out of phase). So, if SMR is still the main contribution to MR, this would exclude a spin-flop even at 9 T in t-Cr$_2$O$_3$. Instead, the positive SMR signal can be originated by the canting of AFM moments.

5.3 Discussion

In this chapter we have reported on the synthesis of the uncommon tetragonal phase of Cr$_2$O$_3$ by thermally-activated oxygen migration from BaTiO$_3$ to a metallic Cr overlayer. By means of *in-situ* XPS we have shown that the onset of this solid state reaction is at $\approx$ 673 K and full oxidation up to few nanometers is reached with an annealing at 773 K. Multiple spectroscopic signatures point out a 3$^+$ oxidation state as in Cr$_2$O$_3$, while electron and photoelectron diffraction reveal a defective rocksalt cell structure in which one out of three Cr atom is missing. As this phase is not stable in the bulk (Cr$_2$O$_3$ has a rhomboedral unit cell), we can make two general considerations on interfaces. The first one is that the interface is not a rigid boundary and interdiffusion of chemical species can possibly create some radically different compounds from the one expected, as such, a great care should be given to proper chemical characterization of interfaces especially if thermal processes are involved. The second aspect highlights the potential role of epitaxy in stabilizing new phases otherwise impossible to study in the bulk (at
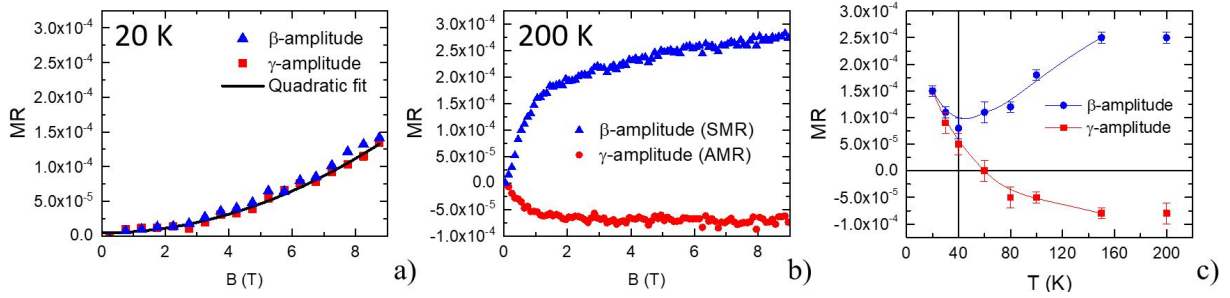
Figure 5.10: *Field and temperature dependence of magnetoresistance in Pt/t-Cr_2O_3a) amplitude of MR along β (blue triangles) and γ (red squares) at 20 K as a function of B as extracted form data in 5.9a. The black line is a quadratic fit of the experimental data b) The same of panel a at 200 K, the data as a function of B are extracted from 5.9e. In this case the signal on β can be identified with SMR, while the signal on γ is the part related to AMR. c) Evolution of β (blue triangles) and γ (red squares) amplitude at B = 9 T for different temperatures.*

least in standard conditions of temperature and pressure).

The magnetic properties of t-Cr_2O_3 were investigated both theoretically and experimentally. Despite theory would predict a whopping Néel temperature of 643 K in this compound, both longitudinal and transverse resistivity measurements point out instead an AFM phase transition below 40 K. This discrepancy should not be surprising as disorder in Cr vacancies and the reduced dimensionality (a 2 nm thick film has been studied due to the interfacial solid-state reaction employed for material synthesis) can largely impact on the effective exchange coupling. Finally we address some open questions regarding magnetoresistance in the AFM phase. With reference to Figure 5.9a-d, the explanation within the framework of combined SMR and AMR may be too simplistic. Indeed, the coincidence of β and γ amplitude in the scans at T = 20 K can be related to a fortuitous matching of the AMR and SMR coefficients, thus canceling each other out in the α scan. Nevertheless, a couple of elements makes this coincidence unlikely. First, if we take the amplitude of β and γ as a function of magnetic field from panel a and e in Figure5.9 we observe a radical difference. At 20 K an identical parabolic trend for both β and γ is found (see Figure 5.10a). At T = 200 K, instead, β and γ present different functional dependence with field and while AMR saturates already at 1 T, SMR keeps increasing (see Figure 5.10b). Therefore, if the results at 20 K were just a mere coincidence, the AMR coefficient should have changed not only its sign and amplitude to match the one of SMR, but also its functional dependence with magnetic field.

As a second point, by looking at the MR ratio as a function of temperature presented in Figure 5.10c, we find another anomaly. While the amplitude of γ evolves monotonously inverting its sign at about 60 K, the amplitude of β has an oscillation in correspondence of the Néel temperature. This raises the question that the mechanism dominating magnetoresistance in the AFM phase may be no longer ascribable to SMR. A possible alternative interpretation is that below T_N spins do not respond at all because of the low susceptibility, suppressing both AMR and SMR. The magnetoresistice signal in this case may come just from the Ordinary MR (OMR) of Pt which originates from the Lorentz force and, in the ultrathin film limit, responds to the out-of-plane component only [115]. OMR follows the relationship

$$\frac{\Delta R}{R} = aH^2 \tag{5.1}$$

well describing the parabolic trend observed a T = 20 K with a coefficient $a = 1.6 \cdot 10^{-6}$ T^{-2} (for comparison the value for bulk Pt is $5.4 \cdot 10^{-6}$ T^{-2}). Still remains unclear how this quadratic component which should be weakly dependent on temperature does not appear in the paramagnetic phase of t-Cr$_2$O$_3$ as well. The question remains open for further investigation, fostering the need of a more comprehensive model to explain the peculiar transport properties of Pt on AFM insulators.

Growth and magnetic characterization of $TmFeO_3$ thin films

This chapter deals with the preliminary results on antiferromagnetism in single-crystal $TmFeO_3$ thin films. The project realized in Johannes Gutenberg Universität in Mainz under the supervision of Prof. Gerhard Jakob and Prof. Mathias Kläui. The first part of the work consisted in the growth optimization of epitaxial thin films of rare-earth orthoferrite $TmFeO_3$ as described in section 6.1. The second part regarded the investigation of the magnetic properties of these films, with insulating antiferromagnet character as expected, exploiting once again interface effects with a Pt capping layer. The outcome of these preliminary results and the perspectives of this work are discussed in section 6.2.

6.1 Growth of epitaxial $TmFeO_3$ thin films on $SrTiO_3$

$TmFeO_3$ (TFO) belongs to the class of rare-earth orthoferrite. Compounds in this family crystallize in an orthorhombically-distorted perovskite structure (a=5.2491 Å, b=5.5716 Å,c=7.5824 Å) with iron moments antiferromagnetically coupled as in Figure 6.1. TFO has a Néel temperature of about 630 K [116] and is distinguished by a strong thermal dependence of the magnetocrystalline anisotropy, with a spin reorientation transition (SRT), known since the sixties, in which the antiferromagnetic easy-axis gradually rotates by 90°between 82.5 and 92.8 K. [117–119] Below the SRT Fe spin are oriented along the c-axis (Figure 6.1a), whereas they align along the a-axis when above the SRT (Figure 6.1b). The strong spin-orbit coupling of Tm ions forces an anisotropic exchange interaction, also known as Dzyaloshinskii-Moriya, between neighboring Fe atoms. The effect of this term is a small canting of the spins which result in a small ferromagnetic component perpendicular to the AFM spin-axis. This *weak ferromag-*
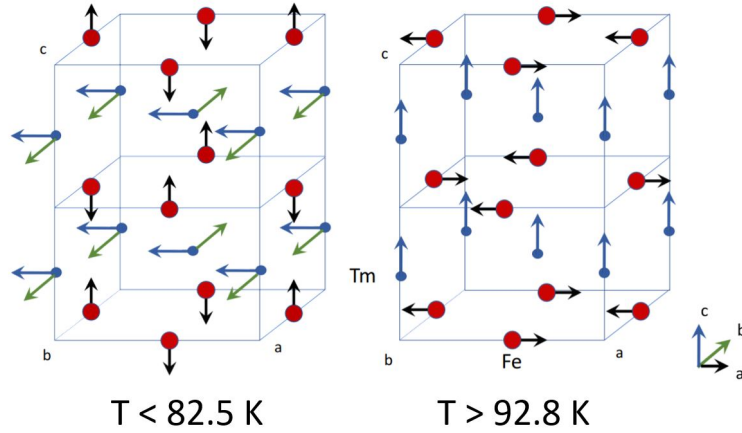
T < 82.5 K   T > 92.8 K

Figure 6.1: *TmFeO$_3$ crystal structure and spin configuration a) below the spin reorientation transition temperature and b) above it. Adapted from [121]*

netism accounts for a magnetic moment lower than 0.05 emu/g along the a-axis below the SRT and of 0.1 emu/g along the c-axis above the SRT. [120].

Following the demonstration of ultrafast magnetization switching with a characteristic time of 4 ps induced by an ultrashort laser pulse [122], renewed interest has been given to TFO magnetic properties. [116, 120, 121, 123] However, with the notable exception of the work of Ahn and coworkers [123] who grew an epitaxial TFO film but in the hexagonal phase, all these studies have been performed on bulk crystals.

For this reason we were motivated in growing crystalline thin films based on the orthorhombic phase. First of all, we need to verify whether the bulk properties are maintained in thin films or not. Secondly, once uniform films can be grown, it becomes possible to produce multilayers and try to exploit interfacial effects to probe the magnetic state of TFO.

As commonly done for complex oxides, the choice of the growing technique fell on Pulsed Laser Deposition (see section 3.1.2) from a stoichiometric TmFeO$_3$target. The lack of suitable orthorhombic commercial substrates forces the use of available crystals with cubic perovskite structure. The conventional cell of Figure 6.1 has approximately the dimensions $\sqrt{2}a_P \times \sqrt{2}a_P \times 2a_P$ with a_P the cubic perovskite lattice constant. As it is impossible to find an ideal matching for the orthorhombic cell, two substrates with different lattice constants were considered: lanthanum aluminate - strontium aluminium tantalate (LSAT, a=3.868 Å) and strontium titanate (STO, a=3.905 Å). Because of some unsuccessful attempts with LSAT the focus has been given to STO substrates, with an optimized growth recipe for the KrF excimer laser as follows:

Laser wavelength	248 nm
Substrate temperature	973 K
Oxygen pressure	0.2 mbar
Oxygen flux	15 sccm
Pulse energy	120 mJ
Repetition rate	10 Hz
Deposition rate	1 nm/min

Table 6.1: *Growth conditions for TmFeO$_3$ on SrTiO$_3$.*

Following the deposition of TFO, a 4 nm thick Pt film was grown *ex-situ* by magnetron sputtering. To remove the water and atmospheric contaminants from the air-exposed surface, an annealing at 250 °C was carried out in ultrahigh vacuum for 30 minutes before the deposition. Sputtering conditions are summarized in Table 6.2.

Substrate temperature	350 K
Argon pressure	0.01 mbar
Plasma current	15 mA
Deposition rate	0.8Å/s

Table 6.2: *Sputtering condition of Pt thin films*

The overall quality of the film grown was assessed by X-Ray Diffraction (XRD). A representative XRD spectrum taken with a monochromatized Cu-K$_\alpha$ source on a Pt(3)/TFO(150)//STO(001) sample (thickness in nm) is reported in Figure 6.2a. The more intense peaks can be readily identified as peaks coming from the STO substrate (marked with S) and the TFO thin film (marked as T). The small signal coming from the Pt ultrathin film can not be distinguished in the tail of the main peaks and the small peak about 42°is probably a replica of the intense STO(002) peak with some leftover Cu-K$_\beta$ radiation. Therefore, a single-crystalline phase is observed for TFO on STO. Rocking curves around the TFO(001) diffraction peak were taken to reveal broadening of the peak width. Here the results were found different depending on the film thickness. On thinner samples (t_{TFO} = 30 nm) the rocking curve reveals a small dispersion with FWHM of about 0.1°(see Figure 6.2b) which indicates a good epitaxial growth. Instead thicker samples (t_{TFO} = 150 nm) show a broader structure (see Figure 6.2c), consistently with a relaxation of the strain and the development of mosaicity in the film. Despite this difference, both thinner and thicker samples gave comparable results for the electrical characterization of Pt as will be discussed in the next section. Finally, bare TFO thin films were also characterized *ex-situ* by photoelectron spectroscopy to verify the chemical composition. Even though nothing can be said for the oxygen stoichiometry because of the atmospheric contamination, the correct 1:1 ratio between Tm and Fe was measured within the experimental error bar of ±2%.
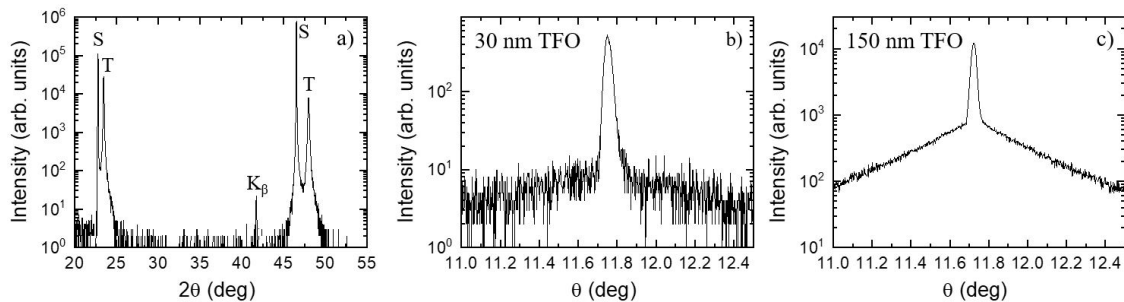

Figure 6.2: *X-Ray Diffraction of TmFeO$_3$ thin films. a) $\theta - 2\theta$ scan of a Pt(3)/TFO(150)//STO(001) sample. b) Rocking curve on the (002) reflection for TFO(30 nm) and c) TFO 150 nm).*
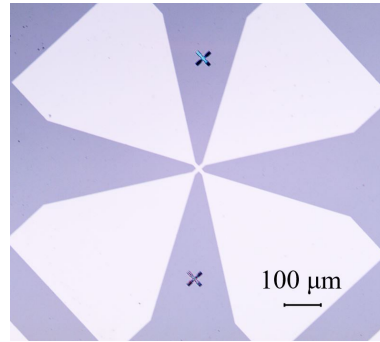
Figure 6.3: *Hall cross patterned by optical lithography and ion milling in Pt/TFO//STO.*
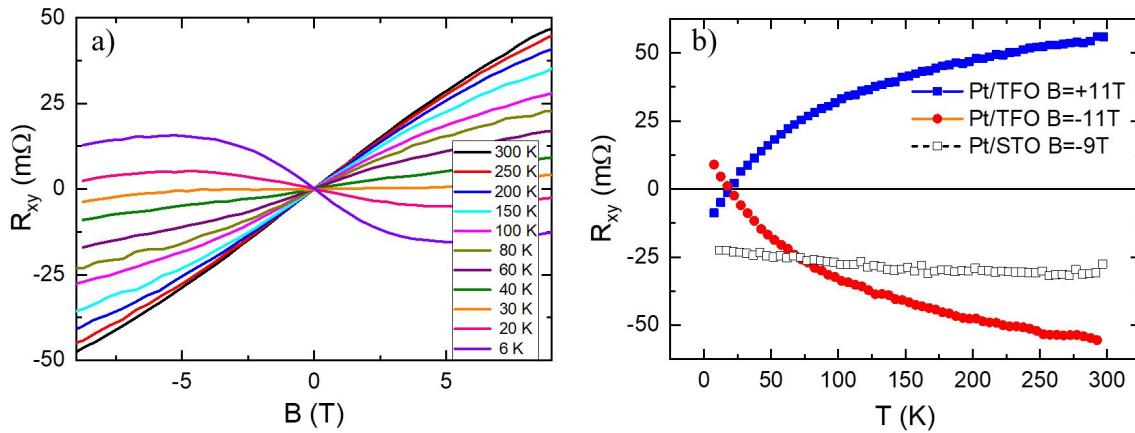

Figure 6.4: *Hall effect in Pt on TmFeO$_3$. a) Offset-compensated Hall resistance as a function of magnetic field for different temperatures b) Temperature dependence of the Hall resistance during field cooling processes. The measurement of a Pt film on diamagnetic STO substrate deposited in same run of the TFO sample is shown for comparison.*

6.2   Electrical transport of Pt films on TmFeO$_3$

Pt thin films deposited on top of insulating TFO were patterned in 10μ wide Hall crosses as the one pictured in Figure 6.3 using the optical lithography and ion-milling tools available in JGU. The measurement setup described in section 3.3.2 was integrated in an High-Field (up to 12 T) cryogenic apparatus (Oxford Instruments VSM MagLab) in Mainz for simultaneous measurement of longitudinal and offset-compensated transverse resistance.

6.2.1   Hall effect in Pt/TmFeO$_3$

Figure 6.4a reports the Hall resistance as a function of the out-of-plane field at different temperatures for a Pt(4)/TFO(150)//STO sample. Once again a strong temperature-dependence of the non-linear anomalous component is found. Differently from the case of t-Cr$_2$O$_3$(section 5.2.1), the anomalous Hall component is observed both at room temperature and approaching 0 K. Noteworthy the anomalous coefficient changes its sign in temperature as can be observed from the opposite slope of the curve around B = 0 at 300 K (black line) and 6 K (purple line) with a change of sign at about 40 K iden-
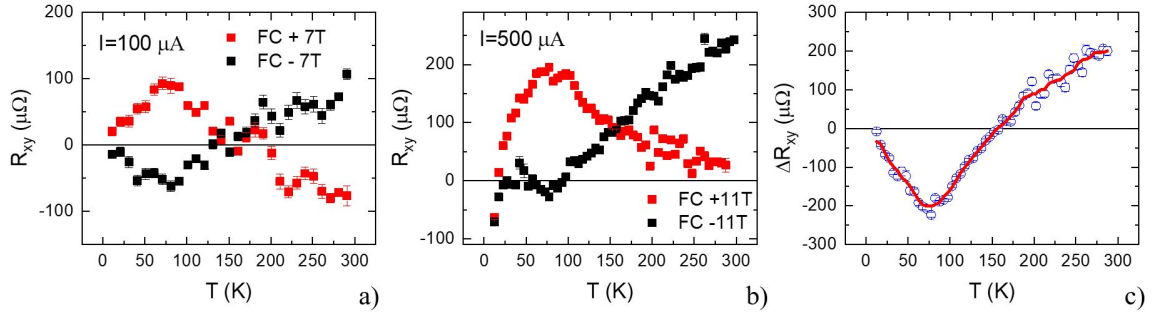
Figure 6.5: *Anomalous Hall effect at remanence in Pt(4)/TFO(150)//STO. a) Offset-compensated Hall resistance probed with a square wave of ±100 μA measured after setting a state with ±7 T applied. b) The same but the state is set with ±11 T and probed with a square wave of ±500 μA. c) Transverse resistance difference between the two states in b). The red line is a guide for the eye.*

tified by the (linear) ordinary Hall behavior of the green line. To better visualize the temperature trend, the transverse resistance monitored during several field cooling processes is shown in Figure 6.4b. As expected the curves are symmetrical with respect to 0 when the magnetic field is inverted (blue and red points corresponding to +11 T and -11 T, respectively). The curves, which account for both the anomalous and ordinary Hall, cross zero below 20 K. This is completely different from the Hall behavior of Pt. The measurement on a reference Pt/STO sample sputtered side by side with the TFO sample to get an immediately comparable measurement is also shown in Figure 6.4b. On diamagnetic STO, Pt shows just ordinary Hall effect, and temperature dependence is almost negligible (empty squares in Figure 6.4b). The interpretation of this behavior is not straightforward. Indeed, given the high T$_N$ of TFO, we expect it to be always in the antiferromagnetic phase, and this will be demonstrated shortly. For this reason, we can impute the anomalous Hall effect to interfacial mechanisms of magnetic proximty (MPE) and/or spin-Hall anomalous Hall (SHAHE). The change of sign of the anomalous Hall coefficient is instead less obvious. We can immediately exclude a magnetic phase transition as we will demonstrate that T$_N$> 300 K as in bulk TFO, but still we could consider a similar spin-reorientation transition to the one happening in TFO crystals. However, not only the temperature is lower than the one of the bulk SRT (between 82 and 93 K), but also the gradual drift of the anomalous Hall coefficient over the whole temperature range seems to exclude any sudden change in the magnetic configuration. Moreover, similar trends have been reported also for Pt on ferrimagnetic YIG [64, 79, 124] and it was demonstrated in that case to be related just to the temperature dependence of the AHE due to MPE independently of any magnetic phase transition. [79]

Even though the Néel temperature of TFO cannot be accessed in the cryostat, it is still possible to use large magnetic fields (|B| > 5 T) at room temperature to write a remanent state. In this case, the writing process is not a proper field cooling, since the Néel temperature is never crossed, but a reorientation of the canted antiferromagnetic domains promoted by large fields. Nevertheless, this approach is sufficient to set two well defined states for upward or downward applied field, as can be seen in Figure 6.5. In the first panel the two states are prepared by cooling the sample in ±7 T and measured while warming up in zero field with a current of ±100 μA. A
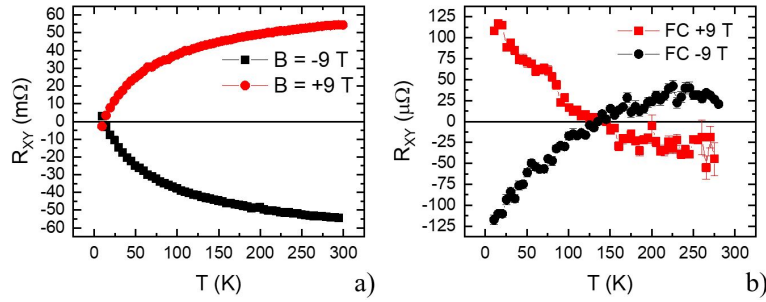
Figure 6.6: *Anomalous Hall effect in Pt(4)/TFO(30)//STO a) Offset-compensated Hall resistance in a field of ±9 T. b) Anomalous Hall resistance at remanence after the field cooling process.*

bias of ±70.0 Oe, previously determined by accurate calibration of the magnet, was employed to compensate for the stray field of trapped currents loops in the coils. The two states are symmetrical with respect to zero but, differently from the cases of Cr an t-Cr$_2$O$_3$already discussed in Chapters 4 and 5, the trend is not monotonous featuring a crossing between the two curves at 156 K whose is not yet understood. The signal remains non-zero at 300 K as the Néel temperature is expected to be much higher. Panel b) shows another measurement made during warming; in this case, the states are set with ±11 T and read with a square wave of ±500 μA. The effect of the latter on one side is to increase the signal-to-noise ratio but, on the other, the larger joule heating produces a non-compensated thermal offset which lifts evenly the two curves from the correct baseline. As usual, the difference between the two curves allows to disentangle only the signal of magnetic origin and is presented in Figure 6.5c. Finally, the increase in the writing field from 7 to 11 T does not produce any appreciable difference and the separation between the curves is the same in panel a) and b).

All the features highlighted on Pt(4)/TFO(150) were qualitatively reproduced in samples with thinner TFO. Figure 6.6 shows the transport properties in term of Hall resistance of a Pt(4)/TFO(30) device. The same temperature trend of transverse resistance (ordinary + anomalus Hall) of Figure 6.5b can be observed in (Figure 6.6a. R$_x y$ at 300 K in this case is slightly larger (54.2 mΩ compared to 47.4 mΩ) and this results also in a change of sign at a lower temperature. These differences can be accounted by slightly different morphologic properties of the Pt layer possibly influenced by the roughness of the TFO film, but the overall shape of the curve is unchanged. Regarding the remanent signal in Pt(3)/TFO(30), we observe again two different states which can be written by applying large magnetic fields and detected in the transverse resistance of Pt (see Figure 6.6b. Here some marked changes can be noted with respect to Figure 6.5, not just quantitatively but also qualitatively, considering the different slope at low temperature. Nevertheless, the puzzling sign inversion at about 150 K is reproducible in all devices, the use of electrical measurements alone however did not allow to correlate to a precise physical mechanism related to the spin structure of TFO. An explanation involving a competition between MPE AHE and SHAHE with opposite sign is also possible but would require an accurate analysis as a function of Pt thickness. In any case, even though the anomalous Hall resistance at remanence leaves some unanswered questions, indeed the interface effects in Pt/TFO allow to reveal the state of the antiferromagnet making possible the electrical reading on this interesting system and possibly
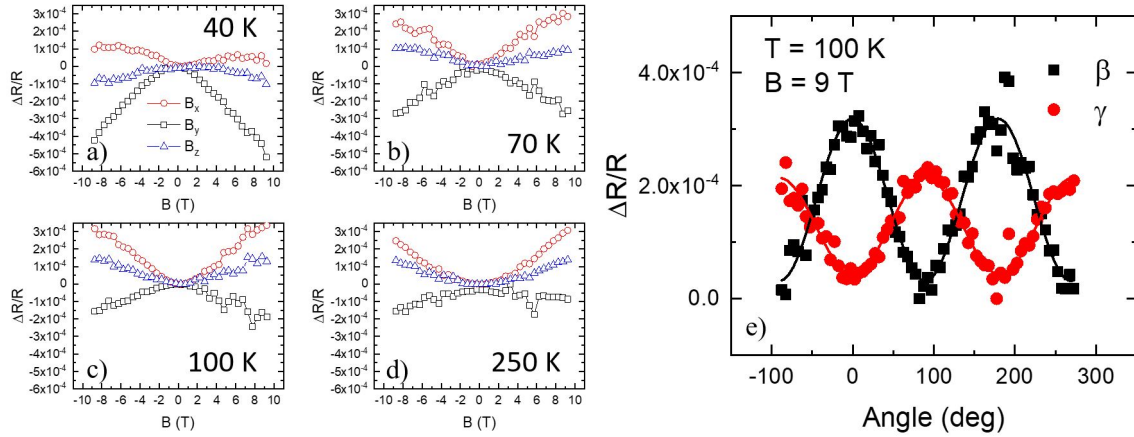
Figure 6.7: *Magnetoresistance in a representative Pt(4)/TFO(30) device. a-d) Relative change of longitudinal resistance as a function of field amplitude and direction at 40, 70, 100 and 250 K. e) Angle dependence of magnetoresistance for rotation along angles β and γ. The lines are fit with a $\sin^2$ function.*

on other ferrites as well.

6.2.2 Magnetoresistance in Pt/TmFeO$_3$

Longitudinal resistance has been characterized as well as a function of temperature and magnetic field. Moreover, by exploiting the possibility to orient the sample inside the magnetic field, we can distinguish AMR and SMR also determining their relative weight as we discussed in section 2.4.3. The results were consistent in all the devices tested; we show representative results in Figure 6.7 from a Pt(4)/TFO(30) device.

We start discussing the magnetoresistance and its dependence on the field direction by applying the field along three orthogonal directions. In analogy to what we did for t-Cr$_2$O$_3$ we follow the convention represented in Figure 2.10: x is the direction parallel to the current flow, y is the orthogonal direction in-plane and z is out-of-plane. x and y are also parallel to the crystallographic axes a and b of TFO (see Figure 6.1). Figures 6.7a-d shows the results obtained with the application of magnetic fields up to 9 T at temperatures from 40 to 250 K. In all cases, the curves for B_x, B_y ans B_z are well separated indicating a concurrence of both SMR and AMR as in the case of Pt/t-Cr$_2$O$_3$ in the paramagnetic phase (see Figure 5.9). No impact of the current amplitude (and so of Joule heating) on the MR ratio was detected, thus excluding a possible contribution of thermomagnetic effects. [125].

The behavior is only slightly affected by temperature as can be seen from the comparison of Figures 6.7a-d. This seems to exclude a possible spin-reorientation-transition in the interval tested.

Angle-dependent measurements, as shown in Figure 6.7e, confirm the expected $\sin^2$ dependence of magnetoresistance. Orthogonal rotations in the yz plane (angle β) and xz plane (angle γ) isolate the SMR and AMR term, respectively. Concerning the SMR term, we observe a "positive" sign as the one of Pt/YIG and other ferri or ferromagnetic systems. We recall from section 2.4.3 that in spin-flop antiferromagnets a negative SMR would be expected. This implies that the canted antiferromagnetism is still the most energetically-favorable state for TmFeO$_3$thin films even at 9 T (and also at 11 T,

not shown). This fosters the idea that a change in the anisotropy is never observed. In fact, approaching a SRT, one would expect a decrease of the anisotropy field H_a down to zero in correspondence of the transition itself. This would make easily accessible the spin-flop field H_{sf} since $H_{sf} \propto H_a^{\frac{1}{2}}$. [126]

In conclusion, longitudinal magnetoresistance measurements on Pt/TFO, still confirming the ubiquity of interfacial effects in similar heterostructures, do not reveal much on the underlying magnetic structure. AMR and positive SMR are observed with similar resistive modulations and those effects are compatible with the canting of AFM moments induced by the external field. The trivial result suggests however that the properties of TFO thin films are rather different with respect to bulk, lacking any anisotropy transition. Further work and complementary techniques are required to understand how the crystal structure affects so deeply the magnetic properties.

6.3 Discussion

In this chapter we have demonstrated the growth by Pulsed Laser Deposition of epitaxial TmFeO$_3$ thin films on SrTiO$_3$. Good crystalline quality can be obtained upon proper optimization of the growth parameters. Sputtered Pt has been used as conductive capping for the study of magnetic properties via electrical methods. Once more, after the cases of Cr and t-Cr$_2$O$_3$, electrical transport driven by interface effects proved to be an available route for retrieving information on the antiferromagnetic system. Indeed transport experiments alone did not allow to determine the spin structure and to highlight possible changes in the anisotropy, like the one found in bulk TFO at the spin-reorientation between 82.5 and 92.8 K. We recognize, however, that forcing an orthorhombic structure on a cubic substrate can affect the crystalline anisotropy, thus justifying the lack of any transition detected from the temperature dependence in magnetoresistance. This is indeed also the case of hexagonal TFO thin films, [123] which however presents a completely different structure. Certainly, a definitive answer in this regard could come from linear dichroism experiments on these films, which are planned for the future.

It is however established by anomalous Hall at remanence that the material is antiferromagnetic up (at least) to room temperature and, if the Néel transition is not too high, electrical measurements could be used to determine it in a measurement setup with sample heating. The peculiar signal with a sign inversion of the anomalous Hall resistance at the moment is not fully understood, a transverse voltage originating from SHAHE should never change sign as no parameter in equations 2.19 and 2.18 could invert with temperature. Considering instead the AHE coming from magnetic proximity the situation can get a bit more complicated. The temperature dependence of the MPE is not much understood especially on Pt/oxides where the magnetization tail penetrating in the Pt layer is predicted to be $< 0.1 \ \mu_B$. [127] However, different magnetized layers of Pt not necessarily contribute to total AHE with the same sign and anomalous Hall coefficient and thermal dependence of magnetization has to be considered layer by layer. [128] Finally, also a superposition of AHE and SHAHE with opposite signs and different thermal dependence could explain the crossing. A series of new experiments with different capping thicknesses and the use of interlayers can possibly settle this point.

In any case, even though many open points remain on the physical interpretation of the results, this work clearly showed the possibility to grow antiferromagnetic TFO and detect its magnetic state as a transverse resistance and, by extension, in the class of ferrites. Thus opening up novel opportunities for the characterization and for the possible exploitation of these interesting materials in antiferromagnet spintronics.

CHAPTER 7

Conclusions

This work deals with the investigation of antiferromagnetic thin films through electrical measurements, with particular focus on anomalous Hall effect coming from non-magnetic/antiferromagnetic interfaces. We showed how surface effects like magnetic proximity or spin-Hall magnetoresistance, beside being an intriguing phenomenon in condensed matter physics, provide a powerful investigation tool for the fundamental study of antiferromagnets and can find application as well in the field of information technology. In fact, the possibility to detect the antiferromagnetic state is one of the key element for the realization of magnetic memory cells which, free of any ferromagnetic element, would allow a fast, nonvolatile storage which is robust against external magnetic fields.

Few antiferromagnetic materials were reported to display measurable transport properties dependent on the antiferromagnetic state, with notable examples like CuMnAs, Mn_2Au, FeRh, Mn_3Ge, and Mn_3Sn. Nevertheless, most of the other metallic antiferromagnets do not show any measurable electrical signal responding to the magnetic configuration and, of course, all the insulating antiferromagnets can not be even considered for this purpose. The relative scarcity of materials displaying both antiferromagnetism and magneto-transport properties can be overcome resorting to composite heterostructures where the antiferromagnet is interfaced with non-magnetic metals, like the ones that we presented in this thesis (in bold the antiferromagnetic/non-magnetic bilayer):

1. **Pt/Cr**//MgO

2. **Ta/IrMn/Ta**//SiO_2

3. **Pt/t-Cr_2O_3**/$BaTiO_3$//$SrTiO_3$

4. **Pt/TmFeO$_3$**//$SrTiO_3$

Following a similar approach in all these cases, a magnetic configuration is prepared in the device by means of field-cooling and the resulting state is then detected by means of Hall measurements performed at remanence. Notably, this approach can be generally applied to both metallic and insulating antiferromagnets, disclosing unexplored possibilities in the field of antiferromagnet spintronics.

In Pt/Cr an anomalous Hall resistance up to $\pm 2.8 \mu\Omega$ was observed at low temperature. Its origin is intimately tied to the antiferromagnetism of Cr, and disappears when the Néel temperature is reached. Chromium by itself allows an independent detection of the antiferromagnetic transition by conventional measurements of longitudinal transport and ordinary Hall effect as a consequence of its spin density wave nature that opens a gap in the band structure at the Néel temperature. Nevertheless, an electrical reading of the antiferromagnetic state, while possible in perfectly ordered bulk crystals, [48] has never been observed in thin films. By interfacing Cr with Pt, instead, the anomalous Hall effect makes possible to easily distinguish states stored by field cooling with opposite out-of-plane fields.

The specific role of Pt in the origin of this effect has been proved by varying its thickness in multiple samples or by interposing an ultrathin Au layer. The disappearance of anomalous Hall in the latter case demonstrates the interfacial nature of this effect, and fits with the theoretical predictions of a proximity induced magnetization in Pt by neighboring antiferromagnetic Cr.

The same phenomenon was observed in the other two systems that have been discussed: Pt/t-Cr_2O_3 and Pt/$TmFeO_3$. In these cases we are dealing with insulating antiferromagnets, whose properties could never be accessed directly. Nevertheless, thanks to the exploitation of interface effects, we could determine the antiferromagnetic character of both and read electrically the magnetic state written by field-cooling.

We introduced t-Cr_2O_3 as a rarely observed phase of Cr (III) oxide, we showed a possible route to synthesize it in the form of ultrathin films which are stable on perovskite $BaTiO_3$, and we combined several spectroscopic and diffraction techniques to determine its structural composition as a tetragonally-distorted defective rocksalt. Finally, by measurements of spin-Hall magnetoresistance and anomalous Hall effect as a function of temperature, we have been able to demonstrate the antiferromagnetic phase transition of this system at about 40 K.

The observed Néel temperature is much lower than the one predicted for bulk by *ab initio* calculations (T_N=643 K): we could expect this discrepancy to be related to the low dimensionality of the system, which is only few nm thick, and to the intrinsic disorder of Cr vacancies in the defective rocksalt cell.

At last, we optimized the growth of single-crystalline films of the rare-earth orthoferrite $TmFeO_3$ and demonstrated its antiferromagnetism. The interest in $TmFeO_3$ is motivated by the strong temperature dependence of the anisotropy leading to a spontaneous spin-reorientation transition, which opens up to possible manipulations of the antiferromagnetic state in ultrafast processes on the ps scale. However, all the available reports to date on thulium orthoferrite magnetism regard bulk crystals only, and the properties of thin films are yet to be determined.

By measuring anomalous Hall effect in Pt/$TmFeO_3$ we could assess the antiferromagnetic character of epitaxial $TmFeO_3$ grown on cubic $SrTiO_3$ up to (at least) room temperature. No direct evidence of the spin-reorientation transition was observed from

electrical measurements in the temperature range explored. While other investigations are planned to clarify this point, it should not be surprising that the material properties of $TmFeO_3$ may change in thin film form. In particular, the growth of a material which is orthorhombic in the bulk on a cubic substrate necessarily induces strain which impacts on the cell geometry. As magnetic anisotropy can be very sensitive to the crystal structure, this could justify the lack of the spin-reorientation transition.

In perspective, once we demonstrated that the epitaxial growth is possible on $SrTiO_3$, other substrates could be considered as well, in order to verify whether the peculiar properties of bulk $TmFeO_3$ crystals can be reproduced, under specific conditions, also in thin films.

To conclude, the growth of different antiferromagnetic systems, including novel compounds like t-Cr_2O_3 and $TmFeO_3$ thin films, has been covered. The investigation of their magnetic properties has been conducted by means of electrical methods. In particular, effects arising from interfaces, namely magnetic proximity and spin-Hall magnetoresistance, have been generally observed in Pt/AFM heterostructures, thus enabling the detection of the Néel temperature and of the state set by field cooling.

The setup employed can be easily replicated in most of the academic laboratories, involving only commonly available instrumentation and a relay switching matrix which can be rapidly and cost-effectively reproduced, thus providing an immediate characterization tool for antiferromagnetic thin films and a testbed for their spintronic application.

Finally, as other non-magnetic materials can replace Pt (for instance Pd, Ir, Ta, W or V), countless combinations with antiferromagnets can be imagined, possibly disclosing novel phenomena on which future devices can be built, once again thanks to interfaces.

Relay switching matrix implementation

The measurement of resistivity using the van der Pauw method requires two non-local acquisitions along orthogonal directions as in Figure 3.7 while the offset compensation in Hall measurements requires other two transverse voltage acquisitions as in Figure 3.8. Considering that the current reversal can be provided from the bipolar current source Keithley 6221, just these four contacts configurations are required.

To achieve the automatic switching between the four states we designed a simple and inexpensive circuit out of three reed relays governed by an Atmel ATmega328P microcontroller on a hobbyist Arduino board. A schematic of the circuit layout is presented in Figure A.1a.

The microcontroller controls independently each relay with three of its general pur-
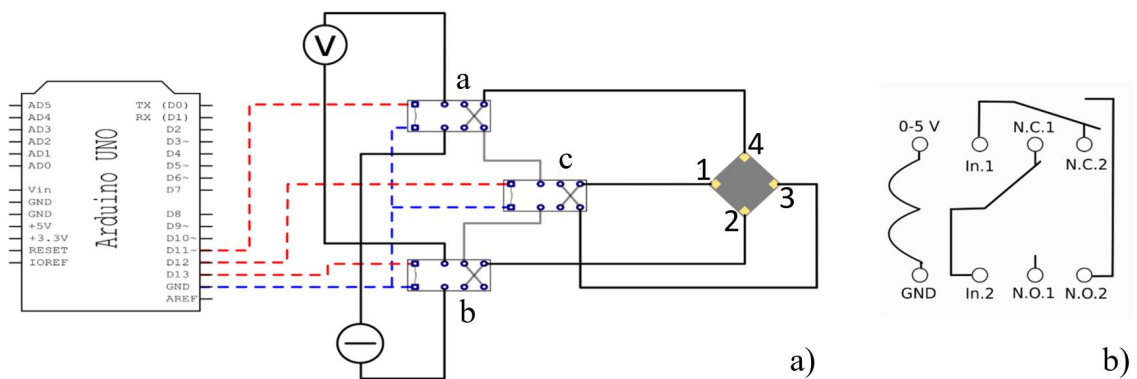
Figure A.1: *a) Relay switching matrix circuital implementation. Red dashed lines are the controlled outputs of the microcontroller governing the reed relays* a, b *and* c, *while the blue dashed line is the common ground connection. b) Pin diagram of DIL05-2C90-63L relays.*

pose outputs (D11, D12 and D13) through the red dashed lines in Figure A.1. The low impedance reed relays that have been used are model DIL05-2C90-63L from Meder Electronic Inc. Those are double pole double throw (DPDT) relays, meaning that there are two coils switching simultaneously both acting on deviator switches as can be seen from the diagram in Figure A.1b. Relays are guaranteed for long endurance ($>10^9$ commutations) and fast switching (< 1 ms). The current source and the nanovoltmeter are connected to the input pins of relays a and b and then rerouted through an appropriate network towards the sample.

With regard to the diagram in Figure A.1, the four configurations can be obtained by switching the relays on and off according to Table A.1.

Measurement	Current probes	Voltage probes	Relay a	Relay b	Relay c
Van der Pauw 1	1, 4	2, 3	On	Off	On
Van der Pauw 2	1, 2	3, 4	Off	On	Off
Hall 1	2, 4	1, 3	On	On	Off
Hall 2	1, 3	2, 4	Off	Off	Off

Table A.1: *Measurement configurations and corresponding relay patterns.*

The graphical representation of all the four configurations with the signal paths highlighted is provided in Figure A.2.
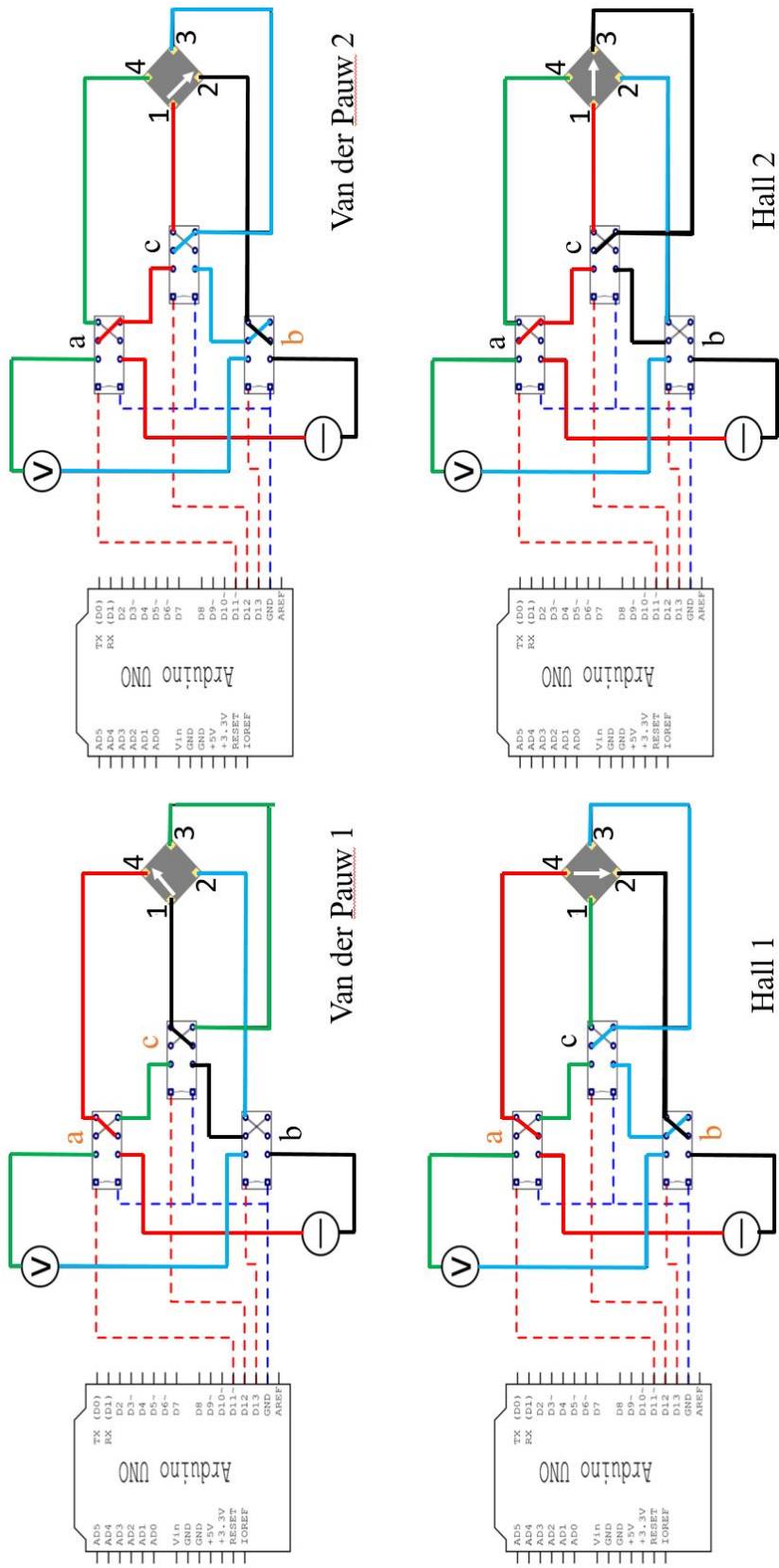
Figure A.2: *Relay configurations and relative signal path. Red and black lines represent the outputs of the current source, blue and green lines the probes of the nanovoltmeter. Relay names are indicated in black if turned off or orange if on. The current direction on the sample is represented by the white arrow.*

List of Figures

Bibliography

[1] Marco Asa, Lorenzo Baldrati, Christian Rinaldi, Stefano Bertoli, Greta Radaelli, Matteo Cantoni, and Riccardo Bertacco. Electric field control of magnetic properties and electron transport in BaTiO 3 -based multiferroic heterostructures. *Journal of Physics: Condensed Matter*, 27(50):504004, dec 2015.

[2] Marcus Liebmann, Christian Rinaldi, Domenico Di Sante, Jens Kellner, Christian Pauly, Rui Ning Wang, Jos Emiel Boschker, Alessandro Giussani, Stefano Bertoli, Matteo Cantoni, Lorenzo Baldrati, Marco Asa, Ivana Vobornik, Giancarlo Panaccione, Dmitry Marchenko, Jaime Sánchez-Barriga, Oliver Rader, Raffaella Calarco, Silvia Picozzi, Riccardo Bertacco, and Markus Morgenstern. Giant Rashba-Type Spin Splitting in Ferroelectric GeTe(111). *Advanced Materials*, 28(3):560–565, jan 2016.

[3] Lorenzo Baldrati, Christian Rinaldi, Alberto Manuzzi, Marco Asa, Lucia Aballe, Michael Foerster, Neven Biškup, Maria Varela, Matteo Cantoni, and Riccardo Bertacco. Electrical Switching of Magnetization in the Artificial Multiferroic CoFeB/BaTiO 3. *Advanced Electronic Materials*, 2(7):1600085, jul 2016.

[4] C. Rinaldi, J. C. Rojas-Sánchez, R. N. Wang, Y. Fu, S. Oyarzun, L. Vila, S. Bertoli, M. Asa, L. Baldrati, M. Cantoni, J.-M. George, R. Calarco, A. Fert, and R. Bertacco. Evidence for spin to charge conversion in GeTe(111). *APL Materials*, 4(3):032501, mar 2016.

[5] C. Rinaldi, S. Bertoli, M. Asa, L. Baldrati, C. Manzoni, M. Marangoni, G. Cerullo, M. Bianchi, R. Sordan, R. Bertacco, and M. Cantoni. Determination of the spin diffusion length in germanium by spin optical orientation and electrical spin injection. *Journal of Physics D: Applied Physics*, 49(42):425104, oct 2016.

[6] Marco Asa and Riccardo Bertacco. Impact of semiconducting electrodes on the electroresistance of ferroelectric tunnel junctions. *Applied Physics Letters*, 112(8):082903, feb 2018.

[7] M. Asa, G. Vinai, J. L. Hart, C. Autieri, C. Rinaldi, P. Torelli, G. Panaccione, M. L. Taheri, S. Picozzi, and M. Cantoni. Interdiffusion-driven synthesis of tetragonal chromium (III) oxide on BaTiO3. *Physical Review Materials*, 2(3):033401, mar 2018.

[8] Christian Rinaldi, Lorenzo Baldrati, Matteo Di Loreto, Marco Asa, Riccardo Bertacco, and Matteo Cantoni. Blocking Temperature Engineering in Exchange-Biased CoFeB/IrMn Bilayer. *IEEE Transactions on Magnetics*, 54(4):1–7, apr 2018.

[9] Christian Rinaldi, Sara Varotto, Marco Asa, Jagoda Sławińska, Jun Fujii, Giovanni Vinai, Stefano Cecchi, Domenico Di Sante, Raffaella Calarco, Ivana Vobornik, Giancarlo Panaccione, Silvia Picozzi, and Riccardo Bertacco. Ferroelectric Control of the Spin Texture in GeTe. *Nano Letters*, 18(5):2751–2758, may 2018.

[10] Herbert Kroemer. Nobel lecture: Quasielectric fields and band offsets: Teaching electrons new tricks, 2001.

[11] A Ohtomo and H Y Hwang. A high-mobility electron gas at the LAO/STO heterointerface. *Nature*, 2004.

[12] S. Tehrani, E. Chen, M. Durlam, M. DeHerrera, J. M. Slaughter, J. Shi, and G. Kerszykowski. High Density Submicron Magnetoresistive Random Access Memory. *Journal of Applied Physics*, 85(8):5822, 1999.

[13] S. Tehrani, B. Engel, J.M. Slaughter, E. Chen, M. DeHerrera, M. Durlam, P. Naji, R. Whig, J. Janesky, and J. Calder. Recent Developments in Magnetic Tunnel Junction MRAM. *IEEE Transactions on Magnetics*, 36(5):2752–2757, 2000.

Bibliography

[14] RC Sousa and IL Prejbeanu. Non-volatile magnetic random access memories (MRAM). *Comptes Rendus Physique*, (October), 2005.

[15] Claude Chappert, Albert Fert, and Frédéric Nguyen Van Dau. The Emergence of Spin Electronics in Data Storage. *Nature materials*, 6(11):813–23, nov 2007.

[16] J. Akerman. Toward a Universal Memory. *Science*, 308(5721):508–510, apr 2005.

[17] D.C. Ralph and M.D. Stiles. Spin Transfer Torques. *Journal of Magnetism and Magnetic Materials*, 320(7):1190–1216, apr 2008.

[18] A V Khvalkovskiy, D Apalkov, S Watts, R Chepulskii, R S Beach, A Ong, X Tang, A Driskill-Smith, W H Butler, P B Visscher, D Lottis, E Chen, V Nikitin, and M Krounbi. Basic principles of STT-MRAM cell operation in memory arrays. *Journal of Physics D: Applied Physics*, 46(13):139601, apr 2013.

[19] Xuanyao Fong, Yusung Kim, Rangharajan Venkatesan, Sri Harsha Choday, Anand Raghunathan, and Kaushik Roy. Spin-Transfer Torque Memories: Devices, Circuits, and Systems. *Proceedings of the IEEE*, 104(7):1449–1488, jul 2016.

[20] A. Manchon, I. M. Miron, T. Jungwirth, J. Sinova, J. Zelezný, A. Thiaville, K. Garello, and P. Gambardella. Current-induced spin-orbit torques in ferromagnetic and antiferromagnetic systems. (January), jan 2018.

[21] T. Jungwirth, X. Marti, P. Wadley, and J. Wunderlich. Antiferromagnetic spintronics, 2016.

[22] Matthias B. Jungfleisch, Wei Zhang, and Axel Hoffmann. Perspectives of antiferromagnetic spintronics. *Physics Letters A*, 382(13):865–871, apr 2018.

[23] T. Jungwirth, J. Sinova, A. Manchon, X. Marti, J. Wunderlich, and C. Felser. The multiple directions of antiferromagnetic spintronics. *Nature Physics*, 14(3):200–203, mar 2018.

[24] N. F. Kharchenko. On seven decades of antiferromagnetism. *Low Temperature Physics*, 31(8):633–634, aug 2005.

[25] Louis Néel. Magnetism and Local Molecular Field. *Science*, 174(4013):985–992, 1971.

[26] R. L. Stamps. Mechanisms for exchange bias. *Journal of Physics D: Applied Physics*, 2000.

[27] L.D. Landau and E.M. Lifshitz. Ferromagnetism and antiferromagnetsim. In *Electrodynamics of Continuous Media*, pages 130–179. Elsevier, 1984.

[28] C. G. Shull and J. Samuel Smart. Detection of Antiferromagnetism by Neutron Diffraction. *Physical Review*, 76(8):1256–1257, oct 1949.

[29] J. Stöhr, H. A. Padmore, S. Anders, T. Stammler, and M. R. Scheinfein. Principles of X-Ray Magnetic Dichroism Spectromicroscopy. *Surface Review and Letters*, 05(06):1297–1308, dec 1998.

[30] A. B. Shick, S. Khmelevskyi, O. N. Mryasov, J. Wunderlich, and T. Jungwirth. Spin-orbit coupling induced anisotropy effects in bimetallic antiferromagnets: A route towards antiferromagnetic spintronics. *Physical Review B - Condensed Matter and Materials Physics*, 2010.

[31] B. G. Park, J. Wunderlich, X. Martí, V. Holý, Y. Kurosaki, M. Yamada, H. Yamamoto, A. Nishide, J. Hayakawa, H. Takahashi, A. B. Shick, and T. Jungwirth. A spin-valve-like magnetoresistance of an antiferromagnet-based tunnel junction. *Nature Materials*, 10(5):347–351, may 2011.

[32] D. Petti, E. Albisetti, H. Reichlová, J. Gazquez, M. Varela, M. Molina-Ruiz, A. F. Lopeandía, K. Olejník, V. Novák, I. Fina, B. Dkhil, J. Hayakawa, X. Marti, J. Wunderlich, T. Jungwirth, and R. Bertacco. Storing magnetic information in IrMn/MgO/Ta tunnel junctions via field-cooling. *Applied Physics Letters*, 102(19):192404, may 2013.

[33] X. Marti, I. Fina, C. Frontera, Jian Liu, P. Wadley, Q. He, R. J. Paull, J. D. Clarkson, J. Kudrnovský, I. Turek, J. Kuneš, D. Yi, J-H. Chu, C. T. Nelson, L. You, E. Arenholz, S. Salahuddin, J. Fontcuberta, T. Jungwirth, and R. Ramesh. Room-temperature antiferromagnetic memory resistor. *Nature Materials*, 13(4):367–374, apr 2014.

[34] I. Fina, X. Marti, D. Yi, J. Liu, J. H. Chu, C. Rayan-Serrao, S. Suresha, A. B. Shick, J. Železný, T. Jungwirth, J. Fontcuberta, and R. Ramesh. Anisotropic magnetoresistance in an antiferromagnetic semiconductor. *Nature Communications*, 5(1):4671, dec 2014.

[35] P. Wadley, B. Howells, J. Železný, C. Andrews, V. Hills, R. P. Campion, V. Novák, K. Olejník, F. Maccherozzi, S. S. Dhesi, S. Y. Martin, T. Wagner, J. Wunderlich, F. Freimuth, Y. Mokrousov, J. Kuneš, J. S. Chauhan, M. J. Grzybowski, A. W. Rushforth, Kw Edmond, B. L. Gallagher, and T. Jungwirth. Electrical switching of an antiferromagnet. *Science*, 351(6273):587–590, 2016.

[36] S. Yu. Bodnar, L. Šmejkal, I. Turek, T. Jungwirth, O. Gomonay, J. Sinova, A. A. Sapozhnik, H.-J. Elmers, M. Kläui, and M. Jourdan. Writing and reading antiferromagnetic Mn2Au by Néel spin-orbit torques and large anisotropic magnetoresistance. *Nature Communications*, 9(1):348, dec 2018.

[37] J. Železný, H. Gao, K. Výborný, J. Zemen, J. Mašek, Aurélien Manchon, J. Wunderlich, Jairo Sinova, and T. Jungwirth. Relativistic néel-order fields induced by electrical current in antiferromagnets. *Physical Review Letters*, 113(15):1–5, 2014.

[38] K. Olejník, V. Schuler, X. Marti, V. Novák, Z. Kašpar, P. Wadley, R. P. Campion, K. W. Edmonds, B. L. Gallagher, J. Garces, M. Baumgartner, P. Gambardella, and T. Jungwirth. Antiferromagnetic CuMnAs multi-level memory cell with microelectronic compatibility. *Nature Communications*, 8:15434, may 2017.

[39] Kamil Olejník, Tom Seifert, Zdeněk Kašpar, Vít Novák, Peter Wadley, Richard P. Campion, Manuel Baumgartner, Pietro Gambardella, Petr Němec, Joerg Wunderlich, Jairo Sinova, Petr Kužel, Melanie Müller, Tobias Kampfrath, and Tomas Jungwirth. Terahertz electrical writing speed in an antiferromagnetic memory. *Science Advances*, 4(3):eaar3566, mar 2018.

[40] Takahiro Moriyama, Kent Oda, Takuo Ohkochi, Motoi Kimata, and Teruo Ono. Spin torque control of antiferromagnetic moments in NiO. *Scientific Reports*, 8(1):14167, dec 2018.

[41] Lorenzo Baldrati, Olena Gomonay, Andrew Ross, Mariia Filianina, Romain Lebrun, Rafael Ramos, Cyril Leveille, Thomas Forrest, Francesco Maccherozzi, Eiji Saitoh, Jairo Sinova, and Mathias Kläui. Mechanism of Neel order switching in antiferromagnetic thin films revealed by magnetotransport and direct imaging. oct 2018.

[42] Isaiah Gray, Takahiro Moriyama, Nikhil Sivadas, Ryan Need, Brian J. Kirby, David H. Low, Gregory M. Stiehl, John T. Heron, Daniel C. Ralph, Katja C. Nowack, Teruo Ono, and Gregory D. Fuchs. Spin Seebeck imaging of spin-torque switching in antiferromagnetic Pt/NiO/Pt heterostructures. oct 2018.

[43] Tobias Kosub, Martin Kopte, Ruben Hühne, Patrick Appel, Brendan Shields, Patrick Maletinsky, René Hübner, Maciej Oskar Liedke, Jürgen Fassbender, Oliver G. Schmidt, and Denys Makarov. Purely antiferromagnetic magnetoelectric random access memory. *Nature Communications*, 8:13985, 2017.

[44] V. J. Folen, G. T. Rado, and E. W. Stalder. Anisotropy of the Magnetoelectric Effect in Cr2O3. *Physical Review Letters*, 6(11):607–608, jun 1961.

[45] Stephen Blundell. *Magnetism in Condensed Matter*. Oxford University Press, 1 edition, 2001.

[46] Neil W Ashcroft and N David Mermin. *Solid State Physics*. 1976.

[47] Eric Fawcett. Spin-density-wave antiferromagnetism in chromium. *Reviews of Modern Physics*, 37(1):209–293, 1988.

[48] W. B. Muir and J. O. Ström-Olsen. Electrical Resistance of Single-Crystal Single-Domain Chromium from 77 to 325 K. *Physical Review B*, 4(3):988–991, aug 1971.

[49] J. Mattson, B. Brumitt, M. B. Brodsky, and J. B. Ketterson. Magnetotransport studies of epitaxial Cr thin films. *Journal of Applied Physics*, 67(9):4889–4891, 1990.

[50] P. Sonntag, P. Bödeker, K. Bröhl, T. Thurston, and H. Zabel. Charge density waves and strain waves in thin epitaxial Cr films. *Nuclear Instruments and Methods in Physics Research Section B: Beam Interactions with Materials and Atoms*, 97(1-4):468–471, may 1995.

[51] P Sonntag, P Bödeker, a Schreyer, H Zabel, K Hamacher, and H Kaiser. Magnetic phase diagram for spin-density waves in thin epitaxial Cr(001) films. *Journal of Magnetism and Magnetic Materials*, 183(1-2):5–18, 1998.

[52] J. Meersschaut, J. Dekoster, R. Schad, P. Beliën, and M. Rots. Spin Density Wave Instability for Chromium in Fe/Cr(100) Multilayers. *Physical Review Letters*, 75(8):1638–1641, aug 1995.

[53] P. Bödeker, A. Schreyer, Zabel, and H. Spin-density waves and reorientation effects in thin epitaxial Cr films covered with ferromagnetic and paramagnetic layers. *Physical Review B*, 59(14):9408–9431, apr 1999.

[54] Ravi K Kummamuru and Yeong-ah Soh. Electrical effects of spin density wave quantization and magnetic domain walls in chromium. *Nature*, 452(April), 2008.

[55] A. A. Povzner, A. G. Volkov, and A. N. Filanovich. Electronic structure and magnetic susceptibility of nearly magnetic metals (palladium and platinum). *Physics of the Solid State*, 52(10):2012–2018, oct 2010.

[56] Y. S. Shi, D. Qian, G. S. Dong, X. F. Jin, and Ding-Sheng Wang. Electronic structure and magnetism of Fe(1-x)-Pd(x) alloys. *Physical Review B*, 65(17):172410, apr 2002.

Bibliography

[57] M.F. Wang, Y.S. Shi, D. Qian, G.S. Dong, and X.F. Jin. Electronic structure and magnetism of Co1-xPdx alloys. *Journal of Magnetism and Magnetic Materials*, 272-276:788–789, may 2004.

[58] Y. Sun, J. D. Burton, and E. Y. Tsymbal. Electrically Driven Magnetism on a Pd thin film. *Physical Review B*, 81(6):064413, feb 2010.

[59] Lei Liang, Qihong Chen, Jianming Lu, Wytse Talsma, Juan Shan, Graeme R. Blake, Thomas T.M. Palstra, and Jianting Ye. Inducing ferromagnetism and kondo effect in platinum by paramagnetic ionic gating. *Science Advances*, 4(4):1–8, 2018.

[60] W.J Antel, M.M. Schwickert, Tao Lin, W.L. O'Brien, and G.R. Harp. Induced ferromagnetism and anisotropy of pt layers in fe/pt(001) multilayers. *Physical Review B - Condensed Matter and Materials Physics*, 60(18):12933–12940, 1999.

[61] G. Schütz, S. Stähler, M. Knülle, P. Fischer, S. Parkin, and H. Ebert. Distribution of magnetic moments in Co/Pt and Co/Pt/Ir/Pt multilayers detected by magnetic x-ray absorption. *Journal of Applied Physics*, 73(10):6430–6432, 1993.

[62] F. Wilhelm, P. Poulopoulos, G. Ceballos, H. Wende, K. Baberschke, P. Srivastava, D. Benea, H. Ebert, M. Angelakeris, N. K. Flevaris, D. Niarchos, A. Rogalev, and N. B. Brookes. Layer-resolved magnetic moments in Ni/Pt multilayers. *Physical Review Letters*, 85(2):413–416, 2000.

[63] F. Wilhelm, P. Poulopoulos, H. Wende, A. Scherz, K. Baberschke, M. Angelakeris, N. K. Flevaris, and A. Rogalev. Systematics of the induced magnetic moments in 5d layers and the violation of the third hund's rule. *Physical Review Letters*, 87(20):207202–1–207202–4, 2001.

[64] Y. M. Lu, Y. Choi, C. M. Ortega, X. M. Cheng, J. W. Cai, S. Y. Huang, L. Sun, and C. L. Chien. Pt magnetic polarization on Y3Fe5O12 and magnetotransport characteristics. *Physical Review Letters*, 110(14):1–5, 2013.

[65] Stephan Geprägs, Sibylle Meyer, Stephan Altmannshofer, Matthias Opel, Fabrice Wilhelm, Andrei Rogalev, Rudolf Gross, and Sebastian T.B. Goennenwein. Investigation of induced Pt magnetic polarization in Pt/Y3Fe5O12bilayers. *Applied Physics Letters*, 101(26), 2012.

[66] Robert Karplus and J. M. Luttinger. Hall Effect in Ferromagnetics. *Physical Review*, 95(5):1154–1160, sep 1954.

[67] J. Smit and J. Volger. Spontaneous Hall Effect in Ferromagnetics. *Physical Review*, 92(6):1576–1577, dec 1953.

[68] L. Berger. Side-jump mechanism for the hall effect of ferromagnets. *Physical Review B*, 2(11):4559–4566, 1970.

[69] Satoru Nakatsuji, Naoki Kiyohara, and Tomoya Higo. Large anomalous Hall effect in a non-collinear antiferromagnet at room temperature. *Nature*, 527(7577):212–215, nov 2015.

[70] Ajaya K. Nayak, Julia Erika Fischer, Yan Sun, Binghai Yan, Julie Karel, Alexander C. Komarek, Chandra Shekhar, Nitesh Kumar, Walter Schnelle, J. Ku bler, Claudia Felser, and S. S. P. Parkin. Large anomalous Hall effect driven by a nonvanishing Berry curvature in the noncolinear antiferromagnet Mn3Ge. *Science Advances*, 2(4):e1501870–e1501870, apr 2016.

[71] J. Yan, X. Luo, F. C. Chen, Q. L. Pei, G. T. Lin, Y. Y. Han, L. Hu, P. Tong, W. H. Song, X. B. Zhu, and Y. P. Sun. Anomalous Hall effect in two-dimensional non-collinear antiferromagnetic semiconductor Cr0.68Se. *Applied Physics Letters*, 111(2):1–14, 2017.

[72] Tobias Kosub, Martin Kopte, Florin Radu, Oliver G. Schmidt, and Denys Makarov. All-Electric Access to the Magnetic-Field-Invariant Magnetization of Antiferromagnets. *Physical Review Letters*, 115(9), 2015.

[73] W. Thomson. XIX. On the electro-dynamic qualities of metals: Effects of magnetization on the electric conductivity of nickel and of iron. *Proceedings of the Royal Society of London*, 8:546–550, jan 1857.

[74] J. E. Hirsch. Spin Hall Effect. *Physical Review Letters*, 83(9):1834–1837, aug 1999.

[75] Stephen R Boona, Roberto C Myers, and Joseph P Heremans. Spin caloritronics. *Energy & Environmental Science*, 7(3):885, 2014.

[76] H. Nakayama, M. Althammer, Y. T. Chen, K. Uchida, Y. Kajiwara, D. Kikuchi, T. Ohtani, S. Geprägs, M. Opel, S. Takahashi, R. Gross, G. E W Bauer, S. T B Goennenwein, and E. Saitoh. Spin Hall Magnetoresistance Induced by a Nonequilibrium Proximity Effect. *Physical Review Letters*, 110(20):1–5, 2013.

[77] N. Vlietstra, J. Shan, V. Castel, B. J. Van Wees, and J. Ben Youssef. Spin-Hall magnetoresistance in platinum on yttrium iron garnet: Dependence on platinum thickness and in-plane/out-of-plane magnetization. *Physical Review B - Condensed Matter and Materials Physics*, 87(18):1–5, 2013.

[78] Yan-Ting Chen, Saburo Takahashi, Hiroyasu Nakayama, Matthias Althammer, Sebastian T. B. Goennenwein, Eiji Saitoh, and Gerrit E. W. Bauer. Theory of spin Hall magnetoresistance. *Physical Review B*, 87(14):144411, 2013.

[79] X. Zhou, L. Ma, Z. Shi, W. J. Fan, Jian Guo Zheng, R. F.L. Evans, and S. M. Zhou. Magnetotransport in metal/insulating-ferromagnet heterostructures: Spin Hall magnetoresistance or magnetic proximity effect. *Physical Review B - Condensed Matter and Materials Physics*, 92(6):1–5, 2015.

[80] Lifan Zhou, Hongkang Song, Kai Liu, Zhongzhi Luan, Peng Wang, Lei Sun, Shengwei Jiang, Hongjun Xiang, Yanbin Chen, Jun Du, Haifeng Ding, Ke Xia, Jiang Xiao, and Di Wu. Observation of spin-orbit magnetoresistance in metallic thin films on magnetic insulators. *Science Advances*, 4(1):eaao3318, jan 2018.

[81] Hua Wang, Dazhi Hou, Zhiyong Qiu, Takashi Kikkawa, Eiji Saitoh, and Xiaofeng Jin. Antiferromagnetic anisotropy determination by spin Hall magnetoresistance. *Journal of Applied Physics*, 122(8):083907, aug 2017.

[82] Geert R. Hoogeboom, Aisha Aqeel, Timo Kuschel, Thomas T. M. Palstra, and Bart J. van Wees. Negative spin Hall magnetoresistance of Pt on the bulk easy-plane antiferromagnet NiO. *Applied Physics Letters*, 111(5):052409, jul 2017.

[83] Yang Ji, J. Miao, Y. M. Zhu, K. K. Meng, X. G. Xu, J. K. Chen, Y. Wu, and Y. Jiang. Negative spin Hall magnetoresistance in antiferromagnetic Cr 2 O 3 /Ta bilayer at low temperature region. *Applied Physics Letters*, 112(23):232404, jun 2018.

[84] Richard Schlitz, Tobias Kosub, Andy Thomas, Savio Fabretti, Kornelius Nielsch, Denys Makarov, and Sebastian T.B. Goennenwein. Evolution of the spin hall magnetoresistance in Cr2O3/Pt bilayers close to the Néel temperature. *Applied Physics Letters*, 112:132401, 2018.

[85] Johanna Fischer, Olena Gomonay, Richard Schlitz, Kathrin Ganzhorn, Nynke Vlietstra, Matthias Althammer, Hans Huebl, Matthias Opel, Rudolf Gross, Sebastian T. B. Goennenwein, and Stephan Geprägs. Spin Hall magnetoresistance in antiferromagnet/heavy-metal heterostructures. *Physical Review B*, 97(1):014417, jan 2018.

[86] L. Baldrati, A. Ross, T. Niizeki, C. Schneider, R. Ramos, J. Cramer, O. Gomonay, M. Filianina, T. Savchenko, D. Heinze, A. Kleibert, E. Saitoh, J. Sinova, and M. Kläui. Full angular dependence of the spin Hall and ordinary magnetoresistance in epitaxial antiferromagnetic NiO(001)/Pt thin films. *Physical Review B*, 98(2):024422, jul 2018.

[87] S. DuttaGupta, R. Itoh, S. Fukami, and H. Ohno. Angle dependent magnetoresistance in heterostructures with antiferromagnetic and non-magnetic metals. *Applied Physics Letters*, 113(20):202404, nov 2018.

[88] R Bertacco, M Cantoni, M. Riva, A. Tagliaferri, and F. Ciccacci. Epitaxial Growth and Characterization of Layered Magnetic Nanostructures. *Applied Surface Science*, 252(5):1754–1764, dec 2005.

[89] M Spak, D Mammato, S Jain, and D Durham. Mechanism and lithographic evaluation of image reversal in AZ 5214 photoresist. In *Seventh International Technical Conference on Photopolymers, Ellenville, New York*, volume 120, 1985.

[90] L.J. van der Pauw. A method of measuring the resistivity and hall coefficient on lamellae of arbitrary sghape. *Philips Technical Review*, 1958.

[91] P. Daniil and E. Cohen. Low field Hall effect magnetometry. *Journal of Applied Physics*, 53(11):8257–8259, 1982.

[92] H. Reichlová, D. Kriegner, V. Holý, K. Olejník, V. Novák, M. Yamada, K. Miura, S. Ogawa, H. Takahashi, T. Jungwirth, and J. Wunderlich. Current-induced torques in structures with ultrathin IrMn antiferromagnets. *Physical Review B*, 92(16):165424, oct 2015.

[93] A Daire, W Goeke, and M A Tupta. White Paper: New instruments can lock out lock-ins. *Keithley Instruments, Inc*, 2005.

[94] C. Andersson, B. Sanyal, O. Eriksson, L. Nordström, O. Karis, D. Arvanitis, T. Konishi, E. Holub-Krappe, and J. Hunter Dunn. Influence of Ligand States on the Relationship between Orbital Moment and Magnetocrystalline Anisotropy. *Physical Review Letters*, 99(17):177207, oct 2007.

[95] S. S P Parkin. Systematic variation of the strength and oscillation period of indirect magnetic exchange coupling through the 3 d , 4 d , and 5 d transition metals. *Physical Review Letters*, 67(25):3598–3601, dec 1991.

[96] Carmine Autieri and Biplab Sanyal. A systematic study of 4d and 5d transition metal mediated exchange coupling between Fe and Gd nanolaminates. *Journal of Physics Condensed Matter*, 2017.

Bibliography

[97] S. Karoui, H. Amara, B. Legrand, and F. Ducastelle. Magnetism: the driving force of order in CoPt, a first-principles study. *Journal of Physics: Condensed Matter*, 25(5):056005, feb 2013.

[98] M. Di Loreto. *Magneto-Resistive phenomena in antiferromagnetic-based spintronic memories*. PhD thesis, Politecnico di Milano, 2015.

[99] Miren Isasa, Estitxu Villamor, Luis E. Hueso, Martin Gradhand, and Fèlix Casanova. Temperature dependence of spin diffusion length and spin Hall angle in Au and Pt. *Physical Review B - Condensed Matter and Materials Physics*, 91(2):1–7, 2015.

[100] Dong Ok Kim, Kyung Mee Song, Yongseong Choi, Byoung Chul Min, Jae Sung Kim, Jun Woo Choi, and Dong Ryeol Lee. Asymmetric magnetic proximity effect in a Pd/Co/Pd trilayer system. *Scientific Reports*, 2016.

[101] T. Khajil and J. Khalifeh. Spin polarization of vanadium overlayers on a semi-infinite tantalum substrate. *Surface Science*, 389:310–316, 1997.

[102] X.S. Du, S. Hak, T. Hibma, O.C. Rogojanu, and B. Struth. X-rays diffraction on a new chromium oxide single-crystal thin film prepared by molecular beam epitaxy. *Journal of Crystal Growth*, 293(1):228–232, jul 2006.

[103] Qiang Fu and Thomas Wagner. Thermal stability of Cr clusters on SrTiO3(1 0 0). *Surface Science*, 505:39–48, 2002.

[104] Qiang Fu and Thomas Wagner. On the tunability of chemical reactions at metal-oxide interfaces. *Surface Science*, 574(2-3), 2005.

[105] C.D. Wagner, W.N. Riggs, L.E. Davies, J.F. Moulder, and G.E. Muilenberg (Eds.). *Handbook of X-ray Photoelectron Spectroscopy*. 1979.

[106] C. Theil, J. van Elp, and F. Folkmann. Ligand field parameters obtained from and chemical shifts observed at the Cr L2,3 edges. *Physical Review B*, 1999.

[107] Yu S. Dedkov, A. S. Vinogradov, M. Fonin, C. König, D. V. Vyalikh, A. B. Preobrajenski, S. A. Krasnikov, E. Yu Kleimenov, M. A. Nesterov, U. Rüdiger, S. L. Molodtsov, and G. Güntherodt. Correlations in the electronic structure of half-metallic ferromagnetic CrO2 films: An x-ray absorption and resonant photoemission spectroscopy study. *Physical Review B - Condensed Matter and Materials Physics*, 2005.

[108] S. O. Kucheyev, B. Sadigh, T. F. Baumann, Y. M. Wang, T. E. Felter, T. Van Buuren, A. E. Gash, J. H. Satcher, and A. V. Hamza. Electronic structure of chromia aerogels from soft x-ray absorption spectroscopy. *Journal of Applied Physics*, 2007.

[109] O. C. Rogojanu. *Stabilizing CrO by epitaxial growth*. PhD thesis, University of Groningen, 2002.

[110] John Goodenough. Goodenough-Kanamori rule. *Scholarpedia*, 3(10):7382, 2008.

[111] Gerd Bergmann. Weak localization in thin films. a time-of-flight experiment with conduction electrons, 1984.

[112] J. Kondo. Resistance Minimum in Dilute Magnetic Alloys. *Progress of Theoretical Physics*, 32(1):37–49, jul 1964.

[113] Sibylle Meyer, Richard Schlitz, Stephan Geprägs, Matthias Opel, Hans Huebl, Rudolf Gross, and Sebastian T.B. Goennenwein. Anomalous Hall effect in YIG|Pt bilayers. *Applied Physics Letters*, 106(13), 2015.

[114] G. Y. Guo, Q. Niu, and N. Nagaosa. Anomalous Nernst and Hall effects in magnetized platinum and palladium. *Physical Review B - Condensed Matter and Materials Physics*, 89(21):1–6, 2014.

[115] Miren Isasa, Saül Vélez, Edurne Sagasta, Amilcar Bedoya-Pinto, Nico Dix, Florencio Sánchez, Luis E. Hueso, Josep Fontcuberta, and Fèlix Casanova. Spin Hall Magnetoresistance as a Probe for Surface Magnetization in Pt/CoFe2 O4 Bilayers. *Physical Review Applied*, 6(3):1–10, 2016.

[116] R. Muralidharan, T. H. Jang, C. H. Yang, Y. H. Jeong, and T. Y. Koo. Magnetic control of spin reorientation and magnetodielectric effect below the spin compensation temperature in TmFeO3. *Applied Physics Letters*, 90(1):3–6, 2007.

[117] J.A. Leake, G Shirane, and J.P. Remeika. The magnetic structure of thulium orthoferrite, TmFeO3. *Solid State Communications*, 6(1):15–17, jan 1968.

[118] F. C. Rossol. Temperature dependence of magnetic domain structure and wall energy in single-crystal thulium orthoferrite. *Journal of Applied Physics*, 39(11):5263–5267, 1968.

[119] E. M. Gyorgy, J. P. Remeika, and F. B. Hagedorn. Magnetic behavior of some orthoferrites in the anisotropy change region. *Journal of Applied Physics*, 39(2):1369–1370, 1968.

[120] Kailin Zhang, Kai Xu, Xiumei Liu, Zeyu Zhang, Zuanming Jin, Xian Lin, Bo Li, Shixun Cao, and Guohong Ma. Resolving the spin reorientation and crystal-field transitions in TmFeO3with terahertz transient. *Scientific Reports*, 6(March):1–7, 2016.

[121] U. Staub, L. Rettig, E. M. Bothschafter, Y. W. Windsor, M. Ramakrishnan, S. R.V. Avula, J. Dreiser, C. Piamonteze, V. Scagnoli, S. Mukherjee, C. Niedermayer, M. Medarde, and E. Pomjakushina. Interplay of Fe and Tm moments through the spin-reorientation transition in TmFeO3. *Physical Review B*, 96(17):1–11, 2017.

[122] A V Kimel, A Kirilyuk, A Tsvetkov, R V Pisarev, and Th. Rasing. Laser-induced ultrafast spin reorientation in the antiferromagnet TmFeO3. *Nature*, 429(6994):850–853, jun 2004.

[123] Suk Jin Ahn, Jung Hoon Lee, Hyun Myung Jang, and Young Kyu Jeong. Multiferroism in hexagonally stabilized TmFeO3thin films below 120 K. *Journal of Materials Chemistry C*, 2(23):4521–4525, 2014.

[124] S. Y. Huang, X. Fan, D. Qu, Y. P. Chen, W. G. Wang, J. Wu, T. Y. Chen, J. Q. Xiao, and C. L. Chien. Transport magnetic proximity effects in platinum. *Physical Review Letters*, 109(10):1–5, 2012.

[125] H. Julian Goldsmid. The Thermoelectric and Related Effects. In *Springer Series in Materials Science*, pages 1–7. 2016.

[126] F. L. A. Machado, P. R. T. Ribeiro, J. Holanda, R. L. Rodríguez-Suárez, A. Azevedo, and S. M. Rezende. Spin-flop transition in the easy-plane antiferromagnet nickel oxide. *Physical Review B*, 95(10):104418, mar 2017.

[127] Xiao Liang, Yupeng Zhu, Bo Peng, Longjiang Deng, Jianliang Xie, Haipeng Lu, Mingzhong Wu, and Lei Bi. Influence of Interface Structure on Magnetic Proximity Effect in Pt/Y3Fe5O12 Heterostructures. *ACS Applied Materials & Interfaces*, 8(12):8175–8183, 2016.

[128] Dirk J Groenendijk, Carmine Autieri, T. C. van Thiel, Wojciech Brzezicki, N. Gauquelin, P. Barone, K. H. W. van den Bos, S. van Aert, J. Verbeeck, Alessio Filippetti, Silvia Picozzi, Mario Cuoco, and Andrea D Caviglia. Berry phase engineering at oxide interfaces. *preprint on ArXiv*, (October), oct 2018.